MODELING THE COSEISMIC AND POSTSEISMIC DEFORMATION OF THE 2002 MW7.9 DENALI, AK EARTHQUAKE

By

Hugh Harper, B.S.

A Thesis Submitted in Partial Fulfillment of the Requirements

for the Degree of

Master of Science

in

Geophysics

University of Alaska Fairbanks

August 2017

Jeffrey T. Freymueller, Committee Chair
Douglas Christensen, Committee Member
Stephen Holtkamp, Committee Member
Carl Tape, Committee Member
Paul McCarthy, Chair
Department of Geosciences
Paul Layer, Dean
College of Natural Science and Mathematics
Michael Castellini, *Dean of the Graduate School*

Abstract

The 2002 Mw7.9 Denali fault earthquake was among the largest intraplate earthquakes on record, and the ongoing crustal deformation of the event is still observed today. Understanding the deformation patterns in the years following the earthquake can give insight into the viscoelastic properties of the crust and upper mantle. Additionally, an accurate and predictive model of this deformation is essential to developing and increasingly complete tectonic model of Alaska.

Using primarily GPS measurements, deformation can be measured to millimeter-level precision. To develop a coseismic and postseismic model of the earthquake, 224 GPS coseismic displacement measurements (along with SAR and geologic measurements from past studies) are inverted for fault slip distribution. Coseismic slip and consequent stress changes drive the forward postseismic deformation model, which is constrained by 119 postseismic GPS time series. Both models use a 1D elastic structure.

The preferred 1D coseismic model fits the coseismic data with a weighted residual sum of squares (WRSS) of 4.86e3 m^2, with more deep slip than a homogeneous model and a geodetic moment of 8.92e20 N m (Mw 7.97). The Maxwell viscoelastic parameters used for the first postseismic model run are 3e19 Pa s for the lower crust; 5e18 Pa s for the viscoelastic shear zone; and 10e19 and 10e20 south and north of the fault, respectively, for the asthenosphere. The respective Kelvin parameters are all an order of magnitude less.

The deep coseismic slip (a product of the 1D elastic model) eliminates the need to add deep slip, which was done in past studies. Based on time series analysis, the decade-plus of data will certainly improve the model prediction relative to previous models, but future observations will be needed to verify this. No preferred postseismic model is developed, and more postseismic models will be run to better fit the observations.

Table of Contents

List of Figures

Page

List of Tables

Page

Acknowledgements

I would like to extend a great thanks to my advisor, Jeff Freymueller, who has afforded me so many opportunities here at the University of Alaska Fairbanks with the funding for chances to do fieldwork, to travel abroad—but who has also instilled in me the confidence to continue in academia. My time as a student at the Geophysical Institute has been very valuable to me.

I'd like to thank my committee for valuable insight not just in scientific matters but in communicating my work as well. While I may have thought of writing and public speaking as some of the more daunting aspects of science, I am very happy to approach both of these things with great enthusiasm and to always improve.

I'd like to thank my collaborator, Yan Hu, at the University of Science and Technology of China in Hefei. Yan's finite element modeling expertise has been, and will continue to be, essential to this project.

Lastly, I want to thank my family who, while far away and scattered across the Lower 48, has offered their support over frequent phone calls. In addition, my utmost thanks go to the University of Alaska Fairbanks Student Health and Counseling Center—they know none of this is easy, and they have been so helpful, caring, and responsive in my short time here.

Chapter 1 Introduction

On November 3, 2002, an Mw7.9 strike-slip earthquake shook interior Alaska, rupturing across three faults with a 340-kilometer long surface rupture. The earthquake was among the largest strike-slip events on record, and a combination of quick field deployment and ongoing observation efforts in the following decade makes it a very convenient event to study. Early efforts to model the postseismic deformation following the earthquake were able to adequately fit the data at the time, and showed that postseismic deformation required multiple mechanisms. However, as later observations did not agree with those model predictions, it is necessary to revisit the problem and develop a more complete model for the coseismic and postseismic phases of the earthquake cycle in the tectonic setting of interior Alaska.

1.1 Tectonics of Interior Alaska

The Denali fault is part of a series of right-lateral strike-slip faults including the Fairweather and Tintina faults that accommodate strain from the oblique accretion of the Yakutat block onto the North American plate in southern Alaska. The rupture history of the Denali fault is not well known, but the previous event, though undated, was measured to have 6 to 8 meters of offset, and in the 1970's the Quaternary slip rate was believed to be between 8 and 13 mm/year [*Plafker et al.*, 1977]. More recent studies divide the Denali fault into a western, central, and eastern third, with long-term slip rates of 9.4 ± 1.6, 12.1 ± 1.7, and 8.4 ± 2.2 mm/yr, respectively, with a slip rate of 6.0 ± 1.2 mm/yr along the Totschunda fault [*Matmon et al.*, 2006]. Observations of Holocene fault activity on the Eastern Denali fault suggest a much lower current slip rate as low as 1.7-2.5 mm/yr with a maximum of 8 mm/yr [*Bender and Haeussler*, 2017; *Seitz et al.*, 2008]. The lower slip rate along the Denali fault east of the Totschunda junction suggests the Totschunda fault becomes the active strand and possibly connects to the Fairweather fault [*Fletcher*, 2002].

1.2 The Denali Fault Earthquake

The Mw7.9 event was preceded by the Mw6.7 Nenana Mountain earthquake on October 28, due west of the Denali earthquake epicenter. The resulting changes in Coulomb stress state could have been responsible for the triggering and propagation of the Denali

earthquake [*Eberthart-Phillips et al.*, 2003]. The Mw7.9 earthquake nucleated on the Susitna Glacier fault, a previously unrecognized thrust fault, and then migrated onto the Denali fault for the main extent of the rupture (Figure 1). The Denali fault rupture terminated and migrated onto the Totschunda fault (thought to be due to its preferential orientation with respect to regional stress), with about 14 km of discontinuity in the rupture's surface expression [*Eberthart-Phillips et al.*, 2003]. Seismograms indicated heterogeneous slip along the rupture, and strong motion sensors identified three main sub-events.

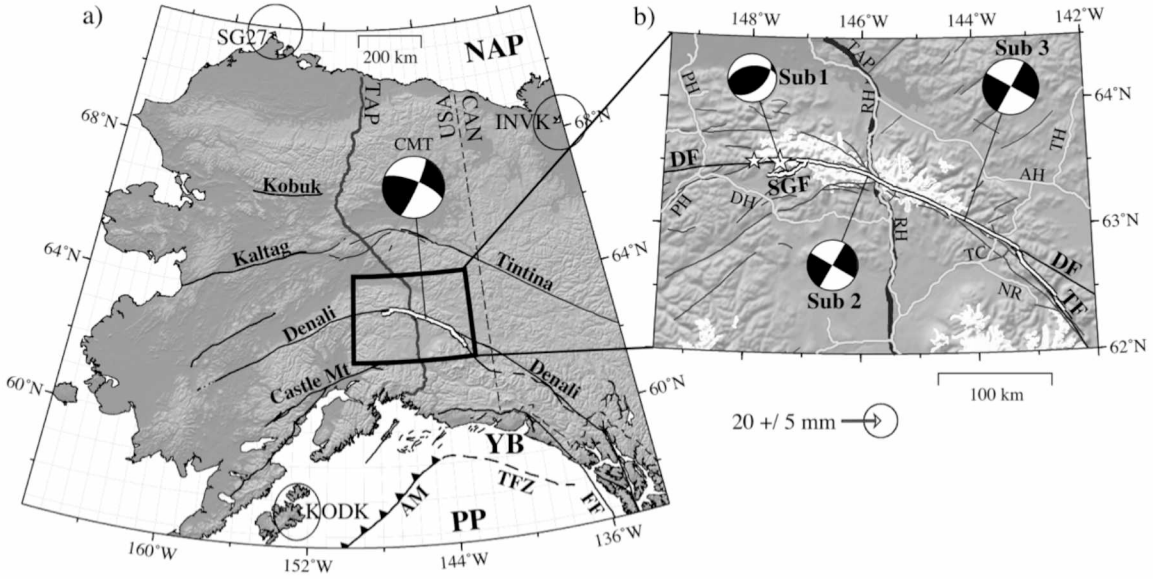

Figure 1. From *Hreinsdóttir et al.* [2006]. The Denali fault and the ruptured segments and the tectonic setting of southern Alaska. There are several regional right-lateral strike-slip faults in addition to the Denali fault. Shown in b) are the focal mechanisms for the three subevents of the rupture.

1.3 The Earthquake Cycle

Reid [1910] first proposed the elastic rebound theory of earthquakes to explain the 1906 San Francisco earthquake. He suggested that stress and strain gradually increase in the crust and are then released during an earthquake. This theory became the basis for the earthquake/crustal deformation cycle model. The earthquake cycle model consists of three major phases: interseismic, intraplate deformation between earthquakes wherein stress and strain accumulate along faults; coseismic, the quick release of the accumulated strain via brittle failure; and postseismic, the deformation triggered by and following an earthquake. Postseismic deformation is superimposed on interseismic deformation, and is the dominant deformation

signal shortly after an earthquake but decays with time. Sometimes a "pre-seismic" phase will be included in earthquake cycle discussions, but there have been no independent observations to confirm such a phase distinct from the interseismic period.

1.3.1 Coseismic Deformation

As adjacent plates (or micro-plates) move, their differential motion is accommodated on a material discontinuity known as a fault. If these faults were essentially frictionless, then displacement along the fault would be steady and no stress or strain would accumulate outside of the fault zone. Impedance of this motion (for example, by friction keeping the shallow part of the fault "locked" in place) will cause a cyclic accumulation and release of stress and strain along the boundary.

The lithosphere, the mostly rigid upper layer of the Earth comprising plates and micro-plates, can be split into two layers based on how the rocks therein deform: the upper layer, the schizosphere, where rocks deform following a velocity-weakening friction law; and the lower plastosphere, where deformation follows a velocity-strengthening friction law [*Scholz*, 2002]. In the schizosphere, faults are effectively "locked" during the interseismic period, impeding plate motion near the fault and causing interseismic surface deformation. One of the earliest quantitative models of interseismic deformation is described in *Savage and Burford* [1973] (Figure 2), which shows that deformation for a 2D strike-slip fault increases away from the fault as an arctangent function depending on the locking depth (i.e., the width of the schizosphere) and the steady slip rate. When stress reaches some critical point, the fault will rupture and the strained lithosphere will recover the elastic deformation accumulated during the interseismic period. Of course, the fault rheology and frictional properties are almost certainly not homogeneous, so some regions of the fault will slip less than others or remain locked altogether to rupture at a later time.

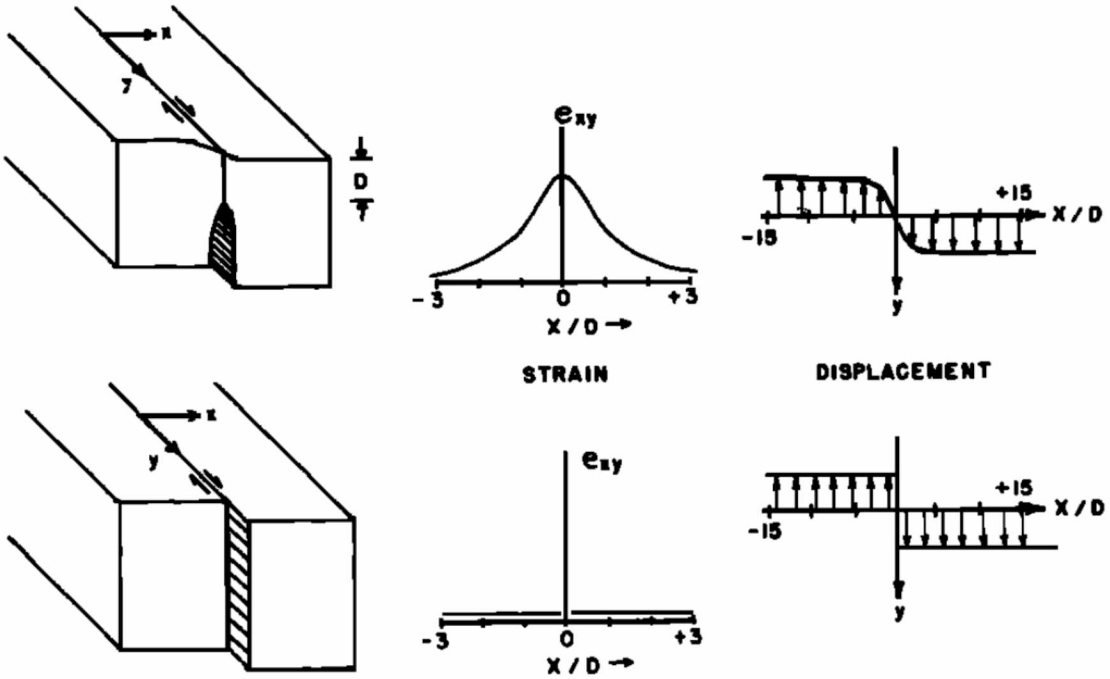

Figure 2. Simple block dislocation model of the earthquake cycle from *Savage and Burford* [1973]. Strain accumulates near the fault as it slips continuously beneath the locking depth, D. During the coseismic phase, that strain is recovered.

As the fault extends into the plastosphere, displacement along the interface will occur essentially unimpeded with the two lithospheric plates, a process known as ductile fault creep. It's important to note that creep can occur in the upper crust, too, such as in brittle creep fault zones [*Perfettini and Avouac*, 2004], and deformation is just a matter of local rheology and stress when deviating from the idealistic model.

Below the lithosphere is the asthenospheric mantle, and the connection with faults (i.e., a fault's physical manifestation) becomes unclear. Generally, in the theory of plate tectonics, the asthenosphere acts as the body over which the lithospheric plates move, and the flow of the asthenosphere, in part, drives the motion of the plates [*Savage and Prescott*, 1978].

1.3.2 Postseismic Deformation

When the lithosphere seismically ruptures, there is a redistribution of the stresses that accumulated along the fault during the interseismic period [*Chinnery*, 1961; *Stein*, 1999]. On nearby faults, this will change the overall stress state, increasing or decreasing the likelihood of rupture. On the fault interface itself, stresses will become concentrated in regions of low

coseismic slip and around the edges of the slip patch. This is the driving force behind one of the two primary postseismic deformation mechanisms: afterslip.

Afterslip occurs aseismically along the fault interface. Since the coseismic slip distribution is not uniform, there must be some difference in frictional properties along the fault or in the present stress state arresting dynamic rupture in certain places. *Marone et al.* [1991] suggests a change in rate-and-state frictional properties to velocity-strengthening is the cause of coseismic slip decrease with depth. The stress increase in these regions is then relaxed as afterslip. The surface deformation due to afterslip follows a logarithmic decay curve, and the deformation rate is typically less than the interseismic rate within two years of the event [*Marone et al.*, 1991]. The rate of afterslip and aftershock seismicity may be related in the same way strain rate and seismicity rate are related in the interseismic period, as the seismicity rate around the creeping zone is thought to be proportional to the stress rate (which depends on slip rate) [*Perfettini and Avouac*, 2004].

While the upper crust exhibits almost exclusively elastic deformation, the lower crust is weaker and exhibits a viscoelastic rheology. The mechanical structure and strength of the lithospheric mantle remain up for debate—some suggest a strong elastic upper mantle (the "jelly sandwich model") while others believe the elastic strength of the lithosphere resides solely in the upper crust and the upper mantle is viscoelastic (the "crème brulee" model) [*Bürgmann and Dresen*, 2008]. Early evidence for a viscoelastic rheology came from isostatic adjustment observations, where the surface rebounds in response to the removal of a great load (the Laurentide ice sheet, in this case) [*Nur and Mavko*, 1974]. Viscoelastic behavior in the mantle was identified earlier due to its damping of seismic waves [*Orowan*, 1967].

For sufficiently large earthquakes (typically those on plate boundaries), the coseismic elastic deformation strains the entire lithosphere. The viscoelastic rheologies of the lower crust and upper mantle cannot sustain the imparted strain and will relax in response, contributing to postseismic deformation at the surface. Depending on the size of the earthquake, this process can last from as little as a few years to many decades (such is the case for megathrust earthquakes).

On a much smaller scale, poroelastic rebound contributes to postseismic deformation. This is due to the rapid change in hydraulic gradient in response to coseismic stress changes and the subsequent movement of groundwater. It is a very localized process and occurs only in the weeks following the earthquake [*Nur and Booker*, 1972].

Chapter 2 GPS Data Collection and Processing

2.1 Distribution of Sites and Survey Frequency

Shortly after the earthquake, a campaign GPS field response began, with priority placed on campaign sites with known pre-earthquake velocities, and 10 new continuous sites were installed. Preliminary postseismic deformation models that identified the most important areas in constraining model parameters determined the spatial distribution of GPS surveying [*Freed et al.*, 2006] along with previous postseismic studies of other earthquakes (e.g., *Hearn et al.* [2002]). Preferred GPS network design is dependent on the postseismic mechanisms and parameters in the chosen forward model, but the area beyond the fault tip and a cross-section through the center of the fault were consistently found to be important areas for data collection [*Freed et al.*, 2006].

The following summer, more campaign sites, in addition to those surveyed immediately post-earthquake, were surveyed. For 4-5 years after the earthquake, most campaign sites deemed important to postseismic study were surveyed at least annually on 1-4 day deployments. In later years, measurements were made once every 1-3 years for most sites.

2.2 GIPSY/OASIS Processing

The GPS data were analyzed using the GIPSY/OASIS II software (version 5.0) developed at JPL, and the analysis routine is described in *Fu and Freymueller* [2012]. Coordinates were estimated in single-site point positioning (PPP) mode. JPL's reanalysis orbit and clock products were used along with a consistent set of models over the entire observation period. A priori dry tropospheric delay estimates were obtained from the Global Pressure and Temperature (GPT) model [*Boehm et al.*, 2006]. Effects of ocean tidal loading were removed using the TPXO7.0 model, with Greens functions modeled in the center of mass of the whole earth system (CM) reference frame, consistent with the JPL orbit and clock products. The estimated PPP GPS solutions are combined to form the Alaska network of solutions (Figure 3). A set of reference sites is used to define a seven parameter Helmert transformation to align each daily GPS solution to the International Terrestrial Reference Frame (ITRF) 2008, and daily solutions are

weighted by the inverse of the corresponding covariance matrix. The time series of daily solutions for each site are then extracted and used for modeling the site's motion with time.

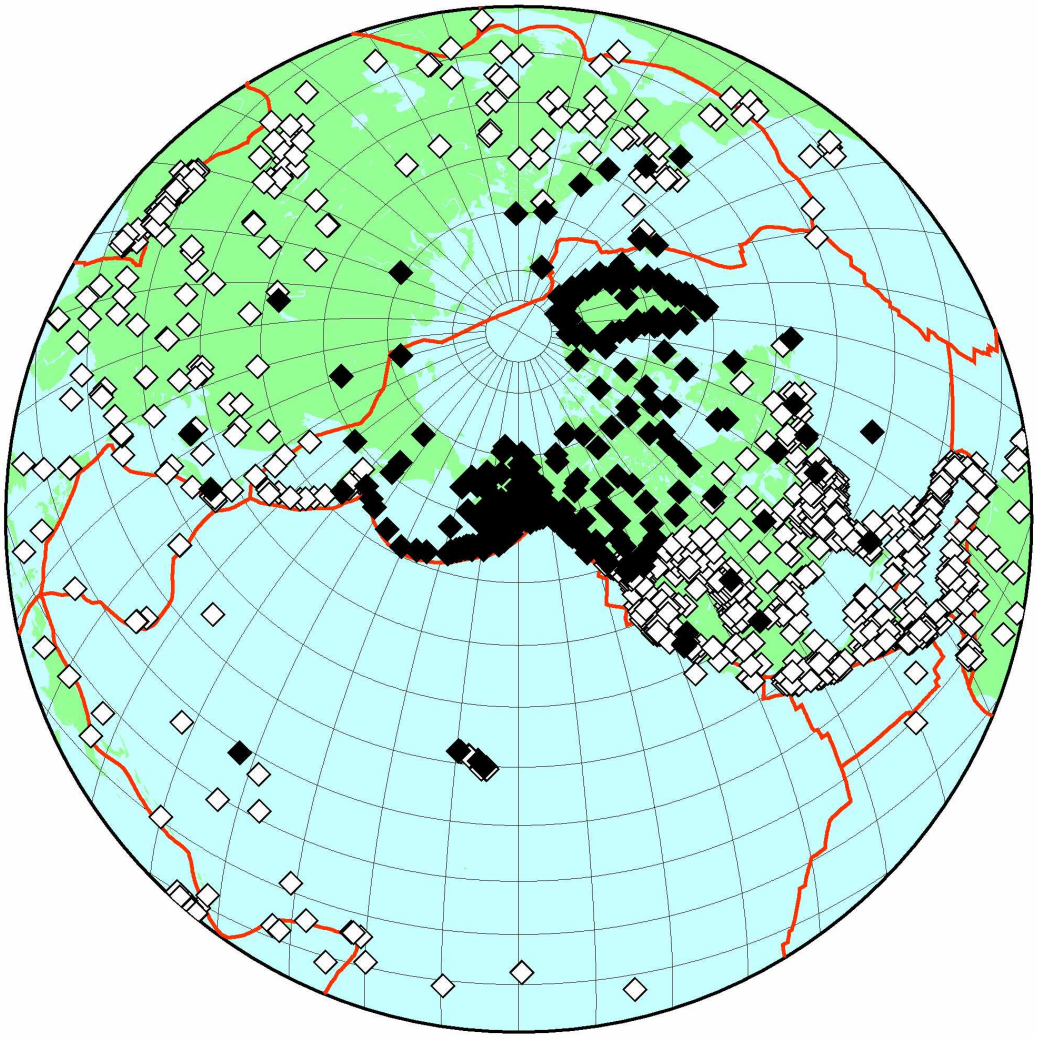

Figure 3. Spatial extent of the Alaska subnet, used in aligning the GPS daily solutions. Black diamonds are included in the Alaska solutions while white diamonds are not.

Chapter 3 Estimating Coseismic Displacements

In estimating coseismic displacements, GPS sites are classified as one of three types of sites: continuous sites; campaign sites with good pre-earthquake coverage; and campaign sites with poor pre-earthquake coverage. The criterion for distinguishing good coverage from poor coverage in this study is the ability to estimate a secular velocity from the pre-earthquake time series.

3.1 Continuous GPS

For continuous GPS sites (which comprise 20 of the sites used in the coseismic study), a simple window of +/- 4 days is applied to the time series (Figure 4). Daily positions are averaged (with weighting based on their uncertainty) before and after the earthquake. The difference in these averaged positions gives the coseismic displacement.

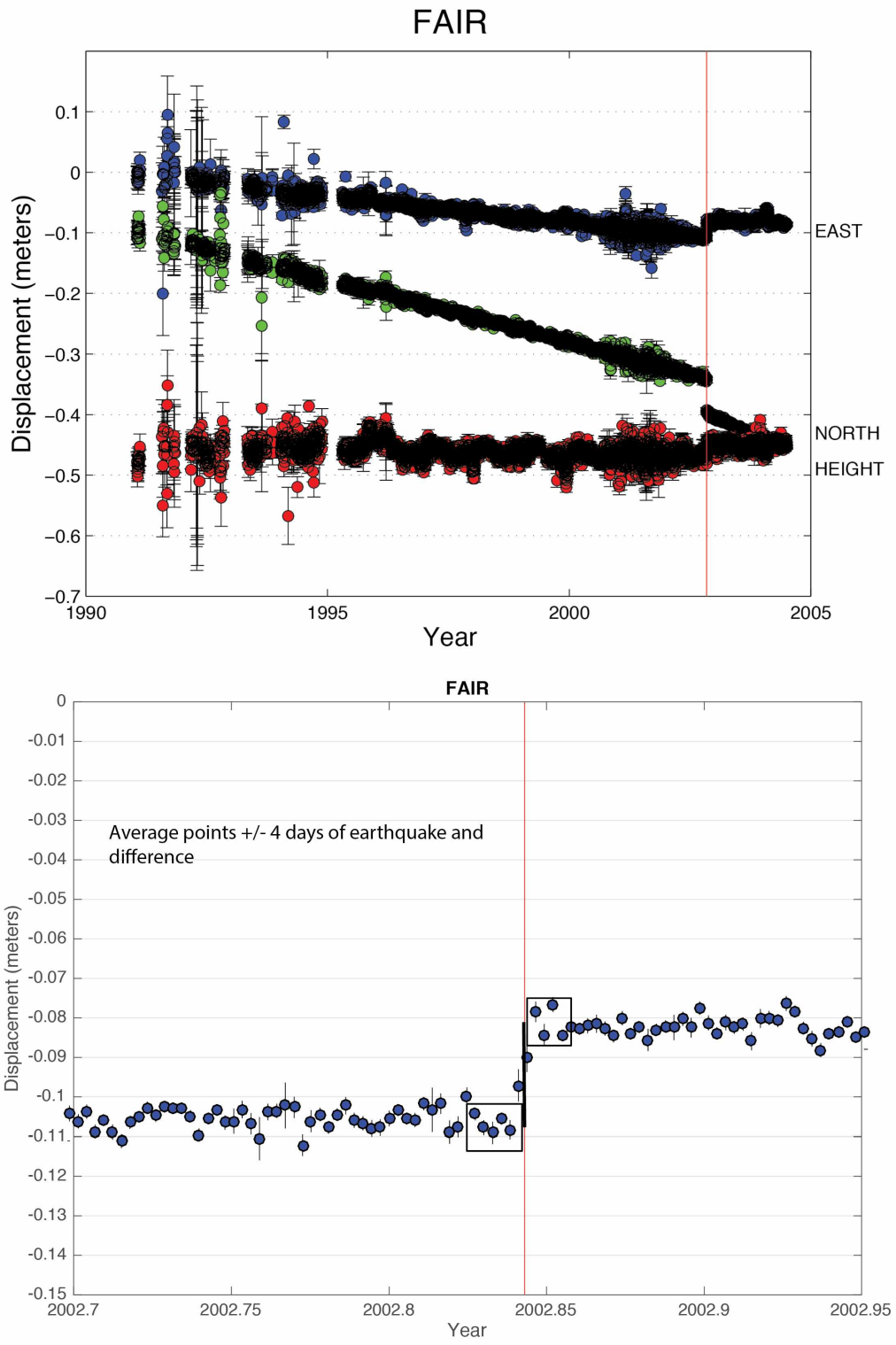

Figure 4. Estimating coseismic displacement from a GPS time series. For continuous sites, the position data are windowed four days before and after the earthquake, averaged, and differenced. The day of the earthquake is excluded.

3.2 Campaign GPS

For campaign sites with good pre-earthquake coverage, the pre-earthquake time series is fit with a simple linear velocity model (Figure 5). The position immediately before the earthquake is then projected from the model. The first post-earthquake data point is selected and then projected back to the time of the earthquake using the pre-earthquake velocity, giving a first approximation for coseismic displacement. However, the post-earthquake time series is affected by postseismic displacement mechanisms and is not linear. Since many campaign sites were not surveyed immediately after the earthquake, a correction must be applied to the displacement estimate (discussed below) for those sites. For sites surveyed within the first 3 weeks after the earthquake, it is assumed that no postseismic correction is needed.

5A

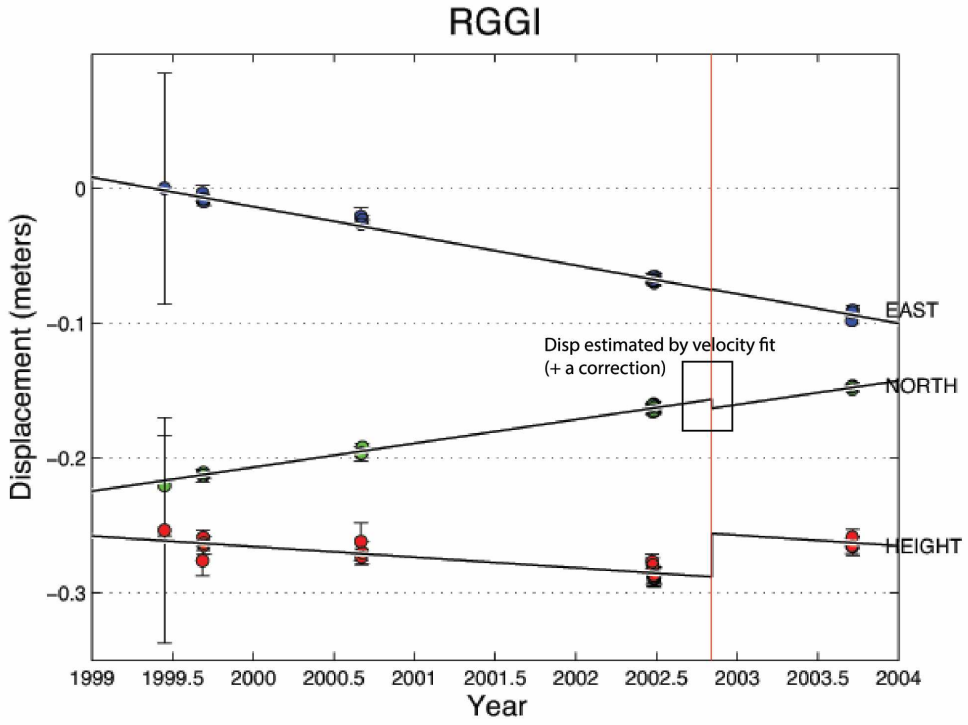

Figure 5. Estimating coseismic displacements from campaign GPS time series. (A) Campaign GPS with good coverage allows an estimate of secular velocity which is projected to the time of the earthquake. The same linear trend is back-projected from the first post-earthquake data and, if needed, a postseismic correction is applied. (B) Poor campaign GPS coverage requires a differencing of the last pre-earthquake epoch and first post-earthquake epoch, an interseismic correction, and depending on the response time at that site, a postseismic correction. The corrections used are described in *Hreinsdóttir et al.* [2006] supplementary materials.

5B

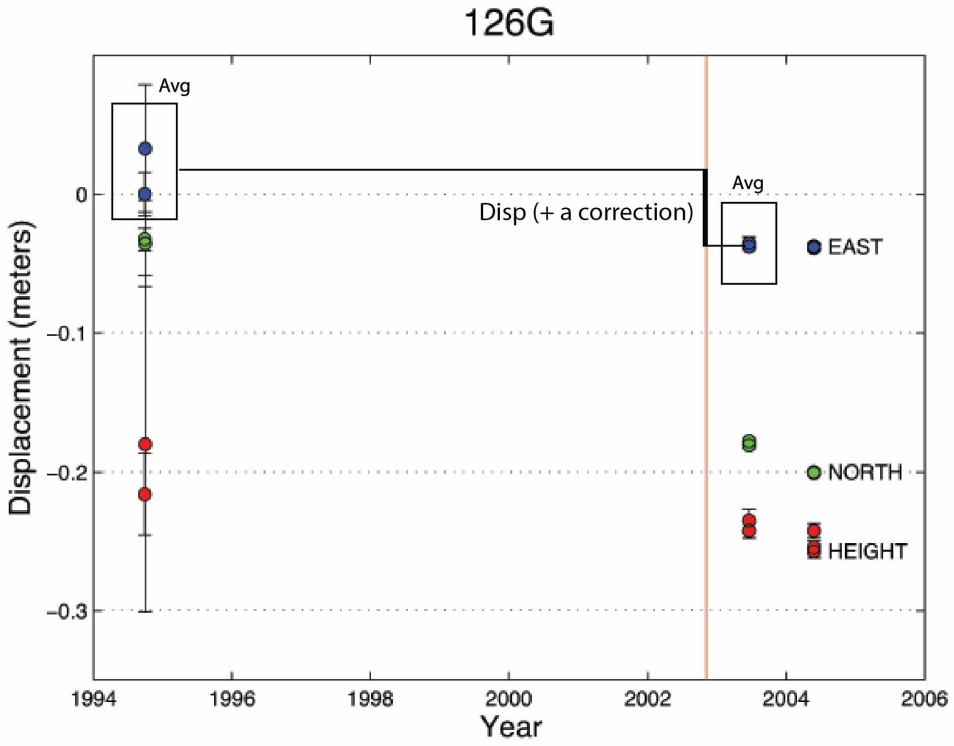

Figure 5 cont.

For campaign sites with poor pre-earthquake coverage, a weighted average position is calculated for the last pre-earthquake epoch and the first post-earthquake epoch, and these two positions are differenced. In all cases, an interseismic correction must be applied to the displacement estimate based on information from nearby sites or from a block model. Depending on the time of the first post-earthquake survey, a postseismic correction may need to be applied.

Interseismic corrections can be calculated with geodetic block models. For a block with a given pole of rotation and angular velocity, the linear velocity can be calculated at any point on the block. Block models also account for the elastic deformation from the faults separating the blocks. Alternatively, velocities can be determined by 2D interpolation using GPS sites with good pre-earthquake time series (this includes continuous GPS sites). For this study, interseismic corrections are taken from the supplementary materials of *Hreinsdóttir et al.* [2006], which uses a block model of southern Alaska to estimate interseismic velocity. The interseismic corrections are given in a North American plate (NOAM) fixed reference frame, so

the time series must be transformed to this reference frame to apply them. This requires a rotation and an origin adjustment, given by the GEODVEL model from *Argus et al.* [2010].

Postseismic corrections can also be estimated by more than one method. For sites surveyed immediately post-earthquake and again the following spring (when the remaining campaign sites were surveyed), a displacement can be calculated over this interval. In the same way interseismic velocities are interpolated, postseismic displacements over this interval are interpolated (again, continuous GPS sites can be used). Alternatively, the displacements over this short interval can be inverted for a rough kinematic afterslip model, and postseismic corrections can be predicted from the rough afterslip model. The specific corrections for this study are taken from the supplementary materials of *Hreinsdóttir et al.* [2006].

3.3 Other Sources of Data

In addition to GPS-derived displacements, data from two other previous studies are used in the coseismic model. SAR offset data from *Elliott et al.* [2007] give displacement measurements along a swath including the Richardson Highway which overlaps 43 of the GPS sites used in this study. The data were acquired by the Canadian RADARSAT-1 satellite on 24 October 2002 and 4 January 2003. Rather than using interferometry in estimating coseismic displacement, cross-correlation of the SAR amplitude images are used.

Geologic offset measurements collected along the Denali and Totschunda faults by *Haeussler et al.* [2004] and along the Susitna Glacier fault by *Crone et al.* [2004] are also used to constrain the slip inversion at the surface. The data used are single point slip estimates, but the studies use different methods of estimating the continuous slip distribution along the fault rupture, and the moment magnitude estimated from these slip distributions are in good agreement with both seismic and geodetic estimates. These studies recommend using the upper envelope of geological surface offsets because it is more likely that a given measurement underestimates the true slip rather than overestimates it. The work of *Hreinsdóttir et al.* [2006] supports this approach, and I used the same sampling of surface data as *Elliott et al.* [2007].

Chapter 4 3-D Fault Model and Coseismic Inversion

The GPS, SAR, and geologic displacement data are jointly inverted for coseismic slip on the rupture interface, spanning three faults. The Denali and Totschunda faults are modeled as a series of vertical planes, extending to 24 km depth (Figure 6). The Susitna Glacier fault is approximated by two planes: a shallow plane dipping at 19 degrees, as it is measured at the surface [*Crone et al.*, 2004], connecting at depth to a 48 degree dipping plane, consistent with the earthquake focal mechanism. All fault elements are 2 km by 2 km, and there are 1263 elements in total. The fault geometry was re-meshed from the model of *Elliott et al.* [2007].

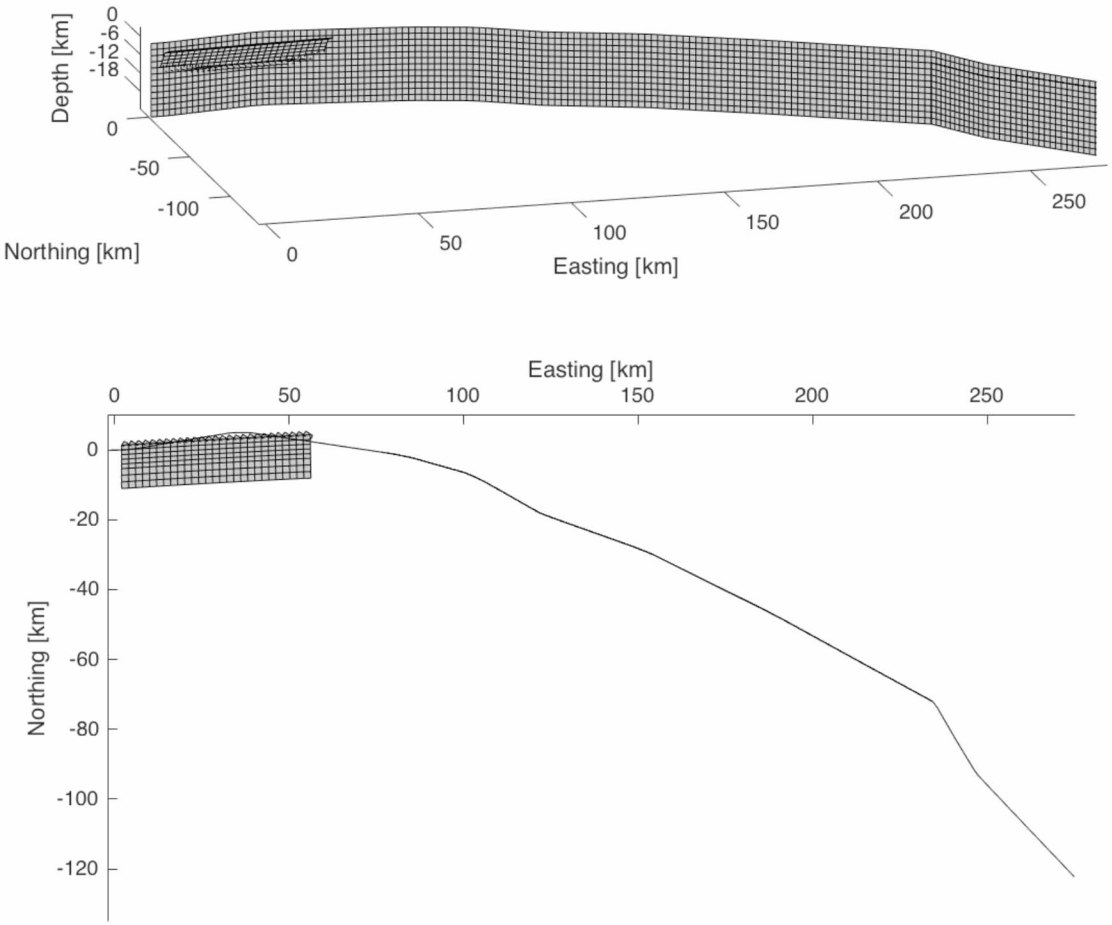

Figure 6. Discretization of the Susitna Glacier, Denali, and Totschunda faults, shown here in a local Cartesian coordinate system. Axis scales are in km.

4.1 Earth Model and Greens Function Calculations

The model uses the 1D ak135 elastic structure [*Kennett et al.*, 1995] and a spherical Earth (Figure 7). Greens functions are computed using a finite element method split-node

technique [*Melosh and Raefsky*, 1981]. To prevent slip singularities on nodes, unit slip is tapered linearly to zero halfway onto adjacent elements when calculating Greens functions for a certain element (shown in Figure 8), so a normalization factor of 2/3 is applied to all buried elements and 4/5 to all dip slip surface elements to maintain the proper moment.

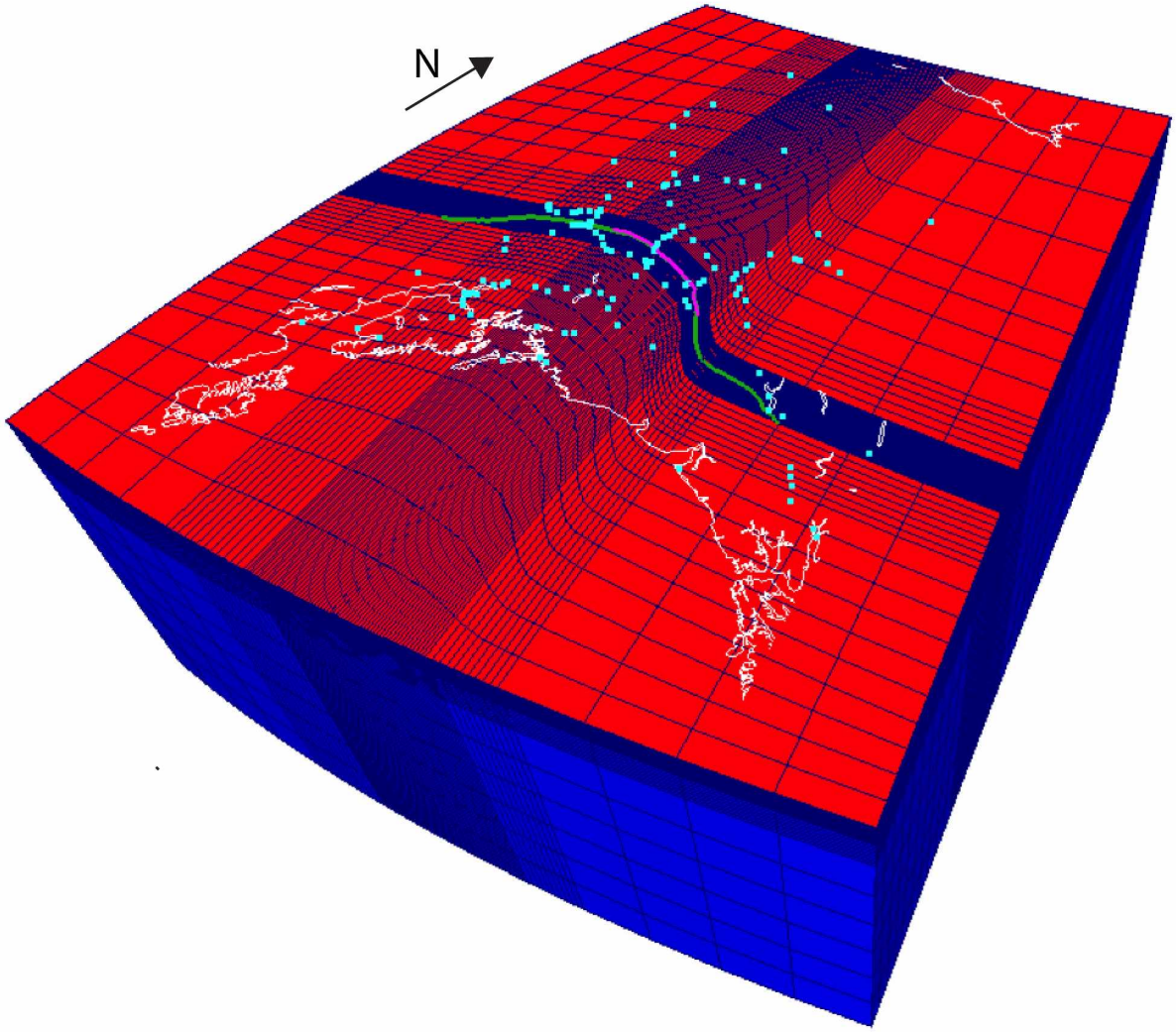

Figure 7. Central region of the finite element model mesh, used in both coseismic and postseismic deformation modeling. Elastic structure is based on the ak135 seismic velocity model. Magenta line is the extent of the rupture. Cyan dots are GPS sites. Figure courtesy of Yan Hu.

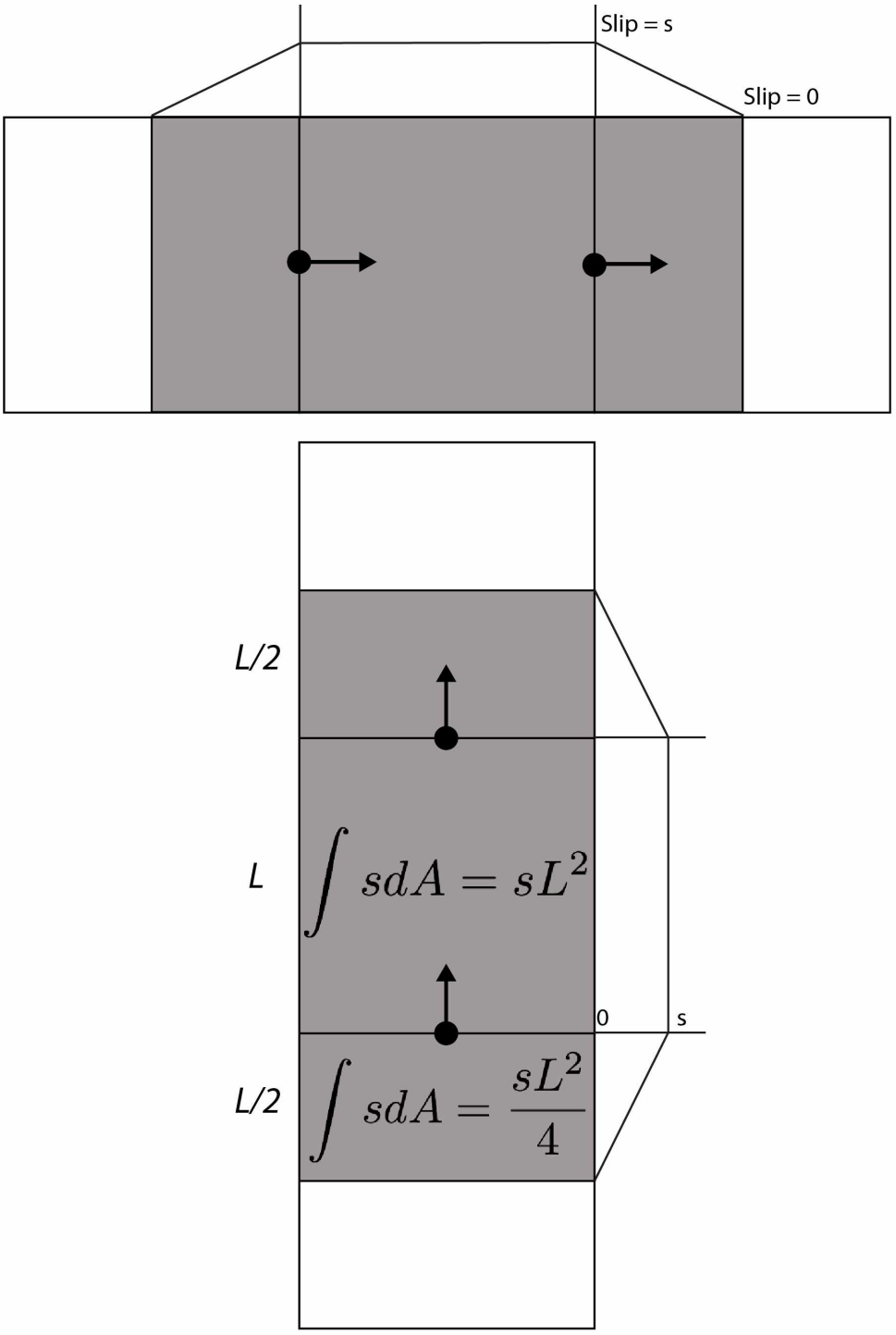

Figure 8. Forward model calculation of coseismic Greens functions using the finite element method (top shows strike-slip component, bottom shows dip slip). To avoid slip singularities at the edge of an element, slip is extended onto adjacent elements and tapered to zero. As a consequence, the calculated Greens functions must be scaled by a factor of 2/3. The dip slip component of surface elements are only scaled by 4/5.

Due to the proximity of some GPS sites and SAR data to the fault interface, it is necessary to replace the FEM-calculated Greens functions with analytical Greens functions (such as *Okada* [1985]) to avoid numerical instabilities or inaccuracy of the FEM-calculated Greens functions. Using smaller model elements would reduce the near-fault numerical instabilities but would increase computation time of Greens functions dramatically. Since some data are located within hundreds of meters of the fault, no practical amount of reduction in element size would produce completely negligible numerical instability. To rectify this, any element less than 14 km from a data point uses analytical Greens functions for that particular data point. Following this scheme, about 37,000 Greens functions replacements are made (out of about 11 million total).

4.2 Inversion Method

The inversion method employs a bounded-variables damped least squares solution, restricting coseismic slip to be right-lateral strike-slip and north-side-up dip slip. This is the same approach used in *Hreinsdóttir et al.* [2006] and *Elliott et al.* [2007], the only exception is a built-in MATLAB function is used, rather than the BVLS algorithm of [*Stark and Parker*, 1995]. Regularization of the solution uses a finite-difference approximated Laplacian operator to minimize the second spatial derivative of the slip distribution. The weight of the smoothing operator relative to the data is determined by the tradeoff of model WRSS and roughness norm, minimizing the objective function:

$$\|\mathbf{W}(\mathbf{Gs} - \mathbf{d})\|^2 + \beta^2\|\mathbf{Ls}\|^2$$

where $\mathbf{W}^T\mathbf{W} = \mathbf{\Sigma}^{-1}$ and $\mathbf{\Sigma}$ is the data covariance matrix, **L** is the Laplacian operator, and β is the smoothing weight factor.

The preferred model has a smoothing weight of β = 4 (Figure 9) and a total model WRSS of 4.03 x 10^3 m^2, and the slip distribution is shown in Figure 10. Model-predicted horizontal displacements are shown in Figure 11, and residual horizontal displacements are shown in Figure 12. Displacement values are given in Table 1. To illustrate the tradeoff between slip model resolution, roughness, and misfit, models with smoothing weights of β = 2 and β = 7 are shown in Figure 13. The basic characteristics of the slip distribution do not change for reasonable variation in the smoothing weight.

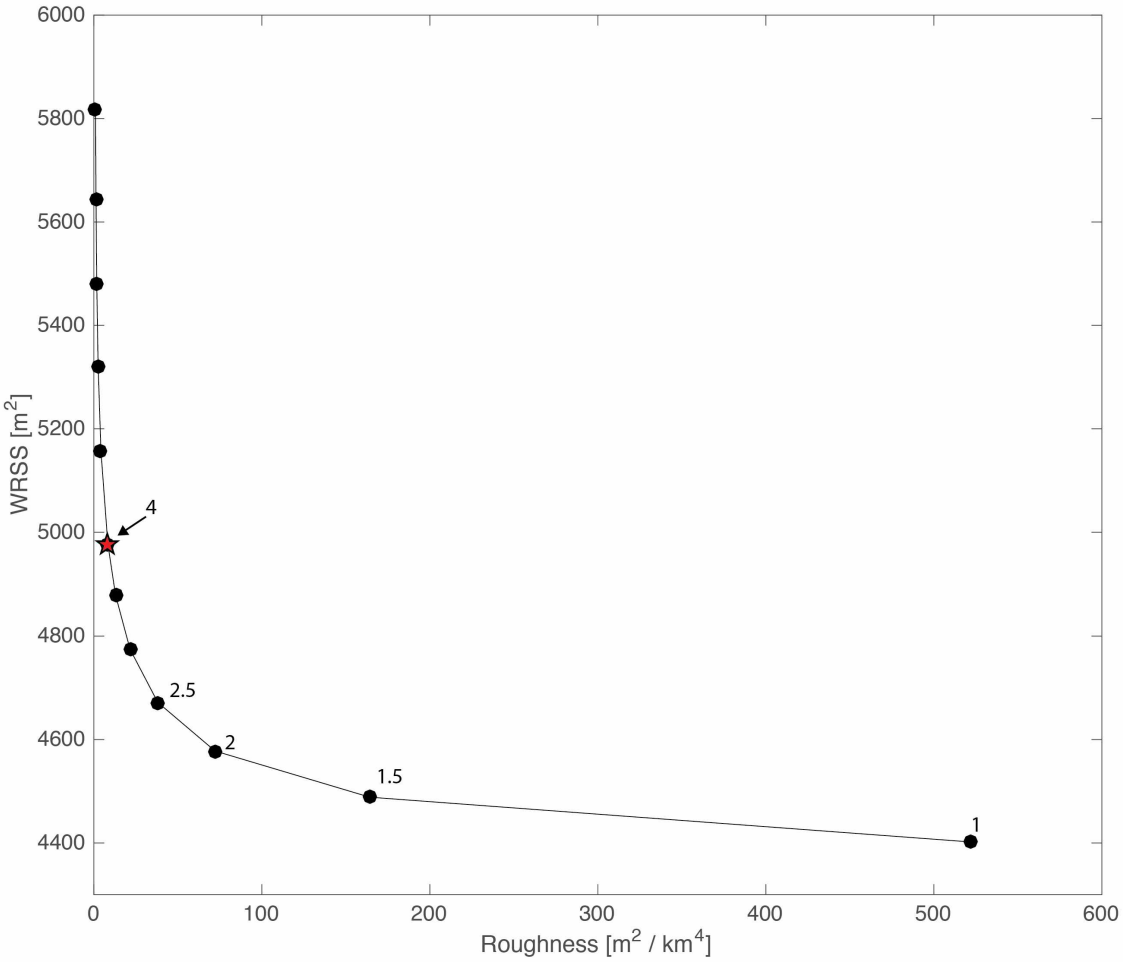

Figure 9. The L-curve for different smoothing values, β. β = 4 (red star) is the preferred smoothing value minimizing the tradeoff of misfit and roughness.

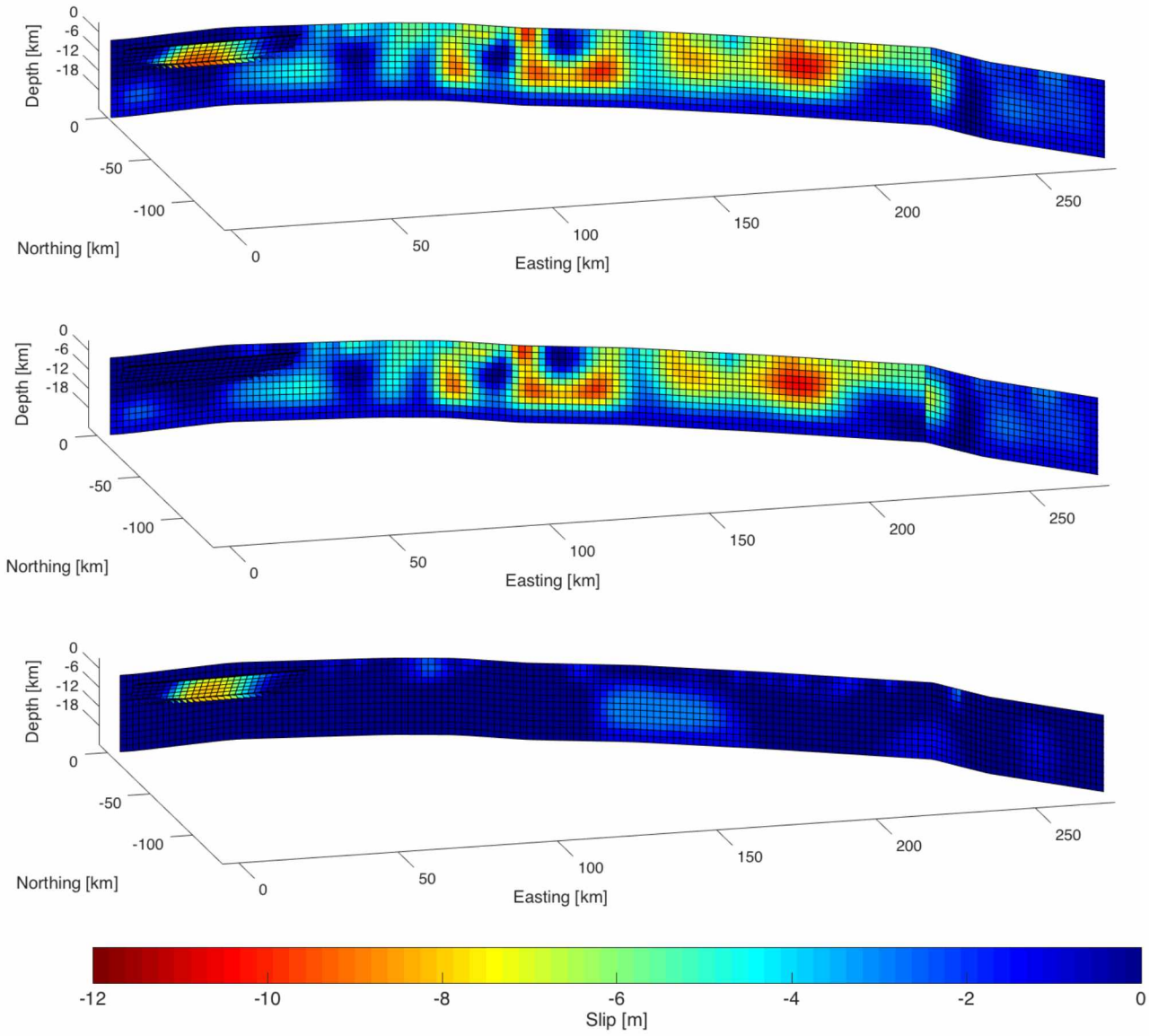

Figure 10. Coseismic slip distribution along the three faults for the preferred model (scale in meters). (a) Total slip magnitude; (b) strike-slip only; (c) dip slip only.

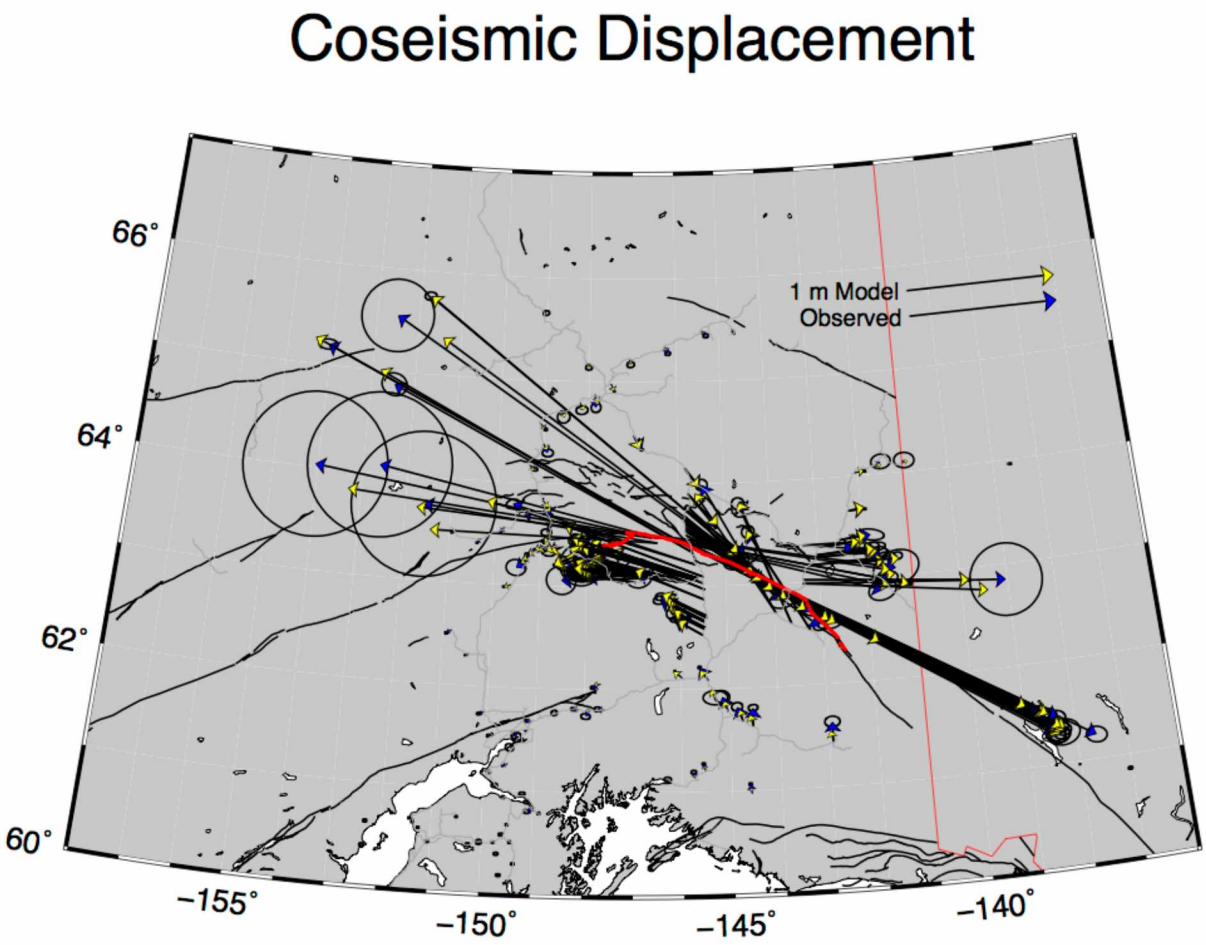

Figure 11. Observed and modeled coseismic surface displacements. Extent of rupture shown in red. Modeled displacements are in good agreement with the data and are typical of right-lateral strike-slip motion.

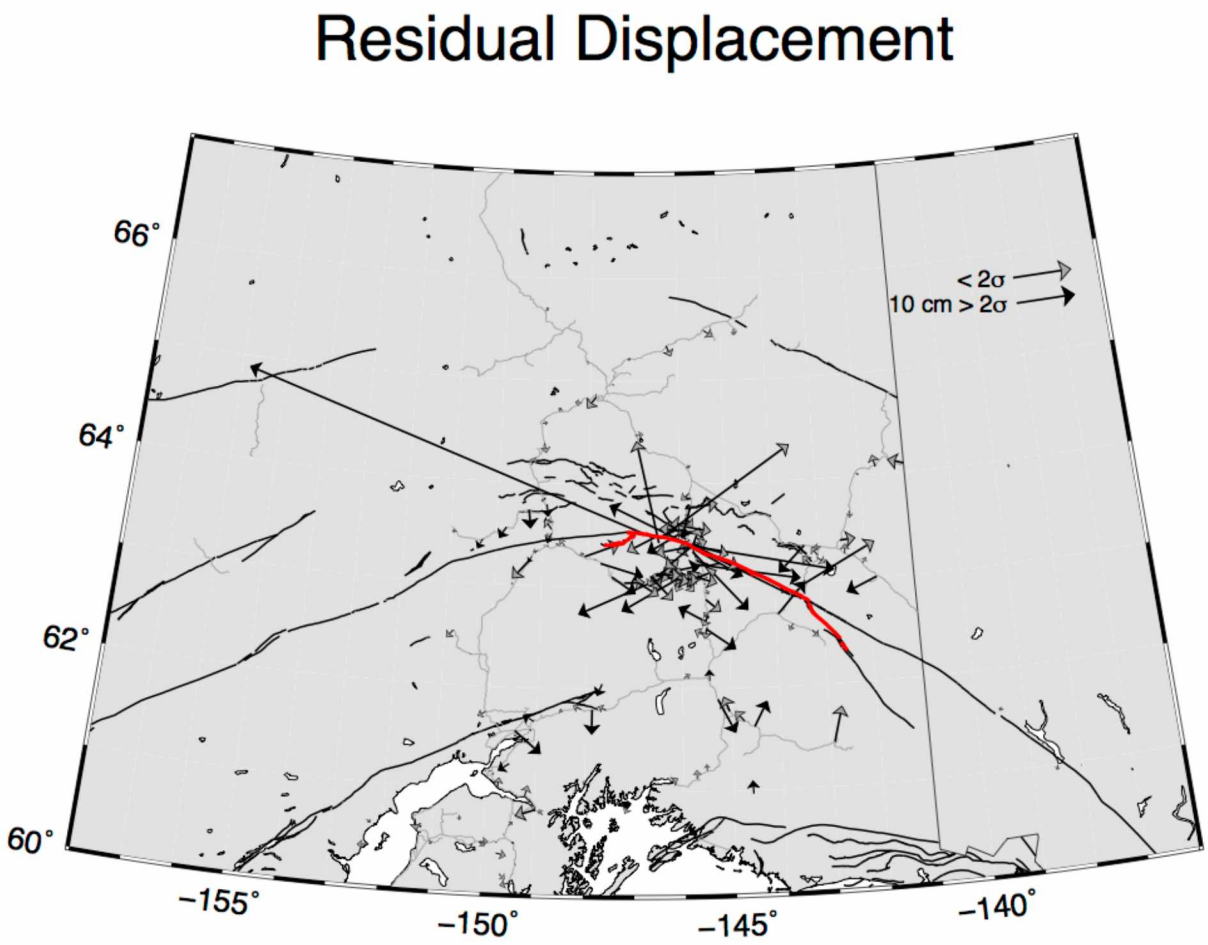

Figure 12. Residual coseismic displacements for the predicted slip model. Black vectors exceed twice the estimated error, gray do not. There doesn't appear to be any systematic bias in the residuals.

Table 1. Coseismic displacement estimates from GPS

Site	Lon.	Lat.	North (m)	East (m)	Up (m)	σ N	σ E	σ U
ELD	-135.2223	58.9720	0.001	0.002	0.004	0.002	0.003	0.005
FS32	-135.3470	59.1487	-0.001	-0.001	-0.002	0.003	0.008	0.008
HNSC	-135.5120	59.2425	-0.007	0.021	-0.015	0.006	0.024	0.016
HNSD	-135.5342	59.2481	-0.001	0.014	0.031	0.005	0.008	0.011
TNK1	-135.4405	59.2722	0.007	-0.022	0.011	0.003	0.009	0.012
STEP	-153.7648	59.4343	0.002	-0.016	0.007	0.005	0.007	0.014
MIDD	-146.3346	59.4346	0.014	0.000	-0.012	0.002	0.003	0.006
SELD	-151.7067	59.4457	-0.006	0.002	-0.002	0.001	0.001	0.002
TEM1	-135.3302	59.4502	0.002	0.002	0.003	0.001	0.001	0.003
YKTT	-139.6488	59.5107	0.019	-0.009	0.014	0.003	0.004	0.008
2201	-150.5514	59.5249	-0.001	0.004	0.015	0.003	0.005	0.009
HOMA	-151.4915	59.6390	-0.005	-0.003	0.015	0.004	0.005	0.011
COMB	-138.6393	59.6698	0.020	-0.008	-0.061	0.003	0.004	0.007
CC	-149.7479	59.6942	0.001	-0.002	0.070	0.003	0.004	0.011
HIDD	-138.9455	59.7055	0.017	0.005	-0.019	0.004	0.006	0.010
BRAD	-150.8519	59.7551	-0.008	-0.007	-0.019	0.001	0.002	0.004
ILIA	-154.8207	59.7633	0.008	-0.023	0.014	0.008	0.011	0.021
MOTG	-147.9078	59.8248	-0.003	0.009	-0.029	0.005	0.006	0.012
RGGI	-149.4072	59.8652	-0.004	0.004	0.021	0.001	0.002	0.004
NINI	-151.7158	60.0085	-0.001	-0.005	-0.001	0.003	0.005	0.010
UAMF	-149.4424	60.0985	-0.003	-0.022	-0.021	0.001	0.002	0.004
T19	-149.4286	60.1192	-0.006	-0.006	0.008	0.003	0.004	0.008
JANE	-149.6436	60.1830	-0.008	0.004	0.006	0.004	0.006	0.016
CHI4	-146.6465	60.2377	0.011	-0.004	0.006	0.003	0.004	0.005
K76	-149.3429	60.2860	0.000	-0.005	0.044	0.003	0.005	0.009
CPLK	-149.7209	60.3830	-0.004	0.010	0.018	0.004	0.006	0.013
HAR3	-152.2712	60.3903	-0.003	-0.024	0.004	0.004	0.006	0.013
BEAR	-150.2478	60.4554	-0.001	-0.002	0.007	0.005	0.007	0.014
SXQD	-151.0417	60.4759	-0.009	-0.005	0.000	0.003	0.004	0.009
EKG3	-151.8382	60.4846	-0.003	-0.006	-0.015	0.001	0.002	0.004
POPZ	-150.0558	60.4850	0.001	0.007	-0.018	0.007	0.007	0.021
POPL	-150.0640	60.4870	-0.008	0.001	0.006	0.003	0.004	0.008
CPR	-149.7454	60.4894	0.000	-0.006	-0.022	0.003	0.004	0.008
TRLK	-149.4203	60.5015	-0.004	-0.005	-0.003	0.003	0.003	0.008
GRAV	-149.5815	60.5644	0.002	-0.010	-0.008	0.004	0.006	0.015
DIAN	-151.2279	60.5879	0.004	-0.009	-0.008	0.003	0.004	0.008
QRRY	-152.3037	60.6299	-0.006	-0.001	-0.009	0.004	0.005	0.014
ROC	-147.9329	60.6537	0.007	-0.002	0.011	0.001	0.002	0.004
DAHL	-149.4879	60.6540	0.007	-0.004	-0.042	0.003	0.003	0.010

Table 1 continued

KEN1	-151.3502	60.6751	-0.023	-0.006	-0.006	0.002	0.004	0.005
NIK2	-151.3915	60.6853	-0.004	-0.014	-0.007	0.003	0.004	0.008
KSTN	-151.7544	60.7201	-0.003	-0.013	0.025	0.002	0.003	0.006
DIXI	-147.4464	60.7315	0.013	-0.011	0.005	0.002	0.003	0.006
MPEN	-150.4827	60.7352	-0.011	-0.009	-0.007	0.002	0.003	0.007
WHIT	-135.2221	60.7505	-0.001	0.005	0.007	0.001	0.002	0.003
PRTG	-148.8296	60.7712	0.010	-0.017	0.003	0.003	0.004	0.009
EGG	-147.9626	60.7740	0.009	-0.008	0.006	0.004	0.006	0.009
ENDI	-148.9757	60.8185	-0.011	-0.046	0.018	0.006	0.009	0.018
X7	-137.0629	60.8592	0.000	0.008	-0.014	0.004	0.006	0.012
GUY	-147.0959	60.8793	-0.004	-0.019	0.010	0.003	0.005	0.011
ALAS	-149.0639	60.8931	-0.001	-0.020	-0.012	0.004	0.007	0.015
TURN	-149.5433	60.9305	0.001	-0.018	-0.016	0.004	0.004	0.011
S72	-149.1954	60.9457	0.018	-0.008	0.010	0.004	0.008	0.014
MOTD	-138.0405	60.9577	0.007	0.006	0.018	0.001	0.001	0.003
BREM	-144.6056	60.9682	0.065	-0.009	0.012	0.004	0.005	0.011
NSLM	-138.4965	60.9927	-0.001	0.001	0.002	0.001	0.002	0.003
HAM	-148.0914	61.0056	0.007	-0.020	0.021	0.002	0.002	0.004
ISLZ	-149.7456	61.0207	0.015	-0.011	-0.008	0.006	0.008	0.019
POT3	-146.6968	61.0563	0.015	-0.010	0.011	0.001	0.002	0.003
COGH	-147.9471	61.0704	0.011	-0.022	-0.003	0.002	0.002	0.005
POWE	-146.3053	61.0837	0.029	0.003	0.070	0.006	0.010	0.022
THMP	-145.7323	61.1280	0.045	-0.013	0.035	0.005	0.007	0.016
CMJV	-149.8449	61.1658	-0.007	-0.014	0.012	0.001	0.001	0.002
ANC1	-149.9968	61.1824	-0.006	-0.013	0.000	0.001	0.001	0.002
TSEA	-149.8950	61.1873	-0.006	-0.017	0.004	0.001	0.001	0.002
TSIN	-145.5282	61.2036	0.047	-0.012	-0.002	0.003	0.004	0.009
DEST	-138.7219	61.2169	0.008	0.001	0.001	0.002	0.002	0.005
EAGL	-149.5287	61.2575	-0.016	-0.035	0.006	0.001	0.001	0.002
NWOD	-149.4510	61.4209	-0.002	-0.018	-0.033	0.009	0.012	0.028
MCAR	-142.9204	61.4320	0.137	0.001	-0.071	0.015	0.021	0.048
FSHL	-149.8824	61.5247	-0.004	-0.024	-0.021	0.003	0.003	0.009
REED	-149.3959	61.5424	-0.008	-0.025	-0.008	0.001	0.001	0.003
S1	-149.4418	61.5805	-0.044	0.025	0.019	0.013	0.013	0.015
Y565	-139.4449	61.5927	0.012	0.000	0.010	0.001	0.001	0.003
ATW2	-149.1323	61.5978	-0.009	-0.020	-0.001	0.001	0.001	0.002
LIBF	-144.5359	61.6202	0.127	0.004	0.022	0.009	0.013	0.023
BUMP	-144.7369	61.6753	0.100	-0.038	0.011	0.012	0.015	0.031
MOS2	-149.0560	61.6756	0.005	-0.044	-0.029	0.003	0.005	0.010
Z22A	-150.0524	61.7542	-0.015	-0.035	-0.029	0.003	0.006	0.008

Table 1 continued

CKLN	-148.5368	61.7647	0.001	-0.025	0.007	0.006	0.008	0.016
KENN	-145.0369	61.7756	0.101	-0.039	0.040	0.016	0.021	0.020
SHPA	-147.5756	61.7998	0.007	-0.049	-0.059	0.006	0.009	0.020
RD44	-147.8664	61.8026	-0.045	-0.034	-0.064	0.008	0.013	0.024
PURI	-148.0894	61.8046	0.002	-0.047	-0.004	0.004	0.005	0.012
WILL	-145.2714	61.8951	0.012	-0.007	0.043	0.020	0.034	0.052
LSG1	-147.6658	62.0533	-0.023	-0.055	0.006	0.004	0.005	0.012
TAZL	-145.4329	62.0799	0.092	-0.057	0.004	0.003	0.004	0.010
GNAA	-145.9702	62.1124	0.048	-0.050	0.005	0.001	0.002	0.004
TLKA	-150.4203	62.3077	-0.010	-0.028	-0.013	0.001	0.002	0.004
O8	-145.5156	62.5229	0.112	-0.190	0.003	0.007	0.012	0.018
FLY	-143.2483	62.5284	0.691	-0.384	0.058	0.016	0.017	0.027
PTVL	-150.8167	62.5317	-0.023	-0.036	-0.007	0.003	0.004	0.010
Y61	-145.4809	62.5823	0.082	-0.156	-0.016	0.015	0.018	0.030
X61	-145.4599	62.5968	0.104	-0.221	-0.054	0.014	0.016	0.032
V61	-145.4847	62.6523	0.158	-0.296	0.033	0.010	0.018	0.029
SOUR	-145.4837	62.6639	0.146	-0.256	-0.007	0.008	0.009	0.015
7297	-145.4261	62.6880	0.162	-0.291	-0.016	0.003	0.003	0.007
SLBR	-143.9474	62.7048	0.897	-0.466	0.064	0.016	0.016	0.022
HOME	-145.4313	62.7133	0.139	-0.311	-0.039	0.008	0.013	0.021
MEN	-143.7953	62.9095	2.137	-2.269	-0.268	0.011	0.016	0.033
PAXS	-145.4517	62.9673	0.272	-0.620	-0.056	0.002	0.003	0.007
HURR	-149.6089	62.9993	-0.015	-0.048	-0.016	0.002	0.003	0.006
NJNC	-141.8000	63.0099	-0.013	0.085	-0.031	0.017	0.028	0.055
LOG	-143.3454	63.0226	-0.074	1.118	0.067	0.003	0.004	0.009
G63	-145.5012	63.0314	0.301	-0.746	-0.040	0.014	0.014	0.012
K112	-147.2128	63.0371	0.090	-0.249	-0.217	0.027	0.045	0.094
U113	-145.8880	63.0420	0.147	-0.605	-0.026	0.016	0.020	0.024
W112	-146.9227	63.0436	0.048	-0.326	-0.007	0.016	0.015	0.020
S113	-145.8443	63.0447	0.204	-0.685	-0.025	0.004	0.006	0.012
Z113	-146.0227	63.0454	0.133	-0.550	-0.042	0.014	0.014	0.014
Y113	-145.9966	63.0473	0.118	-0.596	-0.032	0.017	0.021	0.021
V113	-145.9161	63.0474	0.174	-0.592	-0.045	0.015	0.016	0.015
X113	-145.9748	63.0513	0.155	-0.590	-0.031	0.014	0.013	0.013
B122	-146.0743	63.0586	0.124	-0.554	-0.066	0.015	0.017	0.016
M113	-145.7170	63.0657	0.244	-0.767	-0.107	0.015	0.021	0.019
C122	-146.1008	63.0672	0.061	-0.675	-0.001	0.019	0.028	0.024
E113	-145.5909	63.0703	0.289	-0.823	-0.044	0.015	0.019	0.017
GL22	-146.1809	63.0734	0.090	-0.525	-0.090	0.014	0.018	0.018
F122	-146.1530	63.0744	0.098	-0.533	-0.092	0.016	0.022	0.023

Table 1 continued

L113	-145.7022	63.0777	0.259	-0.774	-0.071	0.014	0.013	0.010
K113	-145.6753	63.0784	0.275	-0.767	-0.083	0.015	0.020	0.018
D122	-146.1152	63.0793	0.132	-0.590	-0.044	0.013	0.012	0.009
F113	-145.6071	63.0835	0.286	-0.818	-0.065	0.014	0.013	0.011
R122	-146.4241	63.0879	0.052	-0.522	-0.084	0.014	0.013	0.013
Q122	-146.4000	63.0885	-0.006	-0.672	-0.012	0.032	0.039	0.088
FCRK	-145.4753	63.0907	0.380	-0.930	-0.076	0.002	0.002	0.005
L122	-146.2839	63.0912	0.067	-0.534	-0.173	0.022	0.029	0.030
S122	-146.4368	63.0930	0.056	-0.541	-0.072	0.014	0.013	0.013
Y111	-147.4846	63.0968	0.083	-0.198	-0.051	0.041	0.048	0.069
T122	-146.4433	63.1002	0.058	-0.527	-0.032	0.014	0.014	0.012
B123	-146.6208	63.1019	0.031	-0.480	0.016	0.017	0.035	0.036
C123	-146.6535	63.1044	0.016	-0.453	-0.040	0.019	0.033	0.040
AL23	-146.5962	63.1055	0.036	-0.515	-0.080	0.015	0.020	0.021
U122	-146.4534	63.1094	0.039	-0.497	-0.048	0.021	0.032	0.040
Z122	-146.5717	63.1165	0.067	-0.451	-0.106	0.015	0.021	0.020
Y122	-146.5427	63.1185	0.045	-0.517	-0.100	0.017	0.024	0.027
V122	-146.4614	63.1201	0.075	-0.529	-0.041	0.014	0.015	0.013
X122	-146.5116	63.1237	0.048	-0.515	-0.057	0.014	0.014	0.016
S174	-142.0812	63.1504	0.017	0.171	-0.037	0.017	0.026	0.054
TRAI	-143.1999	63.1611	0.025	0.600	-0.082	0.010	0.013	0.025
C96	-145.6389	63.2115	0.447	-1.226	-0.087	0.010	0.018	0.021
N111	-147.7264	63.2263	0.088	-0.128	-0.035	0.020	0.027	0.041
H34	-143.0517	63.2340	0.006	0.438	-0.154	0.014	0.020	0.040
RAND	-149.2550	63.2507	-0.056	-0.082	0.089	0.022	0.027	0.048
LADU	-142.4529	63.2543	0.029	0.217	-0.034	0.012	0.029	0.048
TP26	-143.0390	63.2547	0.033	0.390	-0.032	0.011	0.016	0.032
DH97	-147.8550	63.2652	0.013	-0.188	-0.047	0.001	0.001	0.002
PISA	-149.2105	63.2847	-0.034	-0.060	-0.007	0.002	0.003	0.006
R110	-148.0751	63.2922	-0.048	-0.124	-0.058	0.020	0.025	0.045
M110	-148.1870	63.3055	-0.068	-0.159	-0.041	0.002	0.003	0.005
STRI	-142.9531	63.3334	0.022	0.294	-0.039	0.004	0.006	0.011
P592	-145.7353	63.3397	1.186	-1.978	-0.367	0.023	0.033	0.058
SSWB	-149.0902	63.3413	-0.028	-0.061	-0.010	0.004	0.006	0.012
TWB1	-143.3161	63.3593	-0.043	0.340	-0.106	0.011	0.017	0.034
MILC	-145.7318	63.3737	1.447	-2.420	-0.705	0.013	0.026	0.033
L2C6	-148.8662	63.3828	-0.029	-0.060	-0.012	0.002	0.003	0.007
E175	-142.5298	63.3868	0.021	0.219	-0.179	0.011	0.037	0.033
FM09	-145.7330	63.3875	-1.328	2.480	0.281	0.016	0.023	0.043
FM10	-145.7350	63.3879	-1.346	2.446	0.291	0.018	0.024	0.048

Table 1 continued

CGLO	-148.9496	63.3883	-0.027	-0.054	-0.014	0.003	0.003	0.007
FM08	-145.7332	63.3883	-1.320	2.487	0.344	0.033	0.046	0.062
FM07	-145.7358	63.3887	-1.300	2.483	0.294	0.017	0.024	0.045
W109	-148.5067	63.3898	-0.035	-0.098	0.059	0.013	0.020	0.037
FM06	-145.7416	63.3918	-1.321	2.437	0.268	0.020	0.027	0.051
FM05	-145.7390	63.3925	-1.343	2.714	0.390	0.022	0.029	0.047
FM03	-145.7425	63.3931	-1.330	2.460	0.301	0.020	0.029	0.058
FM04	-145.7395	63.3933	-1.281	2.461	0.218	0.019	0.026	0.046
R109	-148.6468	63.3953	-0.036	-0.076	-0.019	0.002	0.002	0.005
FM01	-145.7412	63.4059	-1.214	2.381	0.209	0.018	0.027	0.048
FM02	-145.7439	63.4060	-1.230	2.453	0.166	0.017	0.022	0.045
P586	-145.7463	63.4112	-1.203	2.322	0.323	0.019	0.034	0.049
M126	-150.2970	63.4330	-0.028	-0.028	0.010	0.002	0.002	0.004
HIW4	-148.8073	63.4643	-0.032	-0.039	-0.016	0.001	0.002	0.003
PANA	-148.8204	63.4837	-0.033	-0.044	-0.022	0.002	0.003	0.007
WOND	-150.8737	63.4912	-0.008	-0.022	-0.017	0.002	0.002	0.004
BRBA	-146.4898	63.4930	-0.346	1.708	0.209	0.003	0.006	0.009
BRWE	-146.5081	63.4943	-0.385	1.532	0.298	0.018	0.037	0.044
BRLA	-146.3888	63.4945	-0.239	1.586	-0.111	0.031	0.061	0.052
ATT	-145.8472	63.5025	-0.754	1.300	-0.012	0.002	0.003	0.007
SLIM	-148.8041	63.5120	-0.053	-0.032	-0.037	0.003	0.003	0.008
CRK1	-145.8646	63.5443	-0.646	0.965	-0.119	0.015	0.033	0.036
CARL	-148.8089	63.5515	-0.022	-0.024	-0.086	0.010	0.014	0.034
CRK2	-145.8673	63.5523	-0.673	0.899	-0.095	0.011	0.017	0.025
EFRK	-149.7940	63.5592	-0.035	-0.027	-0.002	0.002	0.002	0.005
N101	-145.8665	63.5814	-0.592	0.854	-0.082	0.012	0.024	0.029
L101	-145.8643	63.6132	-0.530	0.654	-0.033	0.018	0.036	0.047
H101	-145.8913	63.6413	-0.490	0.609	-0.018	0.008	0.010	0.016
GRIZ	-148.8330	63.6524	-0.052	0.003	-0.010	0.003	0.004	0.009
0999	-142.2748	63.6650	0.004	0.113	-0.042	0.003	0.003	0.007
F101	-145.8855	63.6704	-0.455	0.535	-0.046	0.010	0.015	0.021
DNLY	-145.8876	63.6951	-0.406	0.470	0.006	0.002	0.003	0.006
B124	-149.3088	63.7349	-0.062	0.010	0.045	0.001	0.002	0.003
H7	-145.8554	63.7601	-0.323	0.404	-0.266	0.020	0.031	0.055
P100	-145.7697	63.7680	-0.369	0.314	0.104	0.018	0.034	0.048
DFLY	-148.9198	63.7936	-0.075	0.035	0.004	0.004	0.006	0.014
GRNR	-148.9783	63.8358	-0.053	0.025	0.011	0.001	0.002	0.003
BSB4	-145.7891	63.9065	-0.232	0.186	0.031	0.003	0.004	0.008
8130	-138.6944	63.9585	-0.001	0.025	0.021	0.002	0.003	0.008
2999	-142.0761	64.0287	0.006	0.070	-0.027	0.003	0.003	0.007

Table 1 continued

W176	-141.6326	64.0757	0.030	0.048	-0.112	0.020	0.027	0.053
126G	-141.0013	64.0865	0.018	0.015	-0.078	0.021	0.028	0.061
PPLN	-145.8461	64.1549	-0.132	0.100	0.039	0.004	0.005	0.007
BRWN	-149.2951	64.1707	-0.027	0.033	0.015	0.005	0.008	0.017
Z117	-149.0139	64.3885	-0.065	0.032	0.070	0.011	0.015	0.028
SLCH	-146.9764	64.4767	-0.097	0.055	0.029	0.003	0.004	0.007
NENA	-149.0798	64.5794	-0.039	0.033	0.014	0.003	0.004	0.011
S119	-148.6249	64.7105	-0.043	0.017	-0.008	0.014	0.016	0.033
M120	-148.2001	64.7914	-0.051	0.013	0.107	0.011	0.016	0.030
RIDG	-147.8646	64.8496	-0.072	0.008	0.060	0.010	0.012	0.016
CLGO	-147.8605	64.8738	-0.053	0.020	0.019	0.001	0.002	0.003
FAIR	-147.4992	64.9780	-0.052	0.023	0.029	0.001	0.002	0.004
WICK	-148.0662	65.1827	-0.033	0.016	-0.005	0.007	0.009	0.021
SPIL	-147.0844	65.2268	-0.043	0.011	-0.096	0.007	0.010	0.023
FAIT	-146.2610	65.3471	-0.052	0.022	0.023	0.005	0.007	0.015
EGL2	-145.3875	65.4909	-0.036	0.027	0.022	0.005	0.007	0.015
CENA	-144.6776	65.4982	-0.032	0.012	0.020	0.001	0.002	0.003
YUKO	-149.0930	65.6762	-0.014	0.016	-0.004	0.006	0.009	0.020
BRPO	-146.5818	63.4786	0.535	-2.268	0.000	0.200	0.200	1.000
BROZ	-146.4658	63.4284	0.291	-1.574	0.000	0.200	0.200	1.000
BRSR	-146.4341	63.4730	0.532	-1.877	0.000	0.200	0.200	1.000
JOIN	-145.4772	62.8711	0.190	-0.440	0.070	0.040	0.040	0.200
SICH	-143.3545	62.9876	-0.060	1.370	0.040	0.100	0.100	0.200
MACL	-143.6800	62.8882	2.040	-2.530	-0.200	0.100	0.100	0.200
MAT	-143.6418	62.6054	0.829	-0.322	0.107	0.016	0.017	0.024

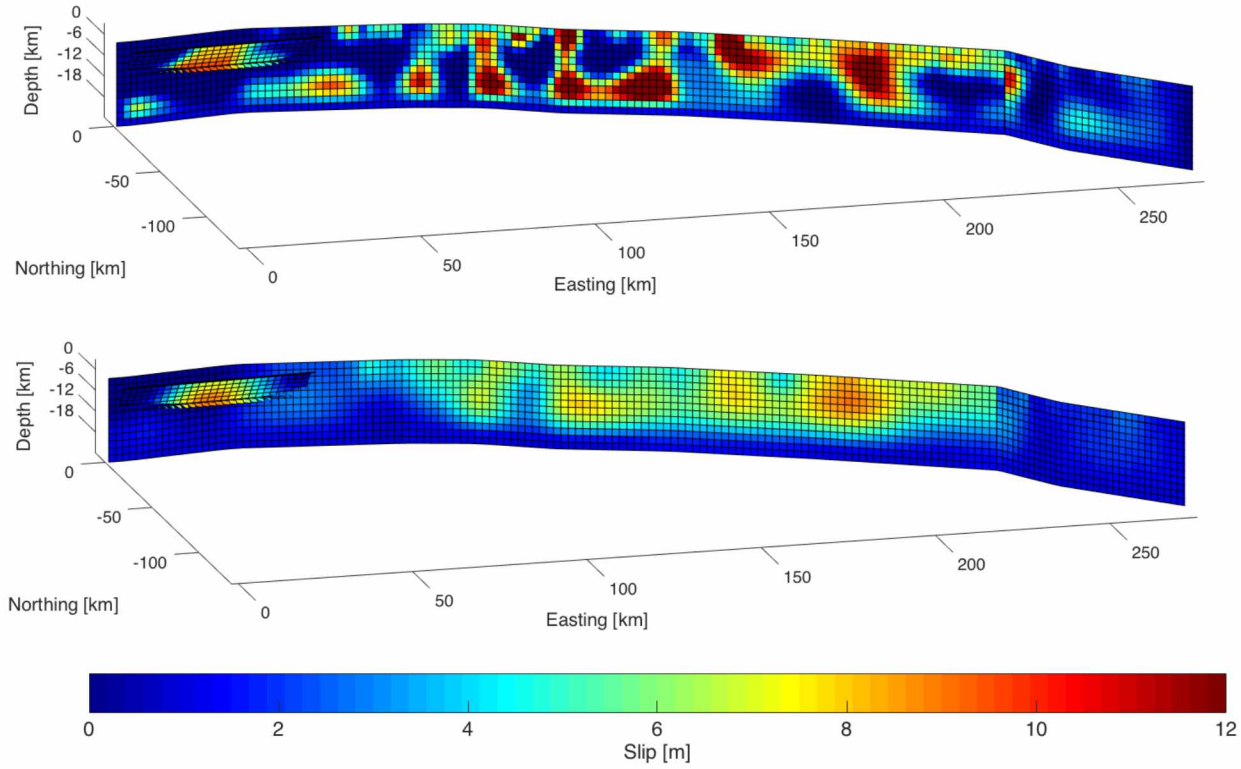

Figure 13. Slip models with a smoothing coefficient β = 2 (Top) and β = 7 (Bottom). The effect of the smoothing coefficient on slip distribution is very clear: a lower coefficient allows for a coarse slip distribution, but lower model misfit, and vice versa.

Inverting the displacements using the 1D spherical Earth model requires additional constraints. Slip must be restricted on the deepest model elements; not doing so puts maximum slip at 24 km depth, suggesting even deeper slip is required which is not a likely scenario [*Elliott et al.*, 2007]. Adding this restriction doesn't greatly affect misfit (Table 2). Different degrees of restriction were applied, but overall slip distribution patterns remain similar (Figures 14 and 15). Overall, the differences between the new 1D elastic coseismic model and previous models are not very different—i.e., major slip patches occur in the same areas along the fault—but the deeper slip distribution of the new model eliminates the need to artificially apply deep slip (see Discussion, Chapter 7).

Table 2. WRSS for different coseismic slip models

Model	GPS WRSS	SAR WRSS	Surface WRSS	Total WRSS	Roughness
Okada	3.88e3	6.30e2	54.9	4.56e3	6.57
Okada, 1m constraints	3.92e3	6.29e2	55.5	4.60e3	8.30
1D	4.05e3	6.07e2	54.2	4.71e3	6.57
1D, 1m constraints	4.31e3	6.08e2	53.8	4.98e3	8.37
1D, 3m constraints	4.19e3	6.08e2	53.5	4.86e3	6.35

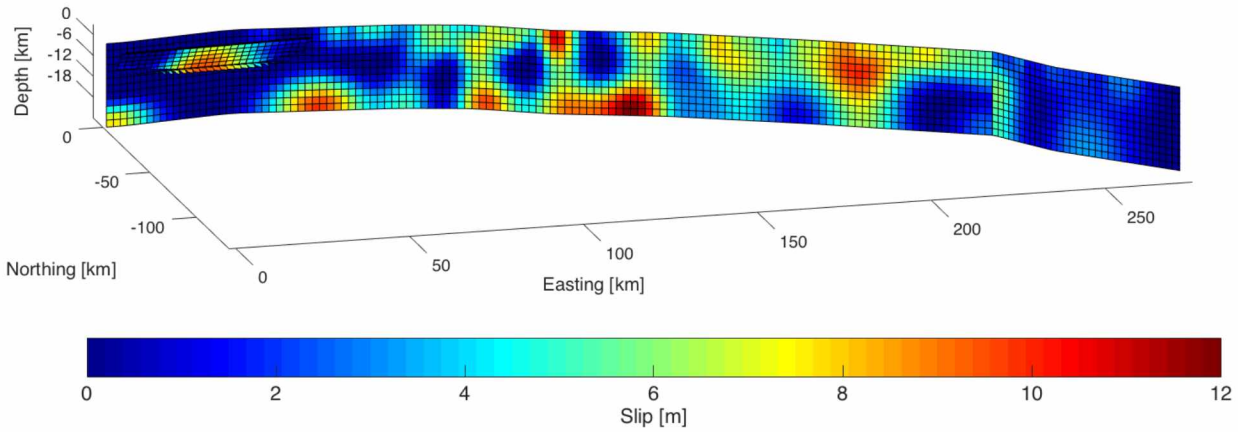

Figure 14. Coseismic slip distribution using FEM-calculated Greens functions with no fault edge slip constraints in the inversion. The deep slip across the fault is unlikely given its separation from surface slip. Previous studies showed it was unlikely slip occurred deeper than 24 km, so it is necessary to constrain slip at depth.

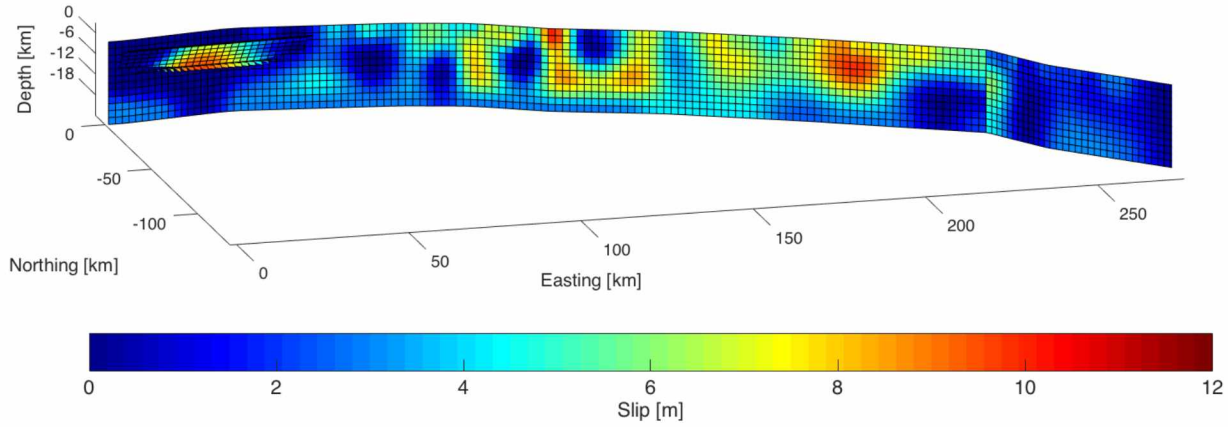

Figure 15. Coseismic slip distribution with slip restricted to 3 meters on the deepest patches. Maximum slip is less than the 1-meter constraint model, but slip is more broadly distributed.

Chapter 5 Postseismic Time Series Processing

5.1 Approaches to Fitting Time Series

To study postseismic displacement, it is necessary to parameterize GPS time series to both isolate the transient signal and allow for resampling to common epochs at all GPS sites. The continuous time series are fit with the following equation:

$$y = a + bt + c\sin(2\pi t) + d\cos(2\pi t) + e\sin(4\pi t) + f\cos(4\pi t) + H(t - t_d)[g + h\ln\left(1 + \left(\frac{t - t_d}{\tau_L}\right)\right) + k\left(1 - e^{-(t-t_d)/\tau_E}\right)]$$

where a, *b, c, d, e, f, g, h,* and *k* are all estimated by a least squares inversion. The periodic terms are standard parameterizations of annual and semi-annual variations. $H(t - t_d)$ is the Heaviside function where t_d is the time of the earthquake. τ_L and τ_E are the decay constants for, respectively, the logarithmic and exponential decay functions, which parameterize the postseismic transient signal. There are several different functions or combinations thereof that can be used for this purpose. In certain time series (Figure 16), postseismic displacements show an early trend of subsidence followed by uplift, so it is necessary that two decay functions be used. *Tobita* [2016] attempts to fit postseismic time series of the 2011 Mw9.0 Tohoku-Oki earthquake with superposition of three decay functions, adding another logarithmic or exponential parameter. The addition of a third parameter in fitting continuous time series with complete records is preferable based on an F-test metric, but because many time series to be fit are campaign GPS data (which also exclude the annual/semi-annual terms in their parameterization), or continuous sites established several months after the earthquake, the two parameter fit is used here to prevent “overfitting” the data.

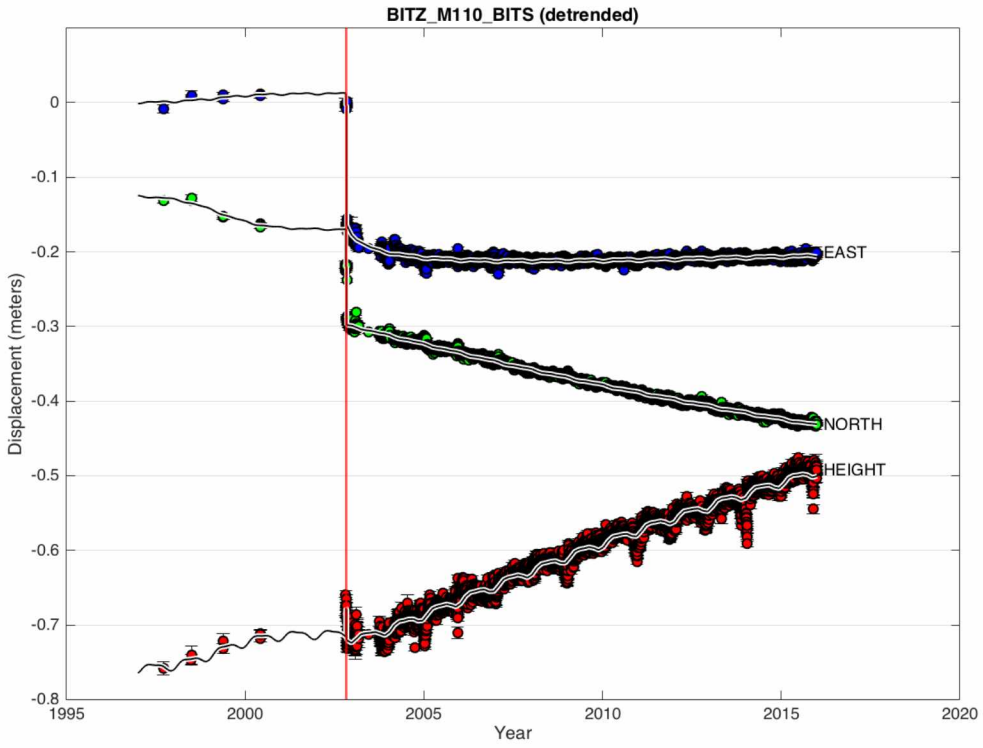

Figure 16. The need for multiple decay functions in the time series fit can be seen here in the east component, where the initial transient displacement trends west but, over time, trends back eastward. (Note: this site records a slow-slip event in the pre-earthquake time series).

To determine what deformation in a time series is transient and not secular, the secular velocity at that site must be estimated—this requires a record of pre-earthquake deformation. Many of the GPS sites in the postseismic dataset have little or no pre-earthquake data, making it impossible to fit the time series directly, and the secular velocity must be estimated by some other method**.** Using a method of 2D spatial interpolation, interseismic velocities are estimated for all sites. The time series can then be fit with equation 1, using the interpolated velocities as a priori estimates for *b*. Interpolated horizontal secular velocities for all postseismic sites are shown in Figure 17 (and listed in Table 3).

Table 3: Interpolated site velocities (NOAM-fixed)

Site	Lon.	Lat.	East (cm/yr)	North (cm/yr)
0999	-142.2748	63.6650	0.01	-0.26
126G	-141.0013	64.0865	0.02	-0.09
152T	-150.6735	66.8208	0.07	-0.34
299C	-142.0758	64.0289	0.00	-0.19
4240	-146.3596	61.1272	-1.27	2.30
AB41	-141.1581	64.7773	0.01	-0.08
AC11	-148.3317	61.8071	-0.57	0.83
ANC1	-149.9968	61.1824	-0.22	-0.15
ATT	-145.8472	63.5025	-0.21	0.16
ATTC	-145.8472	63.5024	-0.21	0.16
ATW2	-149.1323	61.5978	-0.89	0.41
B124	-149.3088	63.7349	0.04	-0.02
BEA2	-140.8625	62.4078	-0.07	0.21
BITS	-148.1883	63.3047	-0.81	-0.47
BREM	-144.6056	60.9682	-1.44	2.44
BRWN	-149.2951	64.1707	-0.01	-0.33
BSB4	-145.7891	63.9065	-0.19	-0.18
BUZZ	-143.3521	62.9638	-0.10	-0.07
C125	-149.6304	63.5737	0.04	-0.14
CENA	-144.6776	65.4982	0.00	-0.12
CHI3	-146.6466	60.2375	-1.00	5.00
CKLN	-148.5368	61.7647	-0.69	0.75
CLGO	-147.8605	64.8738	0.07	-0.31
CODO	-145.4754	60.4937	-1.37	3.35
DENN	-142.1757	63.9552	0.00	-0.21
DFLY	-148.9198	63.7936	-0.07	-0.04
DH32	-146.3127	63.0836	-0.38	0.14
DH34	-146.3658	63.0862	-0.40	0.13
DH97	-147.8550	63.2652	-0.86	-0.50
DLTJ	-145.7136	64.0493	-0.17	-0.25
DMC3	-144.8897	63.8192	-0.14	-0.12
DNL3	-143.3405	63.3723	-0.10	-0.26
DNLC	-145.8877	63.6951	-0.21	0.01
DRMC	-144.3040	62.7140	-0.24	0.17
E175	-142.5298	63.3868	0.01	-0.29
EAAA	-141.1601	64.7787	0.01	-0.08
EFRK	-149.7940	63.5592	0.03	-0.27
EGL2	-145.3875	65.4909	-0.04	-0.16
EIL1	-147.1130	64.6879	0.11	-0.29

Table 3 continued

EYAC	-145.7499	60.5487	-1.35	3.45
F101	-145.8855	63.6704	-0.21	0.03
FAIR	-147.4992	64.9780	0.15	-0.31
FCRK	-145.4753	63.0907	-0.26	0.16
FLY	-143.2483	62.5284	-0.18	0.14
FM02	-145.7439	63.4060	-0.22	0.18
FM04	-145.7395	63.3933	-0.22	0.18
FM10	-145.7350	63.3879	-0.22	0.18
FM11	-145.7330	63.3820	-0.22	0.18
FM12	-145.7304	63.3818	-0.22	0.18
FNGR	-150.4924	66.3755	0.07	-0.36
FRIG	-143.0052	62.4109	-0.19	0.17
GDNR	-141.5119	62.8928	0.11	-0.06
GNAA	-145.9702	62.1124	-0.58	0.76
GRIZ	-148.8330	63.6524	-0.16	0.04
GRNR	-148.9783	63.8358	-0.04	-0.07
GRNX	-148.9782	63.8355	-0.04	-0.07
HIWC	-148.8073	63.4644	-0.23	0.09
HURC	-149.6088	62.9993	-0.14	-0.45
I177	-141.1776	64.0861	0.02	-0.11
ISLZ	-149.7456	61.0207	-0.44	0.38
JANL	-143.9057	63.5685	-0.12	-0.18
KNOZ	-147.2443	63.0393	-0.56	-0.07
L2C6	-148.8662	63.3828	-0.20	0.10
LADU	-142.4529	63.2543	0.05	-0.25
LIBF	-144.5359	61.6202	-0.73	1.12
LOGC	-143.3454	63.0226	-0.09	-0.10
LSG1	-147.6658	62.0533	-0.33	0.77
LUCI	-145.6753	63.0780	-0.29	0.18
M126	-150.2970	63.4330	0.06	-0.60
M175	-142.3790	63.5488	0.01	-0.29
MACL	-143.6800	62.8881	-0.15	0.01
MCAR	-142.9204	61.4320	-0.58	0.62
MEN	-143.7953	62.9095	-0.16	0.02
MENT	-143.7042	62.8315	-0.16	0.04
MOS2	-149.0560	61.6756	-0.82	0.42
NENA	-149.0798	64.5794	-0.10	-0.45
O8	-145.5156	62.5229	-0.39	0.39
ORTT	-141.9364	62.9610	0.16	-0.14
P100	-145.7697	63.7680	-0.19	-0.06

Table 3 continued

P592	-145.7354	63.3397	-0.23	0.19
PANA	-148.8204	63.4837	-0.22	0.10
PAX2	-145.4519	62.9673	-0.29	0.18
PAXC	-145.4524	62.9692	-0.29	0.18
PISA	-149.2105	63.2847	-0.09	0.02
PIT2	-146.3999	62.0789	-0.59	0.81
POT3	-146.6968	61.0563	-1.32	2.29
PTVL	-150.8167	62.5317	0.14	-0.80
PURI	-148.0894	61.8046	-0.54	0.97
Q112	-147.0855	63.0377	-0.53	-0.03
R109	-148.6468	63.3953	-0.40	-0.07
RBOW	-145.6869	63.3109	-0.23	0.18
REED	-149.3959	61.5424	-0.68	0.08
ROLL	-143.2969	62.5358	-0.19	0.14
S103	-149.8706	61.6443	-0.13	-0.60
SDOU	-145.4263	62.6880	-0.34	0.29
SELD	-151.7067	59.4457	0.12	-0.82
SG27	-156.6103	71.3229	0.04	-0.11
SHPA	-147.5756	61.7998	-0.61	1.10
SLCH	-146.9764	64.4767	0.02	-0.26
SLIM	-148.8041	63.5120	-0.23	0.08
SOUR	-145.4837	62.6639	-0.35	0.31
SPIL	-147.0844	65.2268	0.14	-0.32
SSWB	-149.0902	63.3413	-0.09	0.11
STRI	-142.9531	63.3334	-0.06	-0.29
TAHN	-147.1016	61.9720	-0.56	0.91
TALK	-150.1057	62.2986	0.07	-0.64
TAZL	-145.4329	62.0799	-0.50	0.75
THMP	-145.7323	61.1280	-1.32	2.45
TINA	-142.0263	63.1127	0.16	-0.20
TLKA	-150.4203	62.3077	0.11	-0.73
TNAC	-142.0265	63.1126	0.16	-0.20
TP26	-143.0390	63.2547	-0.06	-0.25
TRAI	-143.1999	63.1611	-0.07	-0.19
TSIN	-145.5282	61.2036	-1.29	2.27
TURN	-149.5433	60.9305	-0.60	0.73
TWB1	-143.3161	63.3593	-0.10	-0.26
UAAG	-149.8241	61.1911	-0.32	-0.01
W3	-148.8426	63.6602	-0.15	0.04
WHTU	-142.0669	60.0478	-1.31	2.53

Table 3 continued

WICK	-148.0662	65.1827	0.09	-0.30
WILL	-145.2714	61.8951	-0.57	0.94
WOND	-150.8737	63.4912	0.15	-0.85
Y111	-147.4846	63.0968	-0.64	-0.20
YKTT	-139.6488	59.5107	-2.13	3.86
YUKO	-149.0930	65.6762	0.05	-0.35
Z22A	-150.0524	61.7542	-0.01	-0.71

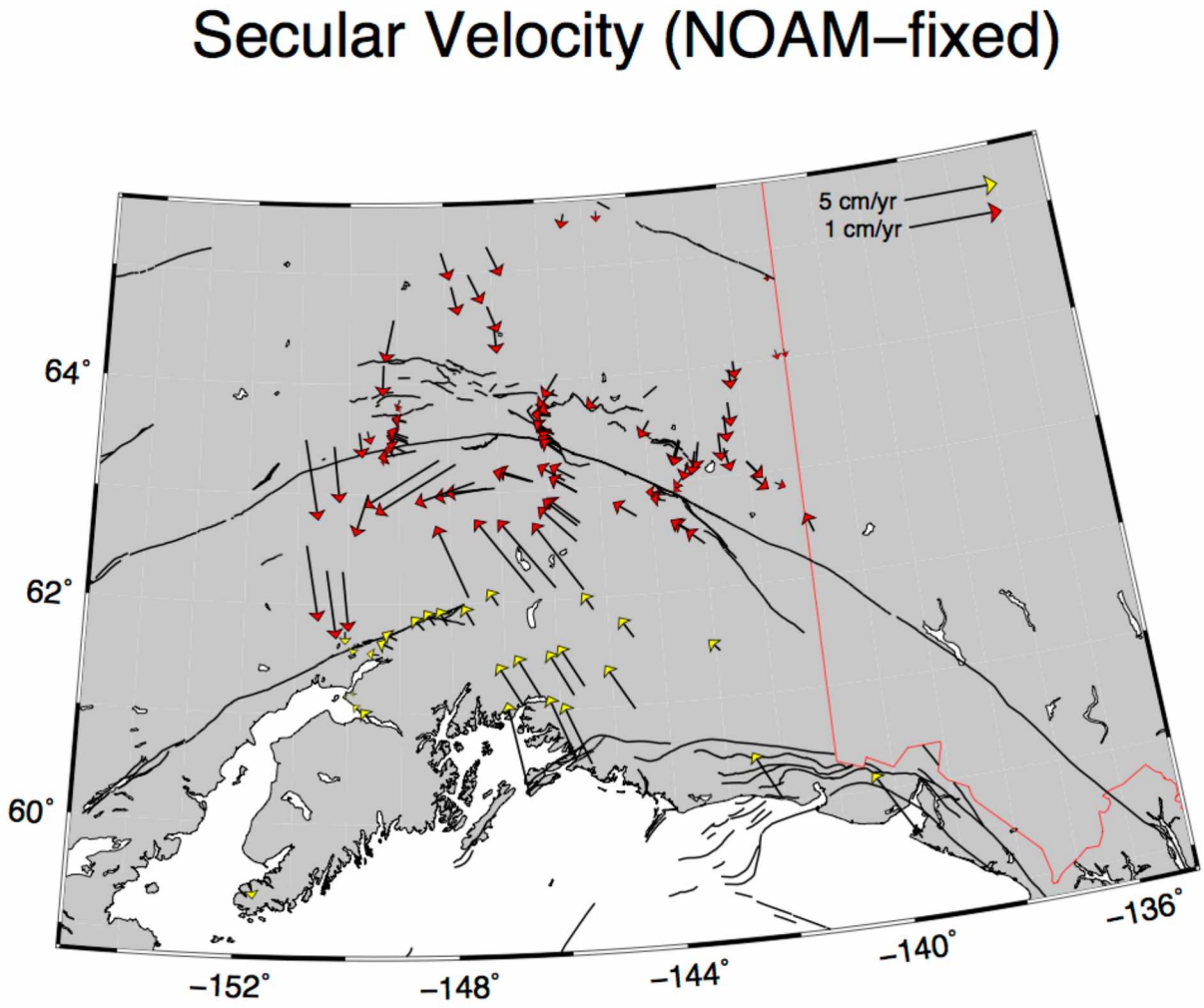

Figure 17. Interpolated velocity field shown in a North American plate-fixed reference frame. Velocities south of 62°N (shown in yellow) are quite large due to subduction zone strain, so the vectors are scaled by a factor of ¼.

In fitting the time series, the exponential decay parameter has a significant tradeoff with the secular velocity, which can bias the estimates of transient displacement. It's necessary then to examine the relationship of a time series parameterization with a "fixed" a priori secular velocity and one with a priori errors, too (See Discussion, Chapter 7). An important assumption made here is that pre-earthquake secular velocities do not change after an earthquake. While this is not an issue that can be solved with time series analysis alone, systematic biases in postseismic model misfits might suggest at least a temporary change in secular velocity which could be caused by increased coupling between the subducting slab and overriding plate in the south [*Johnson et al.*, 2009].

Not all GPS sites in the postseismic dataset have good coverage throughout the post-earthquake time series—for example, some continuous sites were not installed until several years after the event, some campaign sites have been abandoned, and some have a significant data gap. The post-earthquake time series is split into three-year intervals, and the displacements over each interval are kept or rejected on a site-by-site basis depending on how well constrained the time series fit is. For instance, if no data are recorded at a campaign site before 2007, then estimated displacement at that site over the 2003-2006 and 2006-2009 intervals would not be reliable since the time series is unconstrained before 2007 (see Figure 18).

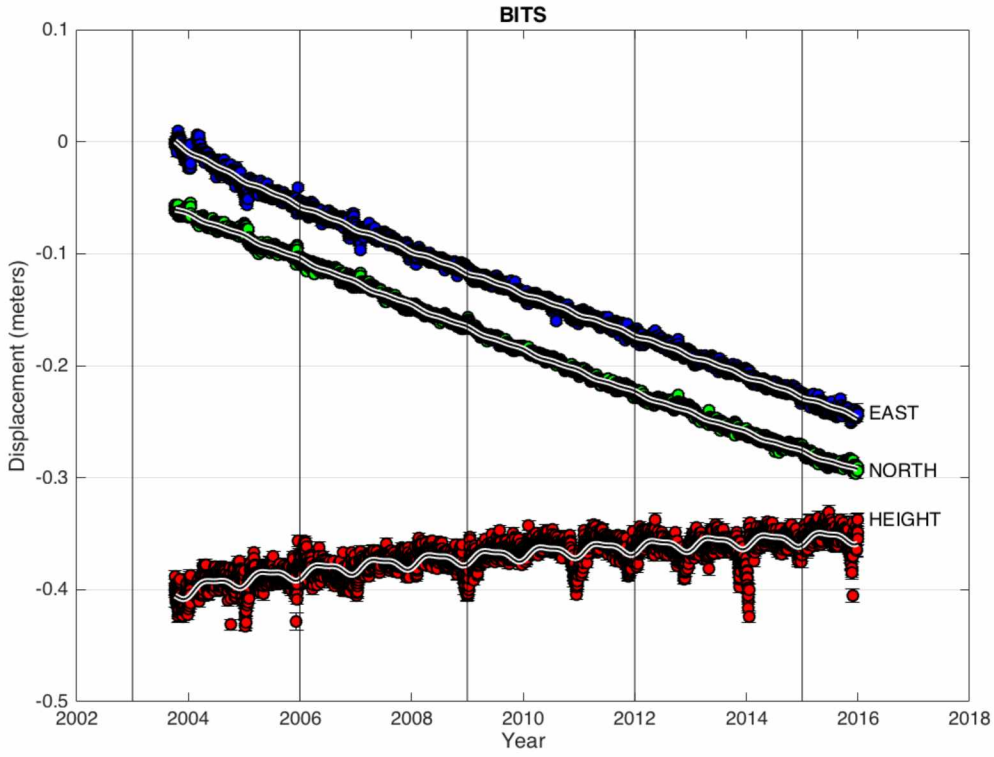

Figure 18. Three different cases of postseismic time series. (Top) A continuous site not installed until late 2003—coverage is great, but a secular velocity has to be interpolated from nearby sites. (Middle) Campaign GPS with good coverage—although secular velocity must be interpolated in this case, the yearly sampling at this site leaves no gaps in the postseismic time series. (Bottom) Campaign GPS with poor coverage—low sampling rates after the earthquake leave only one window where the time series is well constrained and can be used in model evaluation. Vertical black lines denote beginnings and ends of sampling intervals.

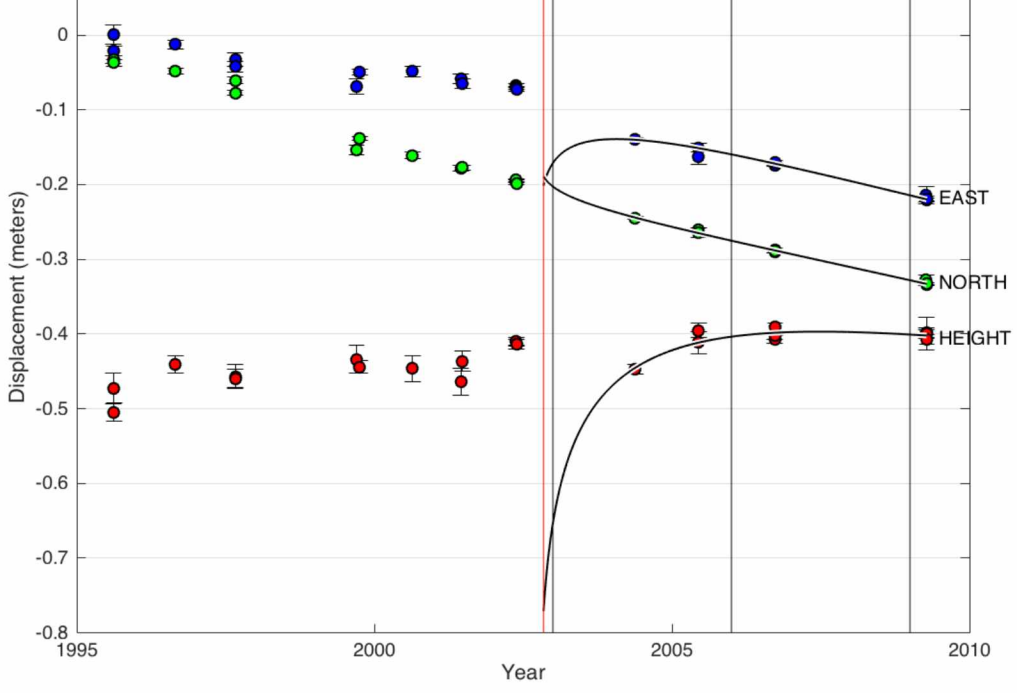

Figure 18 cont.

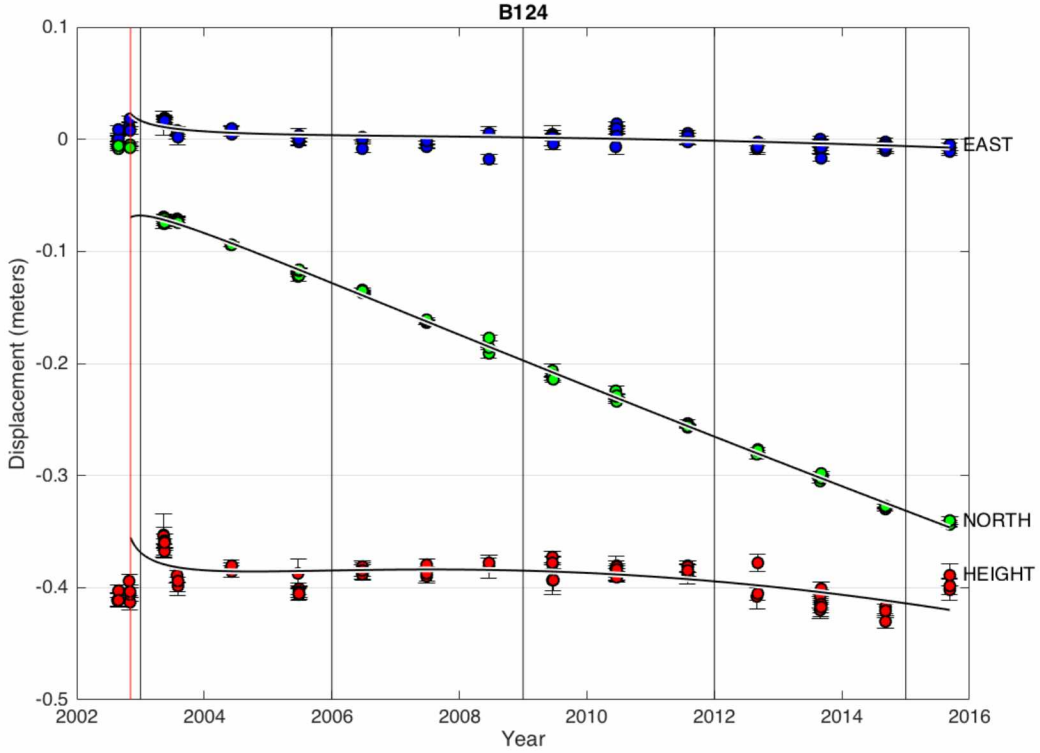
B124
0.1
0
-0.1
-0.2
-0.3
-0.4
-0.5
Displacement (meters)
2002
2004
2006
2008
2010
2012
2014
2016
Year
EAST
NORTH
HEIGHT
S103

5.2 Optimizing Decay Time Constants

Decay time constants, τ_L and τ_E, are assumed to be the same in all components (east, north, up) and for all GPS sites. The constants are optimized by a grid search to minimize total WRSS for a suite of 14 continuous GPS sites with good spatial coverage at the rupture's western tip and the central transect (Figure 19). The decay functions and time constants are not assumed to correspond to any one postseismic deformation mechanism, only the superposition of multiple mechanisms. Parametrically fitting the GPS time series is not assigned any long-term predictive power; however, over short periods of time, there may be some capacity for prediction [*Tobita*, 2016]—which poses the question: how long is "long enough" to parametrically describe a postseismic displacement timeseries? (See Discussion, Chapter 7).

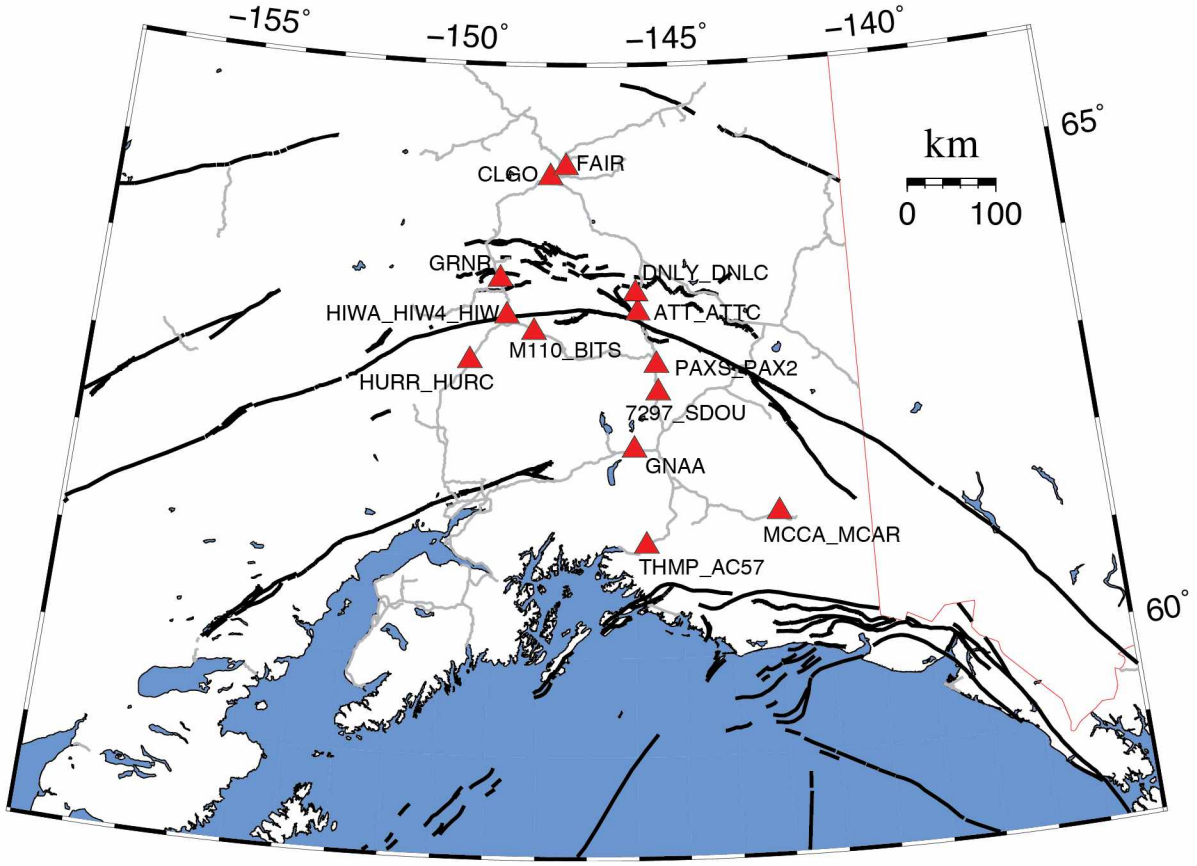

Figure 19. Spatial distribution of the tied and continuous GPS sites used to optimize the decay constants in the time series fits.

By windowing the postseismic time series to exclude more recent data and re-optimizing time constants, it is evident that the more post-earthquake data used, the larger the preferred time constants for the exponential relaxation. There is not currently enough data to

definitively state if this trend ceases. Using all available data, optimal time constants are: τ_L = 0.12 years and τ_E = 20 years (Figure 20). It is worth noting that *Suito and Freymueller* [2009] estimated the Maxwell relaxation time for the mantle to be 20 years, potentially suggesting τ_E = 20 years should be the maximum decay time in the parameterization, as the mantle relaxation time should be the longest of the active processes.

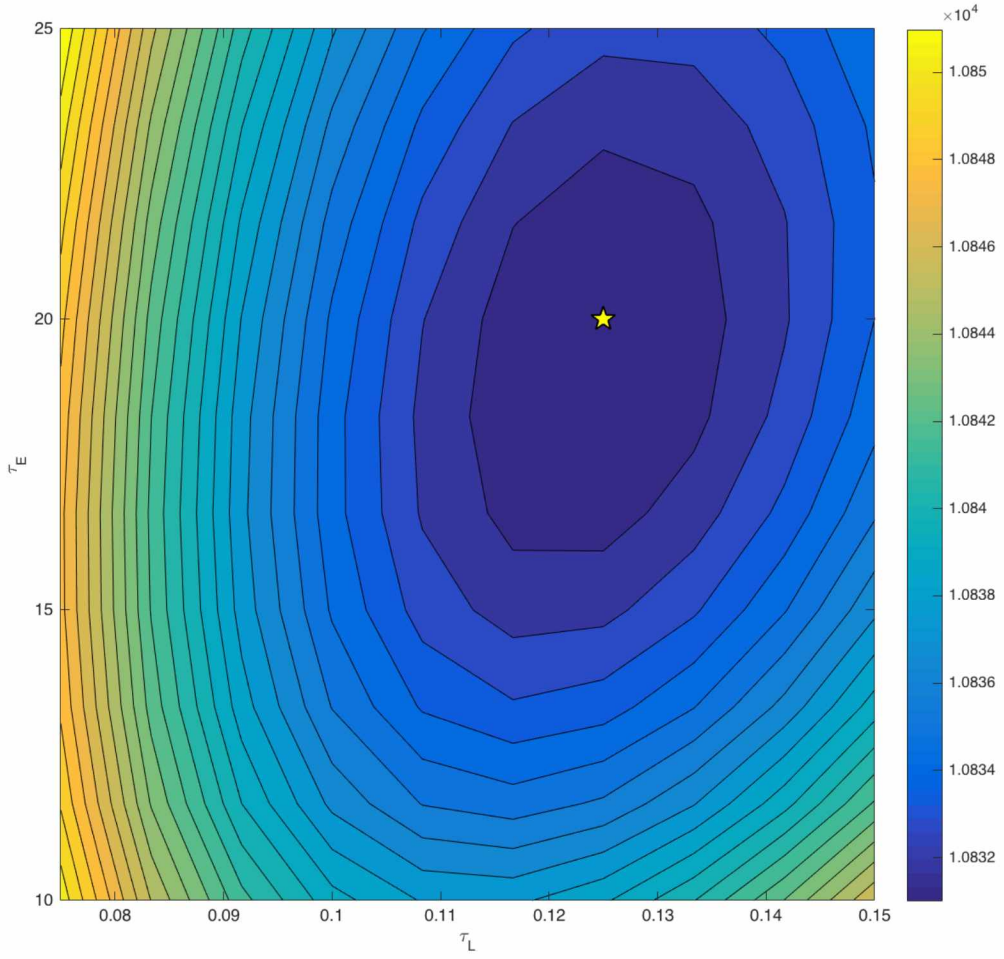

Figure 20. Total WRSS for fitted continuous sites based on logarithmic and exponential decay time constants. Best fitting model is τ_L = 0.125 years, τ_E = 20 years.

With optimal time constraints and estimated secular velocities, all postseismic time series are fit, and transient displacements are extracted at common epochs. Figure 21 shows (and Table 4 lists) the horizontal postseismic displacements over four intervals of three years.

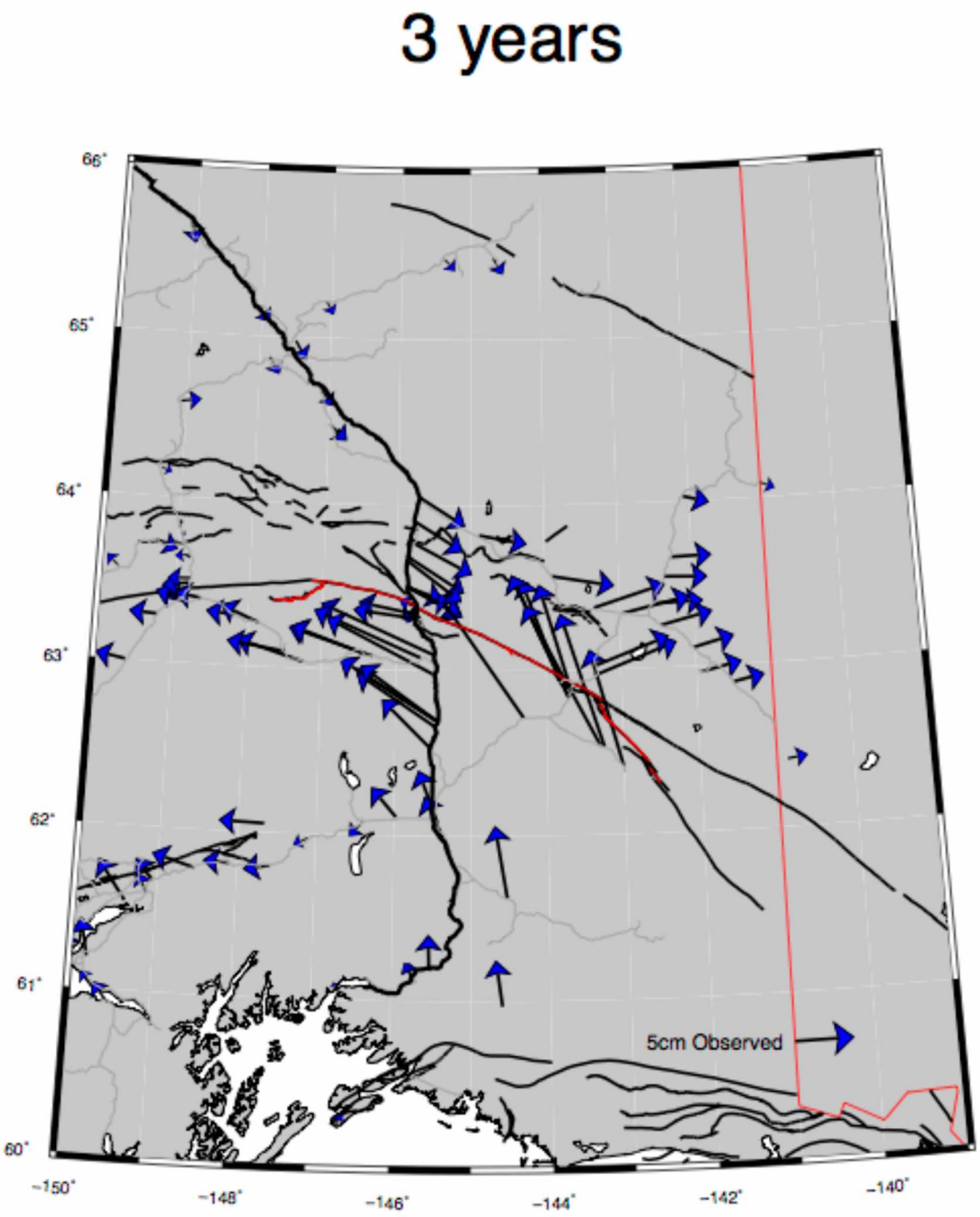

Figure 21. Observed postseismic displacements over three year intervals. “3 years” denotes the displacement from 2003 (just after the earthquake) to 2006, and so on. It’s apparent that displacements are generally greater south of the fault.

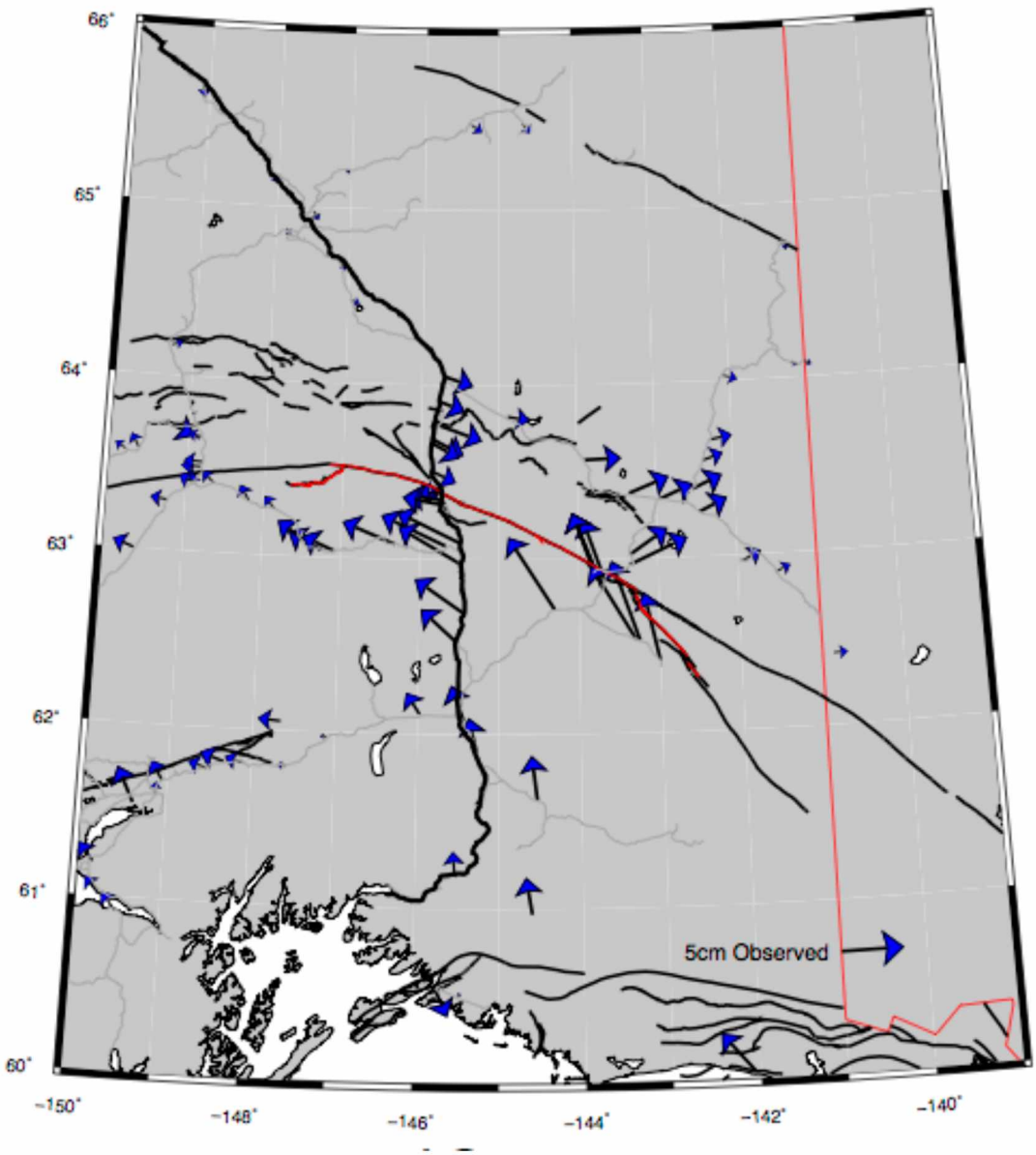

Figure 21 cont.

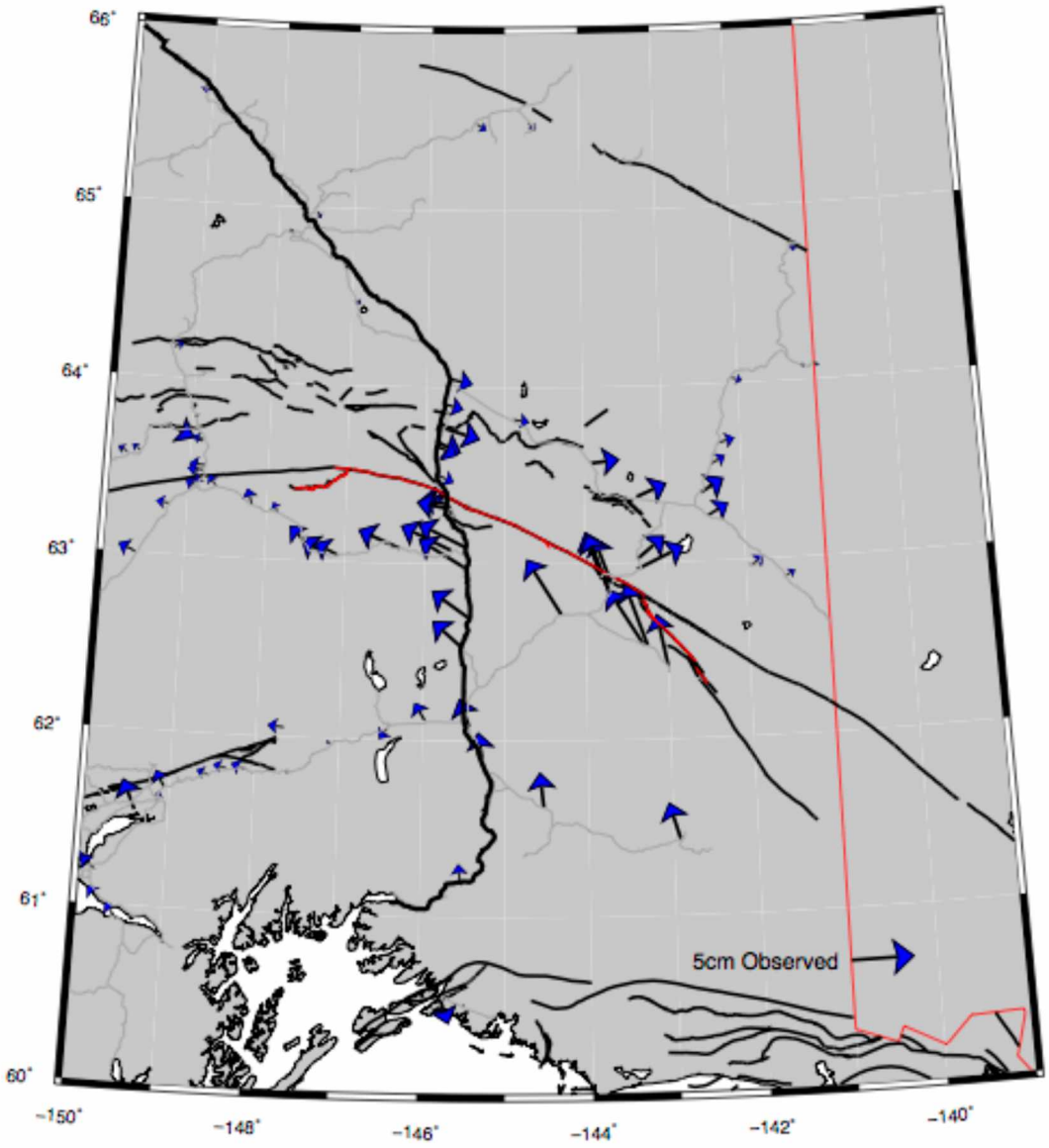

Figure 21 cont.

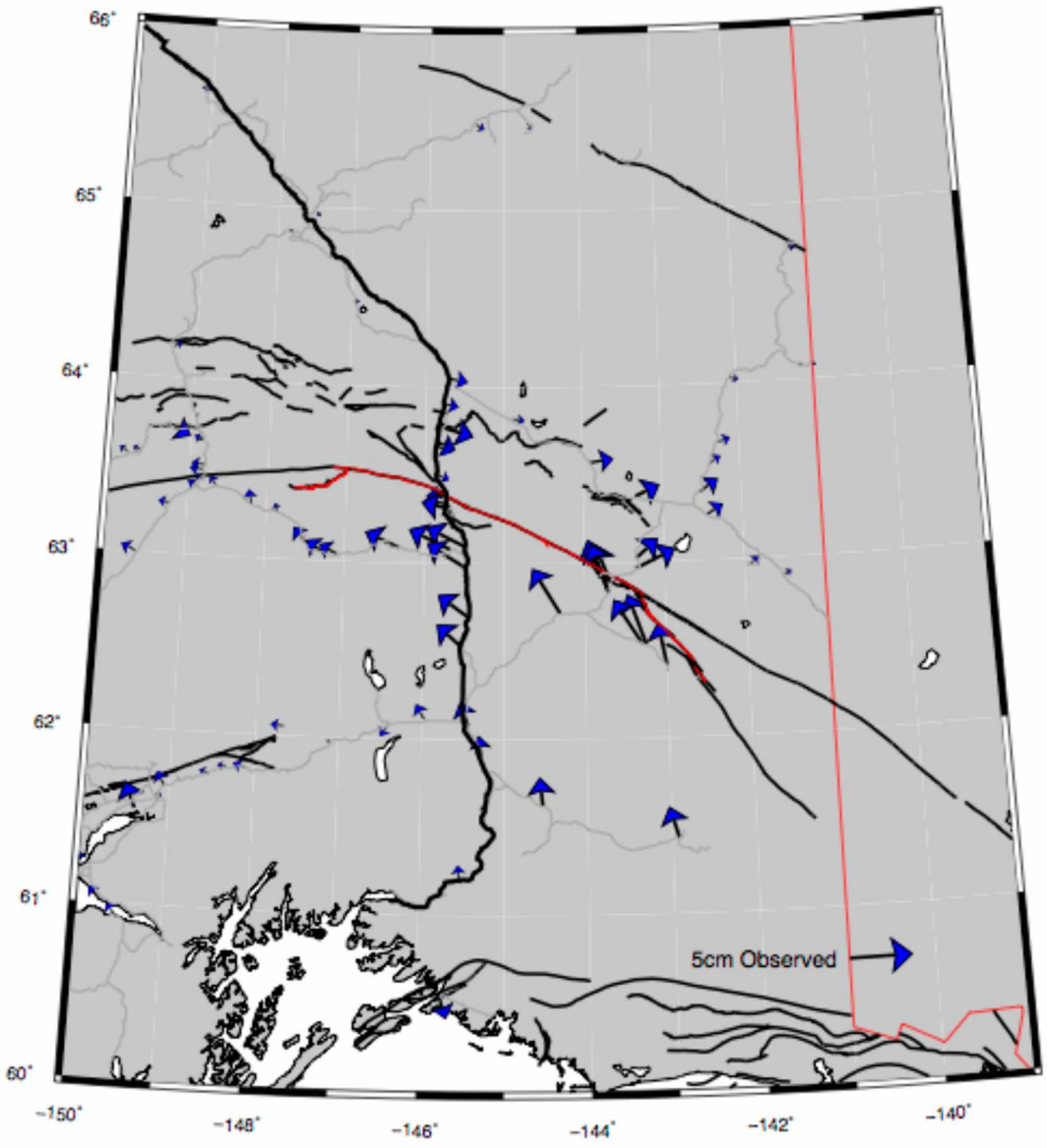

Figure 21 cont

Table 4. Observed postseismic displacements

			2003-2006		2006-2009		2009-2012		2012-2015	
Site	Lon.	Lat.	E (mm)	N (mm)	E (mm)	N (mm)	E (mm)	N (mm)	E (mm)	N (mm)
0999	-142.2748	63.6650	3.4	0.1	1.7	0.3	1.3	0.3	1.0	0.3
126G	-141.0013	64.0865	1.2	-0.5	0.5	-0.3	0.4	-0.2	0.3	-0.2
152T	-150.6735	66.8208	-	-	-0.4	-2.3	-0.6	-2.1	-0.6	-1.9
299C	-142.0758	64.0289	2.2	-0.6	1.1	-0.4	0.8	-0.3	0.7	-0.2
AB41	-146.3596	61.1272	-	-	0.5	-0.5	-0.4	0.7	-0.6	1.0
AC11	-145.4262	62.6880	-	-	-4.0	3.0	-3.0	2.4	-2.5	2.0
ANC1	-141.1581	64.7773	1.0	0.0	0.0	-0.7	-0.2	-0.7	-0.2	-0.7
ATT	-148.3317	61.8071	-6.1	2.8	-	-	-	-	-	-
ATTC	-149.9968	61.1824	-1.0	1.9	-0.7	2.0	-0.5	1.8	-0.4	1.5
ATW2	-145.8472	63.5025	2.9	-1.1	-0.2	0.6	-0.6	0.8	-0.7	0.8
B124	-145.8472	63.5024	4.4	-2.2	1.9	-0.9	1.3	-0.6	1.0	-0.4
BEA2	-145.8473	63.5024	4.6	-2.5	1.8	-1.1	-	-	-	-
BITS	-149.1323	61.5978	-0.7	1.6	0.0	1.0	0.1	0.8	0.1	0.7
BREM	-149.3088	63.7349	1.9	-0.7	2.4	-1.1	-	-	-	-
BRWN	-140.8625	62.4078	1.7	0.2	1.1	0.1	0.9	0.0	0.8	0.0
BSB4	-148.1883	63.3047	-2.4	0.3	-0.7	1.3	-0.4	1.3	-0.2	1.1
BUZZ	-148.1883	63.3047	-0.7	2.7	0.9	3.0	1.1	2.7	1.0	2.4
C125	-144.6056	60.9682	-	-	-0.5	3.0	-0.4	2.5	-0.4	2.1
CENA	-149.2951	64.1707	0.9	-0.3	0.9	0.3	0.8	0.4	0.7	0.3
CHI3	-145.7891	63.9065	4.2	-2.6	-	-	-	-	-	-
CKLN	-143.3521	62.9638	6.9	2.6	4.6	2.1	3.7	1.7	3.1	1.5
CLGO	-149.6304	63.5737	0.0	4.6	-0.6	1.1	-0.7	0.4	-0.6	0.2
CODO	-144.6776	65.4982	-	-	0.6	-0.8	0.5	-0.6	0.4	-0.5
DFLY	-146.6466	60.2375	0.5	1.0	-0.1	0.5	-0.2	0.4	-0.2	0.3
DH32	-148.5368	61.7647	-3.6	1.1	-1.5	0.5	-1.0	0.3	-0.8	0.3
DH34	-147.8605	64.8738	0.9	-1.4	-	-	-	-	-	-
DH97	-145.4754	60.4937	1.1	1.3	0.1	0.4	-0.1	0.2	-0.1	0.1
DLTJ	-142.1757	63.9552	0.7	-1.0	-2.4	-0.6	-2.6	-0.5	-2.4	-0.4
DMC3	-148.9198	63.7936	-0.2	-0.5	-0.3	-0.2	-0.3	-0.2	-0.3	-0.1
DNL3	-146.3127	63.0836	-7.1	2.4	-4.2	1.7	-3.3	1.4	-2.7	1.2
DNLC	-146.3658	63.0862	-6.5	2.4	-2.9	1.4	-2.0	1.0	-1.6	0.8
DRMC	-147.8550	63.2652	-3.2	1.4	-0.8	1.0	-0.4	0.8	-0.2	0.7
E175	-145.7136	64.0493	3.9	-2.5	2.3	-0.8	1.8	-0.5	1.5	-0.3
EFRK	-144.8897	63.8192	4.0	-0.8	1.8	-0.3	1.3	-0.2	1.0	-0.2
EGL2	-143.3405	63.3723	6.0	1.8	3.2	1.3	2.4	1.0	1.9	0.9
EIL1	-145.8877	63.6951	4.9	-3.2	2.7	-1.4	2.0	-1.0	-	-
EYAC	-145.8877	63.6951	-	-	2.6	-1.0	2.0	-0.6	1.6	-0.5

Table 4 cont.

F101	-144.3040	62.7140	-7.1	10.5	-3.6	5.8	-2.7	4.4	-2.2	3.6
FAIR	-142.5298	63.3868	4.1	0.1	2.4	1.1	1.9	1.1	1.5	1.0
FCRK	-141.1601	64.7787	0.3	-0.3	0.8	-0.7	0.8	-0.7	0.7	-0.7
FLY	-149.7940	63.5592	-1.0	1.0	-0.9	0.6	-0.8	0.4	-0.7	0.4
FM02	-145.3875	65.4909	0.9	-1.0	0.9	-0.6	0.8	-0.5	0.7	-0.4
FM04	-147.1130	64.6879	1.0	-1.4	0.4	-0.6	0.2	-0.4	0.2	-0.3
FM10	-135.2222	58.9719	-0.5	0.3	-0.6	-0.1	-0.5	-0.2	-0.5	-0.2
FM11	-145.7499	60.5487	2.4	-1.8	1.0	-2.4	0.7	-2.2	-	-
FM12	-145.8855	63.6704	-	-	2.4	-1.3	1.7	-0.8	1.4	-0.6
FNGR	-147.4992	64.9780	-	-	0.4	-0.8	0.3	-0.5	0.2	-0.4
FRIG	-145.4753	63.0907	-9.6	4.4	-5.1	2.5	-3.9	1.9	-3.1	1.6
GDNR	-143.2483	62.5284	-3.5	11.3	-2.1	6.4	-1.7	4.9	-1.4	4.0
GNAA	-145.7439	63.4060	0.0	-0.9	-0.4	-0.3	-0.4	-0.2	-0.4	-0.1
GRIZ	-145.7395	63.3933	-0.8	-1.5	-0.8	-0.2	-0.7	0.0	-0.6	0.1
GRNR	-145.7350	63.3879	-1.2	-1.1	-0.9	-0.4	-0.7	-0.2	-0.6	-0.2
GRNX	-145.7330	63.3820	-	-	-1.2	-0.1	-1.0	-0.2	-0.8	-0.3
HIWC	-145.7305	63.3819	-1.2	-0.1	-1.9	-0.1	-1.8	0.0	-1.6	0.0
HURC	-150.4924	66.3755	0.7	-0.1	-0.4	-1.9	-0.5	-2.0	-0.5	-1.8
I177	-143.0052	62.4109	-	-	-1.2	5.5	-0.8	4.2	-0.6	3.4
ISLZ	-141.5119	62.8928	2.6	0.5	1.1	0.5	0.8	0.4	0.6	0.4
JANL	-145.9702	62.1124	-2.1	2.5	-1.1	1.7	-0.8	1.4	-0.7	1.2
KNOZ	-148.8330	63.6524	-1.2	-0.1	-1.0	0.3	-0.9	0.3	-0.8	0.3
L2C6	-148.9783	63.8358	-0.1	-0.3	-0.2	0.1	-0.2	0.1	-0.2	0.1
LADU	-148.9782	63.8355	0.2	-0.6	-0.2	-0.2	-0.3	-0.1	-0.3	-0.1
LIBF	-148.8073	63.4644	-2.6	0.8	-1.7	1.1	-1.4	1.0	-1.1	0.9
LOGC	-148.8073	63.4644	-1.8	-1.1	-1.0	-0.8	-0.7	-0.7	-0.6	-0.6
LSG1	-149.6088	62.9993	-2.6	0.5	-1.7	0.7	-1.4	0.6	-1.1	0.5
LUCI	-149.6088	62.9993	-2.6	1.0	-1.7	1.2	-1.4	1.1	-1.1	0.9
M126	-141.1776	64.0861	0.5	-0.8	0.5	-0.3	0.4	-0.2	0.3	-0.2
M175	-149.7456	61.0207	-0.9	1.1	-1.1	1.1	-1.0	1.0	-0.8	0.9
MACL	-143.9057	63.5685	5.3	-0.9	3.0	0.1	2.3	0.2	1.9	0.3
MCAR	-147.2443	63.0393	-	-	-	-	-1.9	1.2	-1.5	1.0
MEN	-148.8662	63.3828	-2.5	0.7	-1.4	0.7	-1.1	0.6	-0.9	0.5
MENT	-142.4529	63.2543	4.4	1.0	2.3	1.1	1.7	1.0	1.4	0.8
MOS2	-144.5359	61.6202	-1.0	6.1	-0.4	3.6	-0.3	2.8	-0.2	2.3
NENA	-143.3454	63.0226	6.3	2.3	-	-	-	-	-	-
O8	-147.6658	62.0533	-3.8	0.2	-1.8	0.2	-1.3	0.1	-1.0	0.1
ORTT	-145.6753	63.0780	-8.9	4.0	-5.1	2.4	-4.0	1.9	-3.2	1.6
P100	-148.1883	63.3047	-0.7	2.7	0.9	3.0	1.1	2.7	1.0	2.4
P592	-150.2970	63.4330	-1.5	1.7	-1.2	1.3	-1.0	1.1	-0.9	0.9

Table 4 cont.

PANA	-142.3790	63.5488	3.7	-0.2	1.6	0.5	1.1	0.6	0.9	0.5
PAX2	-143.6800	62.8881	-2.5	8.8	-1.6	4.8	-1.3	3.6	-1.1	3.0
PISA	-142.9204	61.4320	-1.2	4.5	-1.0	3.4	-0.9	2.9	-0.7	2.5
PIT2	-142.9204	61.4320	-1.7	4.7	-	-	-1.3	3.6	-1.1	3.1
POT3	-143.7953	62.9095	-3.2	8.9	-	-	-	-	-	-
PTVL	-143.7042	62.8315	-4.7	10.4	-2.3	6.0	-1.7	4.7	-1.4	3.8
PURI	-149.0560	61.6756	-1.5	1.7	-1.0	1.6	-0.8	1.4	-0.7	1.2
Q112	-149.0798	64.5794	-	-	1.6	0.8	1.4	0.8	1.3	0.7
R109	-145.5156	62.5229	-4.2	4.2	-2.9	2.7	-2.4	2.2	-2.0	1.8
RBOW	-141.9364	62.9610	3.4	0.8	1.5	0.8	1.0	0.7	0.8	0.6
REED	-145.7697	63.7680	4.9	-2.6	3.4	-1.3	2.8	-0.9	2.4	-0.7
ROLL	-145.7353	63.3397	-4.9	1.0	-2.7	0.5	-2.1	0.3	-1.7	0.3
S103	-148.8204	63.4837	-	-	-1.6	0.1	-	-	-	-
SDOU	-145.4519	62.9673	-9.3	4.9	-5.2	3.1	-3.9	2.4	-3.2	2.0
SELD	-145.4524	62.9692	36.4	2.9	40.9	0.5	36.9	0.0	32.4	-0.1
SG27	-145.4519	62.9673	-9.4	5.1	-5.1	3.1	-3.9	2.5	-3.2	2.1
SHPA	-145.4519	62.9673	-9.3	5.0	-5.1	3.1	-3.9	2.5	-3.2	2.0
SLCH	-149.2105	63.2847	-2.5	0.2	-1.5	0.2	-1.1	0.2	-0.9	0.1
SLIM	-146.3999	62.0789	-1.1	-1.2	-0.9	-1.2	-0.8	-1.1	-0.7	-0.9
SOUR	-146.6968	61.0563	-0.1	0.8	-	-	-	-	-	-
SPIL	-150.8167	62.5317	-2.5	0.9	-2.0	0.8	-1.7	0.7	-1.4	0.6
SSWB	-148.0894	61.8046	-	-	-	-	-	-	-	-
STRI	-147.0855	63.0377	-5.4	1.8	-2.6	1.1	-	-	-1.5	0.8
TAHN	-148.6468	63.3953	-2.2	0.4	-0.9	0.9	-0.6	0.9	-0.5	0.8
TALK	-145.6869	63.3109	-	-	-3.4	0.6	-	-	-	-
TAZL	-149.3959	61.5424	-2.4	3.4	-1.4	2.8	-1.1	2.4	-0.9	2.1
THMP	-143.2969	62.5358	-6.1	12.0	-	-	-	-	-	-
TINA	-149.8706	61.6443	0.5	1.4	-	-	-	-	-	-
TLKA	-145.4263	62.6880	-7.0	4.5	-4.0	2.8	-3.1	2.2	-2.5	1.8
TSIN	-151.7067	59.4457	0.3	-0.4	0.1	0.1	0.1	0.2	0.1	0.2
TURN	-156.6103	71.3229	-1.9	-6.7	-1.8	-6.3	-1.5	-5.5	-1.3	-4.8
UAAG	-147.5756	61.7998	-2.2	-0.4	-0.7	0.0	-0.4	0.1	-	-
W3	-146.9764	64.4767	1.5	-1.3	0.8	-0.3	0.6	-0.1	0.5	-0.1
WHTU	-148.8041	63.5120	-	-	-1.5	0.1	-	-	-	-
WICK	-145.4837	62.6639	-6.5	4.5	-3.6	3.1	-2.8	2.6	-2.3	2.2
WILL	-145.4262	62.6880	-8.3	5.3	-5.2	3.5	-4.1	2.9	-3.4	2.4
WOND	-145.4262	62.6880	-6.6	4.8	-3.5	3.0	-2.7	2.4	-2.2	2.0
Y111	-147.0844	65.2268	0.7	-1.2	0.3	-0.4	0.2	-0.2	0.1	-0.2
YKTT	-149.0902	63.3413	-2.5	-0.4	-1.5	-0.1	-1.2	0.0	-1.0	0.0
YUKO	-142.9531	63.3334	5.7	1.3	2.7	1.1	1.9	1.0	1.5	0.9

Table 4 cont.

Z22A	-147.1016	61.9720	-1.2	-0.6	-	-	-	-	-	-

Chapter 6 Finite Element Method Postseismic Modeling

The preferred coseismic slip model is used as the input for the postseismic forward model where deformation occurs in response to the redistributed stresses of the rupture. Stress-driven afterslip and viscoelastic relaxation of the upper mantle and lower crust are used to model postseismic deformation. These finite element models were run by collaborator Yan Hu of the University of Science and Technology of China (Hefei).

6.1 FEM Viscoelastic Structure

The postseismic model uses the same spherical Earth and elastic structure as the coseismic model. The upper mantle and lower crust are modeled as Burgers body viscoelastic materials, with the transient (Kelvin) viscosity component an order of magnitude less than the Maxwell component (Figure 22). The viscoelastic lower crust begins at 20 km depth. The tomography study in *Veenstra et al.* [2006] suggests that the crust-mantle boundary is ten kilometers deeper south of the fault, so the viscoelastic thickness of the lower crust differs across the fault. Beneath the lower crust and extending to 50 km depth is a purely elastic layer, consistent with the "jelly sandwich" model of the lithosphere [*Bürgmann and Dresen*, 2008]. Finally, there is the viscoelastic upper mantle, extending to 120 km depth.

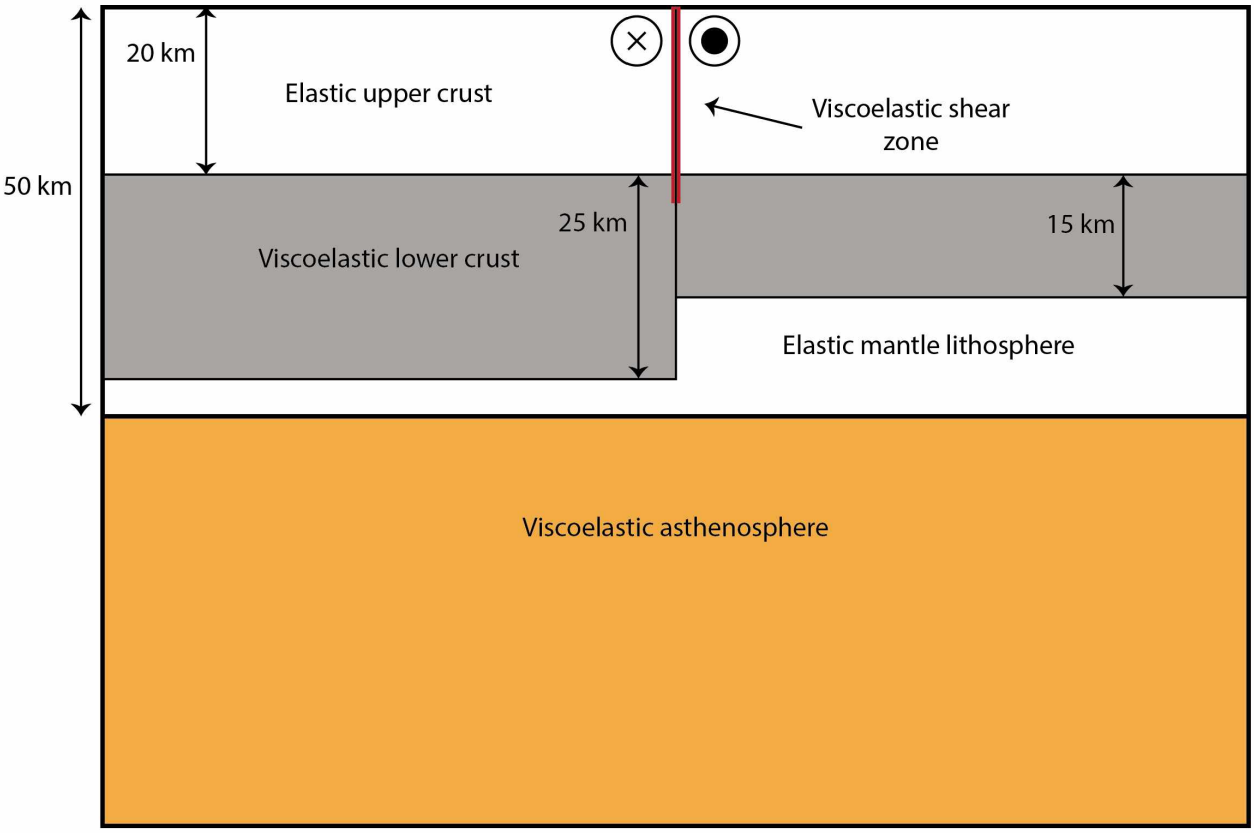

Figure 22. Rheological structure of postseismic finite element model. The thicker crust south of the Denali fault is based on *Veenstra et al.* [2006]. All viscoelastic bodies are given a Burgers body rheology, with the Kelvin viscosity an order of magnitude less than the Maxwell viscosity. Afterslip is approximated as stress-driven slip on a thin viscoelastic shear zone.

Stress-driven afterslip occurs on a thin, viscous shear zone along the fault interface and is restricted to regions of the interface where coseismic slip did not exceed a specified threshold; 2 m slip and 5 m slip thresholds are considered, but these values are somewhat arbitrary (see Discussion Chapter 7.4). Model computations employ the finite element method implemented in the private software PCvise2 [*Hu*, 2011].

6.2 Workflow and Parameter Variance

Initial parameter values are based on a recent study by collaborator Yan Hu. Computed postseismic displacements over three year intervals are compared to the estimated displacements described in Section 5.1, and averaged model misfit is computed. Varying a single parameter at a time, multiple forward models are run to minimize averaged model misfit and find a best fitting model for deformation. At the time of this writing, only one such model

has been run as bugs in the finite element modeling code—specifically implementing the 1D elastic structure—are being worked out. The displacement predictions of the current model, along with the observed displacements, are shown in Figure 23.

South of the fault, for all time intervals, the model under-predicts displacements. The exception to this is the very near-fault sites, where the model over-predicts. Along the central transect, both north and south of the fault, there is a systematic angular difference in displacements generated by the model and the observations. The only regions where this model agrees with observations are just northeast of the fault and west of the rupture tip, but the model displacements decay too quickly and do not fit well from 2009 on. These evident biases give good insight on where to begin adjusting model parameters (see Discussion, Chapter 7.4).

3 years

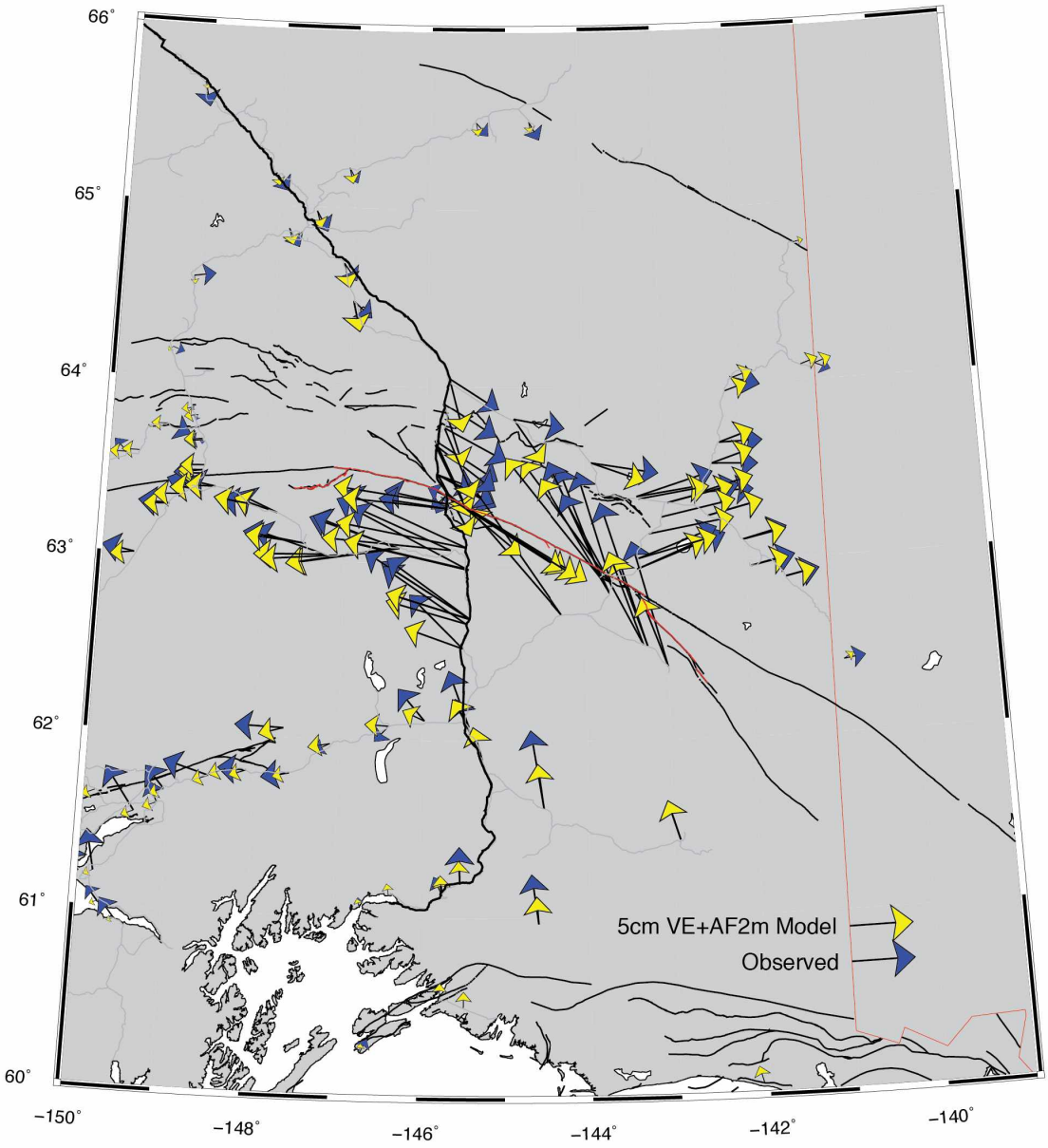

Figure 23. Modeled and observed postseismic displacements. This postseismic model includes both viscoelastic relaxation and 2-meter contoured afterslip. Notice the systematic angular difference between model displacements and data along the central transect of the fault, especially in the first 6 years.

6 years

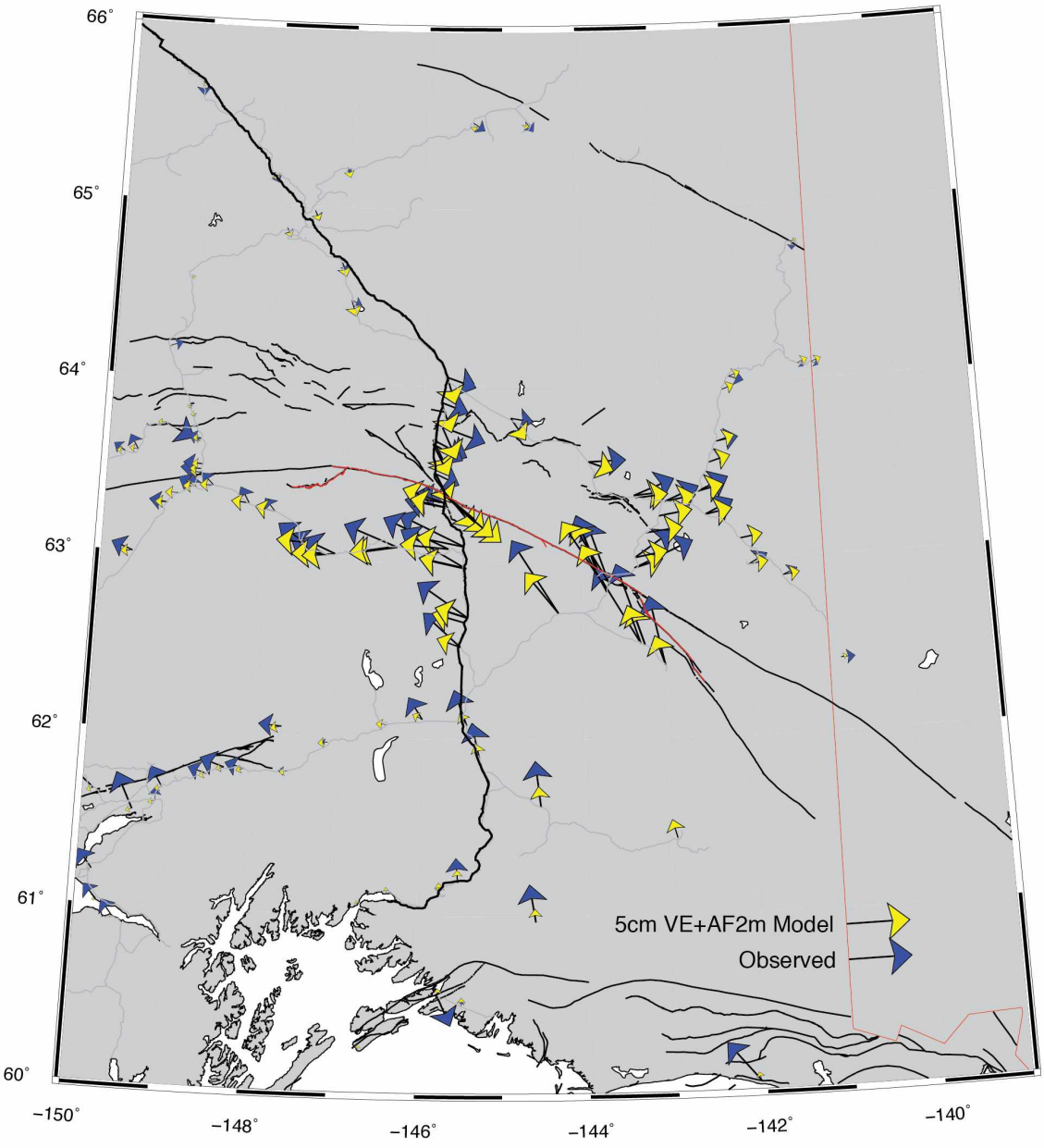

Figure 23 cont.

9 years

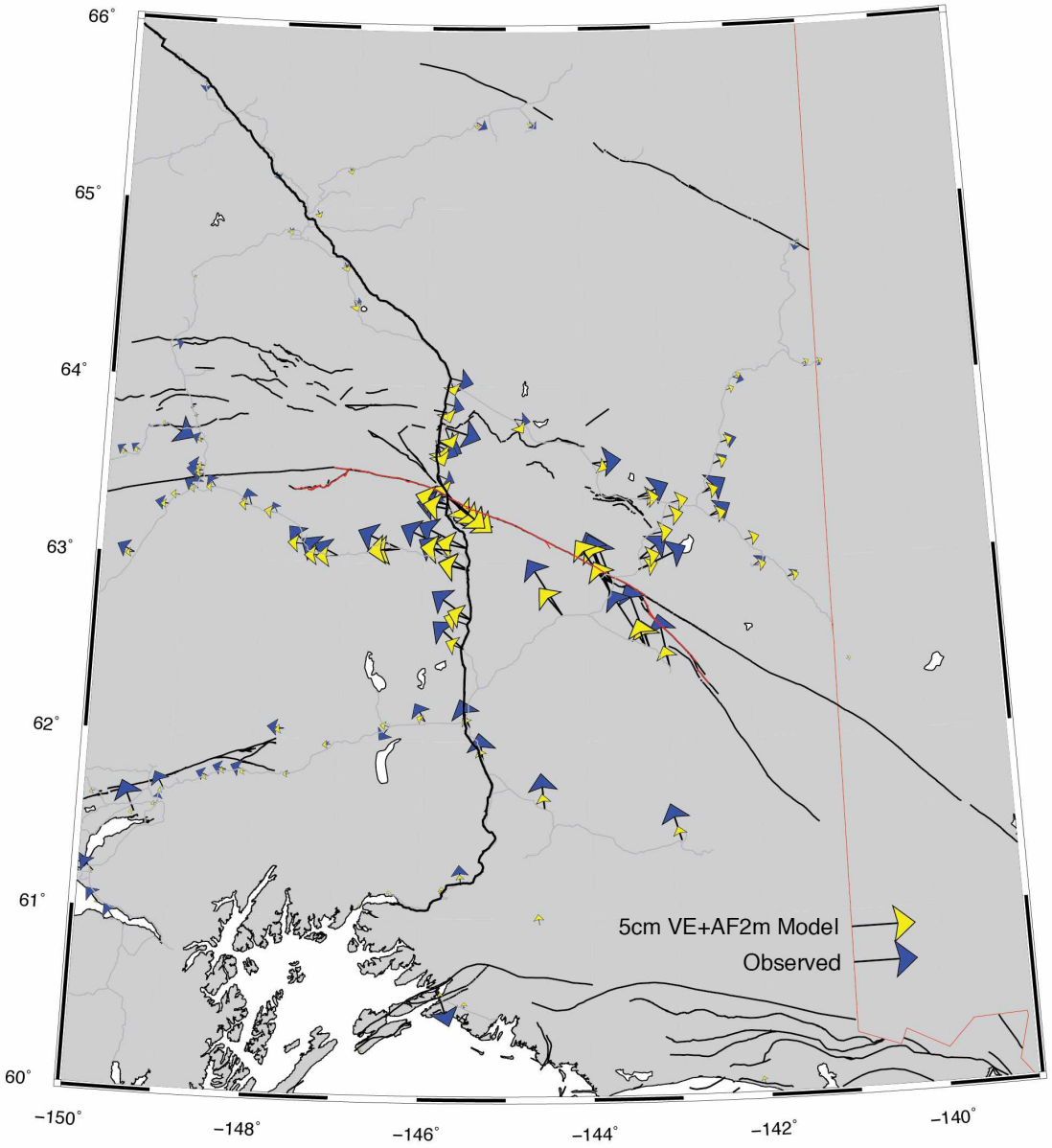

Figure 23 cont.

12 years

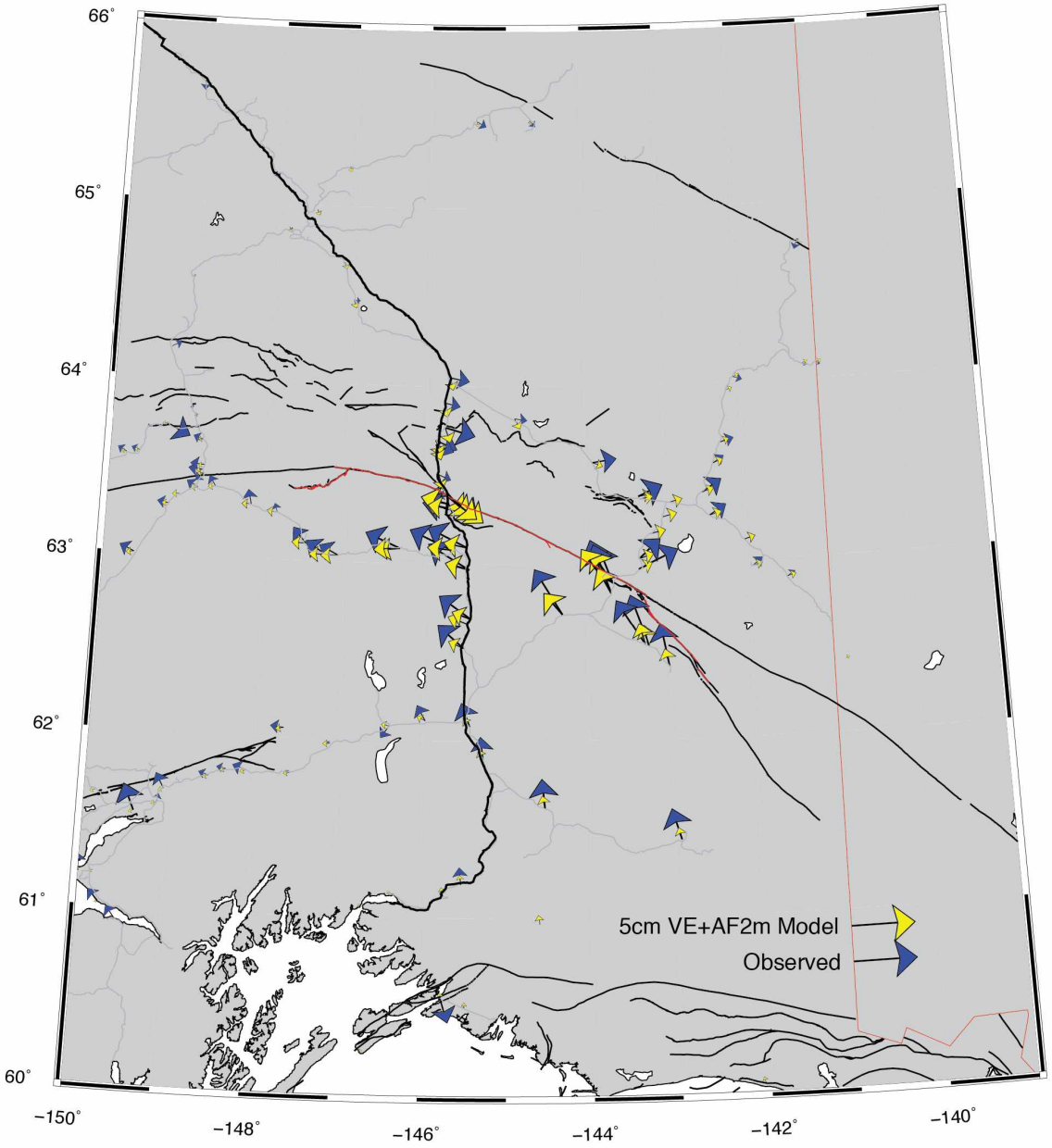

Figure 23 cont.

Chapter 7 Discussion

7.1 Improvements on Previous Coseismic Models

Past coseismic models [*Elliott et al.*, 2007; *Hreinsdóttir et al.*, 2006] were revisited due to improvements in the GPS data set and the need to make the coseismic and postseismic models fully consistent. Better GPS displacement estimates are available due to improved processing—such as an updated ITRF and higher accuracy in reference frames—and post-processing—using seasonal position corrections from GRACE data and estimating GPS displacements in a more systematic, reproducible way. The updated horizontal displacement estimates are not significantly different from previous estimates, but the uncertainties are reduced by about a factor of 2. Vertical displacements are most affected due to the importance of GRACE-derived seasonal corrections in the vertical component.

Because the coseismic slip model for an earthquake will drive the forward postseismic model with coseismic stress changes, it is necessary that the elastic structure of the two models be consistent. *Hearn and Bürgmann* [2005] showed that homogeneous half space models (Okada models), when compared to layered elastic models, typically under-predict slip and moment, and thus coseismic stress change, in the lower crust. In the past, an Okada model was used to model coseismic slip, while an elastically heterogeneous structure was used to model postseismic deformation. When the estimated coseismic slip model was input into the postseismic model, surface displacements were systematically under-predicted [*Freed et al.*, 2006]. To correct for this, slip was extrapolated to greater depth, resulting in a greater overall geodetic moment magnitude, and tapered to zero at 24 km. Use of consistent elastic models eliminates the need for ad hoc corrections in coseismic and postseismic studies.

Figure 24 shows the average slip as a function of depth along the Denali fault for the 1D elastic model and an Okada model. It is clear that deep slip (10-18 km) is much greater in the 1D model, which was expected. To see how these slip differences change at particularly large slip patches (such as the Richardson Highway), Figure 25 shows the slip distribution difference for 1D –Okada. The dominant signal here does not correspond to a particular slip patch but rather greater, broadly distributed difference in slip along the Denali fault. The 1D model

predicts lower slip at shallow depth but higher slip at greater depth. An exception here is on the Susitna Glacier fault where the Okada model predicts very little slip.

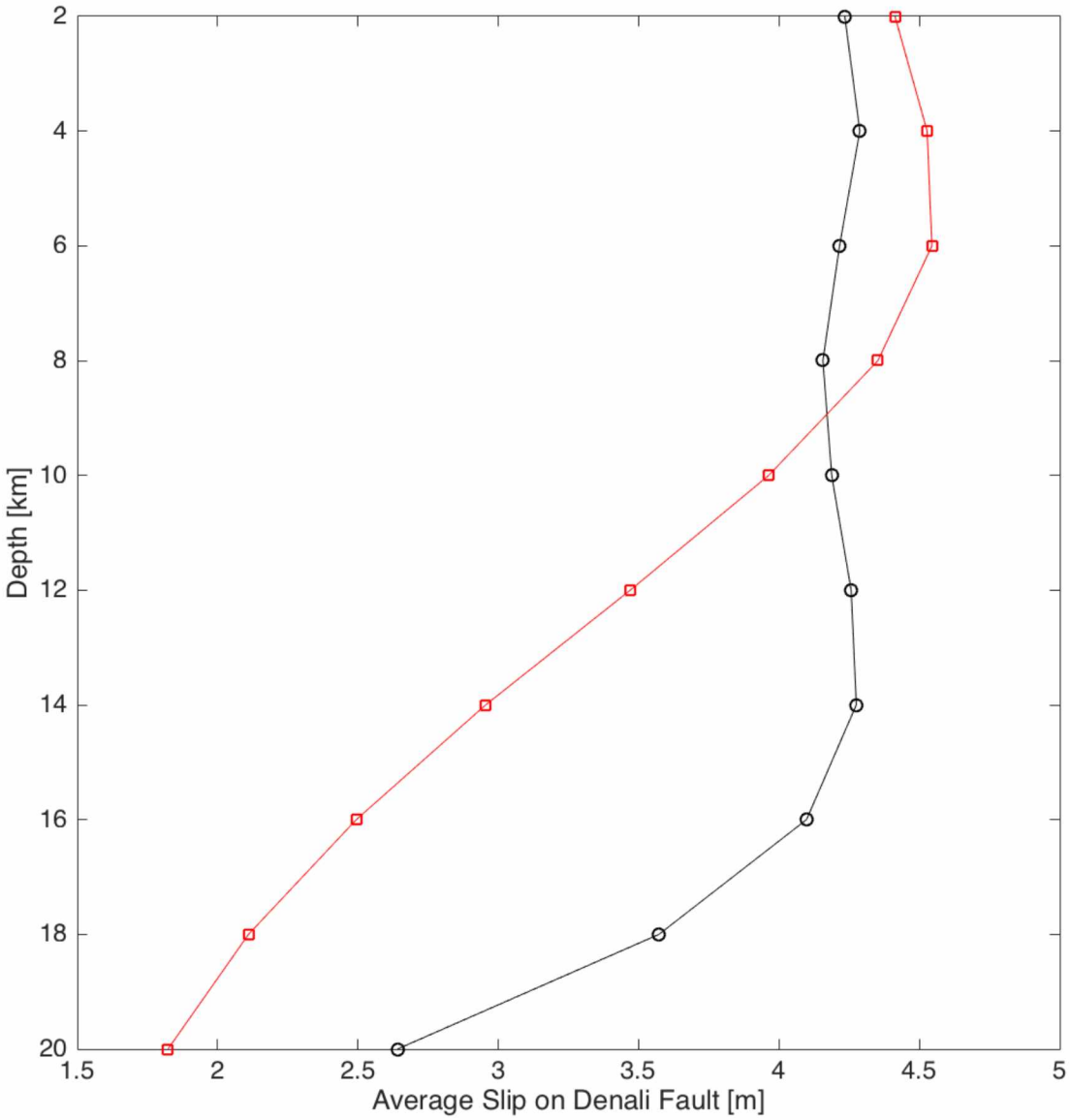

Figure 24. Average coseismic slip along the Denali fault segment as a function of depth. Where slip begins to decrease below 8 km in the Okada model (red squares), the 1D elastic model (black circles) has the greatest average slip below 10 km, as expected.

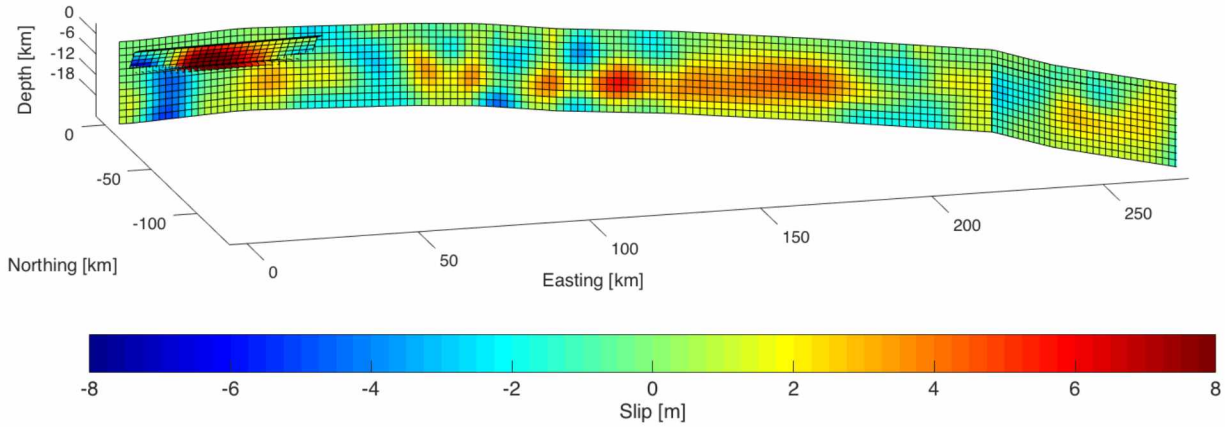

Figure 25. Difference between 1D elastic and Okada coseismic slip distributions. Along the Denali fault, the major differences do not correspond to any slip patch, but rather just a broad zone of greater slip at 12-18 km depth with generally lower slip above that. Nearly the entire Susitna Glacier fault slips more in the 1D elastic model.

While this study does not attempt to model a complete earthquake cycle, the implications of a unified coseismic and postseismic model suggest such a possibility. For instance, in the interseismic phase, locking depth of a fault is one of the significant factors in determining the deformation field. The coseismic slip model—most importantly the depth of coseismic slip—typically corresponds to the "locked" depth of the fault. Average coseismic slip estimates as a function of depth then give a good estimate of a fault's locking depth. Here, the Okada model corresponds to about a 10 km locking depth whereas the 1D model corresponds to about a 16 km locking depth. The geodetic moment of the two models is similar, with M_o = 7.45e20 N-m (7.91 Mw) for the Okada model and M_o = 8.92e20 N-m (7.97 Mw) for the 1D model. The estimated seismic moment for the earthquake is Mw 7.9. The geodetic moment is likely a slight overestimate due to the inclusion of some postseismic motion in the coseismic displacement calculation, as some measurements were made as late as three weeks after the earthquake with no postseismic correction applied.

7.2 Prediction Power of Time Series Fitting

As stated earlier, the time series parameterization is primarily a tool for resampling, not one of prediction. If there were predictive power ascribed to the parameterization, then the question of "how much postseismic data is enough to characterize the processes?" could be

answered. Considering the primary shortcomings of previous postseismic models—likely just lack of data, as the mechanisms considered were sufficient—this knowledge would greatly benefit future postseismic studies.

Tobita [2016] attempts to answer a similar question, albeit over a short period of time and with different intentions: to predict a short-term transient signal and remove it from time series. To answer the question at hand, the same time series used in estimating decay constants are windowed, using only data before a specified date. The best-fitting decay constants are then found via grid search for each windowed data set, and the parameterized time series is projected to present day. For each of the windowed time series predictions, WRSS is computed for the prediction window, 2012-Present (Figure 26).

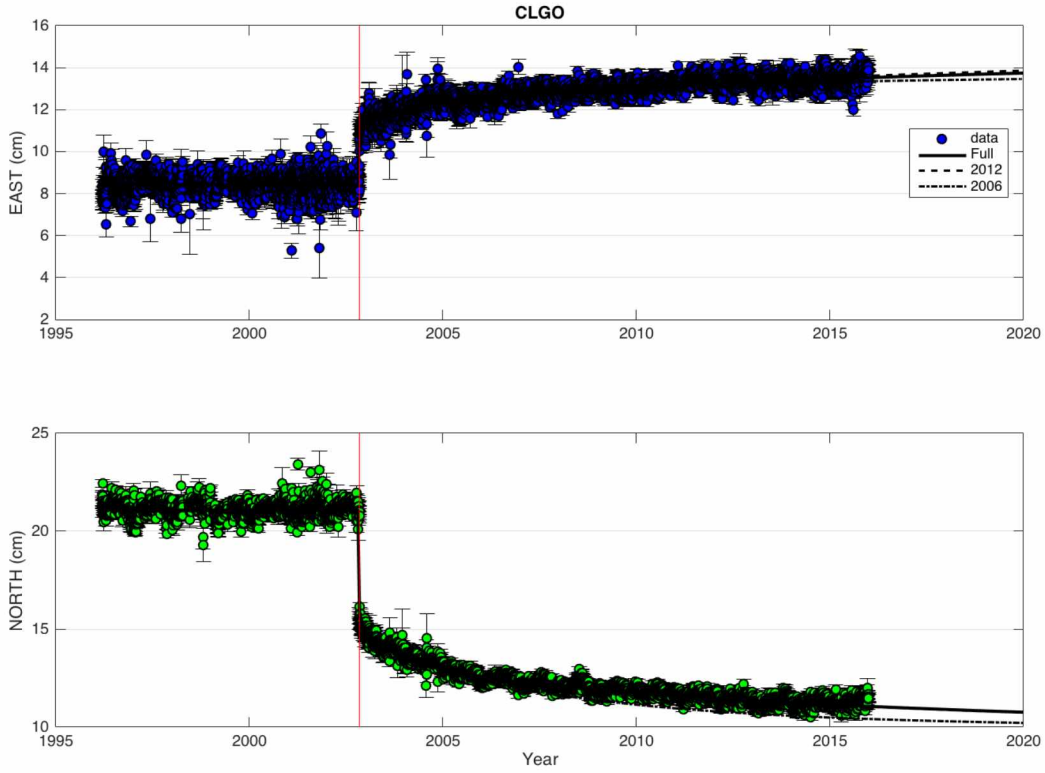

Figure 26: Example of continuous time series with three separate curve fits for different data windows.

As time series windows are varied, the estimated optimal decay constants increase or decrease with the amount of postseismic data—not a particularly interesting conclusion. But

when assessing WRSS, when and if it approaches a steady value, that window time can potentially be considered the minimum amount of time required to allow the "curve fitting" models to predict well into the future. Comparing the prediction window WRSS of the windowed models to the full time series model, I find the 2012-windowed model has an average WRSS twice as large as the full time series, and the 2006 model is about an order of magnitude greater.

Of the 14 GPS time series used in optimizing the decay constants, 4 record slow-slip events in the pre-earthquake time series. This signal is easily removed with the proper hyperbolic tangent function, but again, there is a tradeoff with the secular velocity. If I exclude these sites and re-estimate the best decay constants, the 2012 model does not change, but curiously the 2006 model prefers a long exponential decay time (>25 years). However, neither this change nor simply excluding the 4 sites in the initial misfit calculation appreciably change the total WRSS for the windowed models compared to the full model. Lastly, I use fixed decay constants determined from all available data and fit the windowed data to test whether an a priori decay constant might improve the prediction power of the time series fit. For both the 2006 and 2012 windowed models, misfit in the prediction period, 2012-present, does not change appreciably when using the full time series model decay constants.

In addition to this being an inconclusive result, it is not even completely certain whether all available data is enough to characterize the postseismic cycle—only future observations will tell. It could be that the addition of another decay parameter improves the prediction power; such is the conclusion of *Tobita* [2016]. Regardless, to establish this as a technique, it would need to be repeated for several different earthquakes to see how the minimum time scales with earthquake magnitude, crustal thickness, and tectonic setting, among other factors.

7.3 Effect of Fixing Secular Velocity in Transient Displacement Estimation

In isolating the transient signal of a GPS time series, there are potentially significant trade-offs between the secular (interseismic) velocity and the long-term exponential decay. This is not so much of a problem for continuous GPS installed a few years before the earthquake or campaign data with good coverage, but for sites where the secular velocity estimates are made by spatial interpolation, and more errors are introduced, trade-off issues must be considered.

The errors used for the interpolated velocity estimates are simply the interpolated errors in sites with velocity estimates. The impact of using an uncertain linear velocity was examined by fitting the time series in two different ways. First the a priori velocity was used with its a priori uncertainty applied. Then, the time series are inverted again, this time with an effectively fixed velocity (error of <1 mm/yr), and the postseismic displacements are compared to the first estimates.

Only a few regions show noticeable differences (Figure 27)—those adjacent to the western tipline of the rupture, and some far south near the subduction zone (which are affected by slow-slip events). Overall, the interpolated velocities and errors (which can be quite high) are adequate and can be used in the postseismic dataset. Additionally, where these differences occur are not in regions where there is systematic bias in the postseismic models (see next section), so they can be ruled out as a cause of this misfit.

3 years

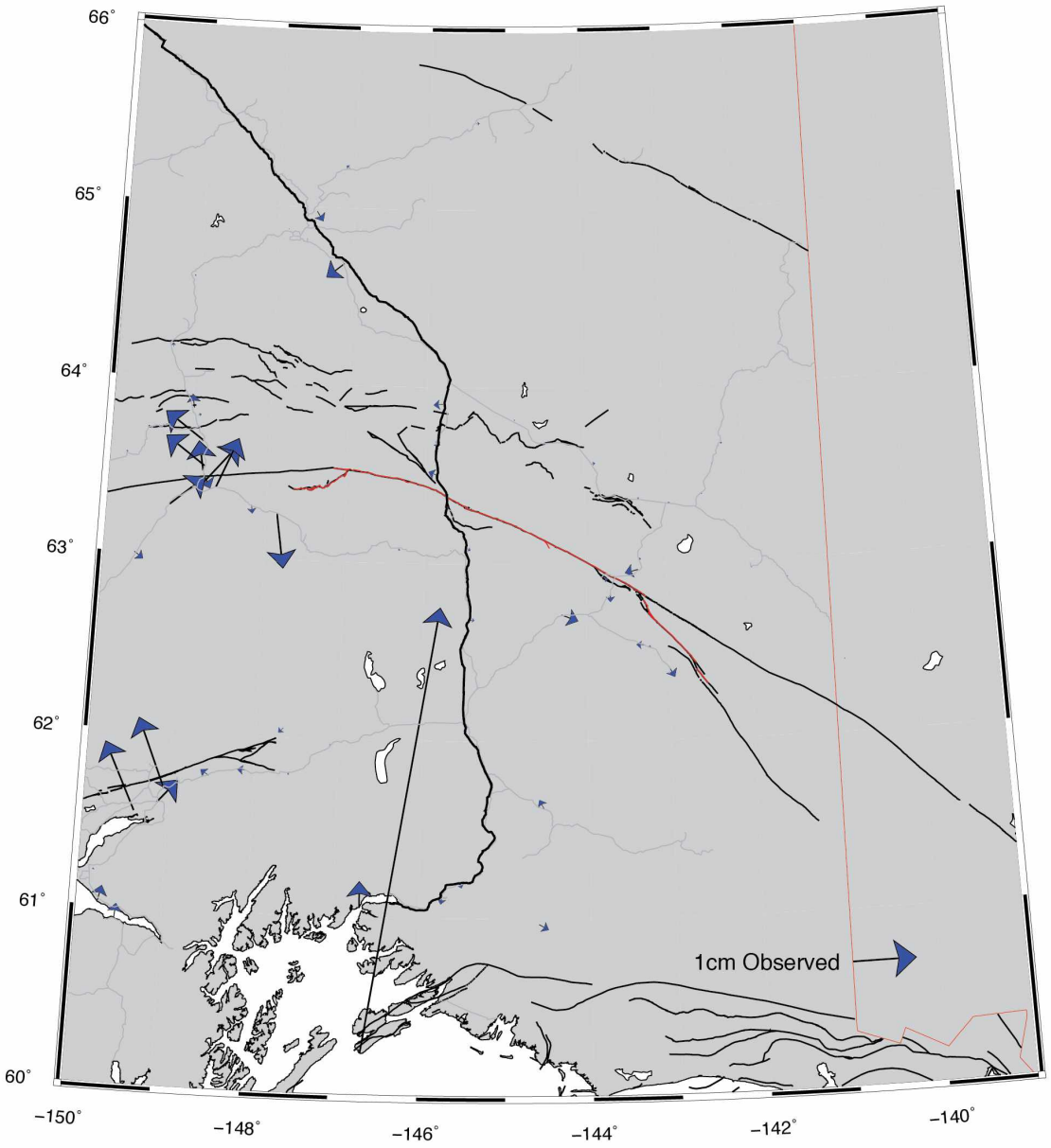

Figure 27. Differences between postseismic displacement observations when time series are fit with a fixed velocity or the linear velocity allowed to vary. The only significant discrepancies are adjacent to the western tip of the rupture and at some southern sites (likely affected by a slow slip event at the subduction zone).

6 years

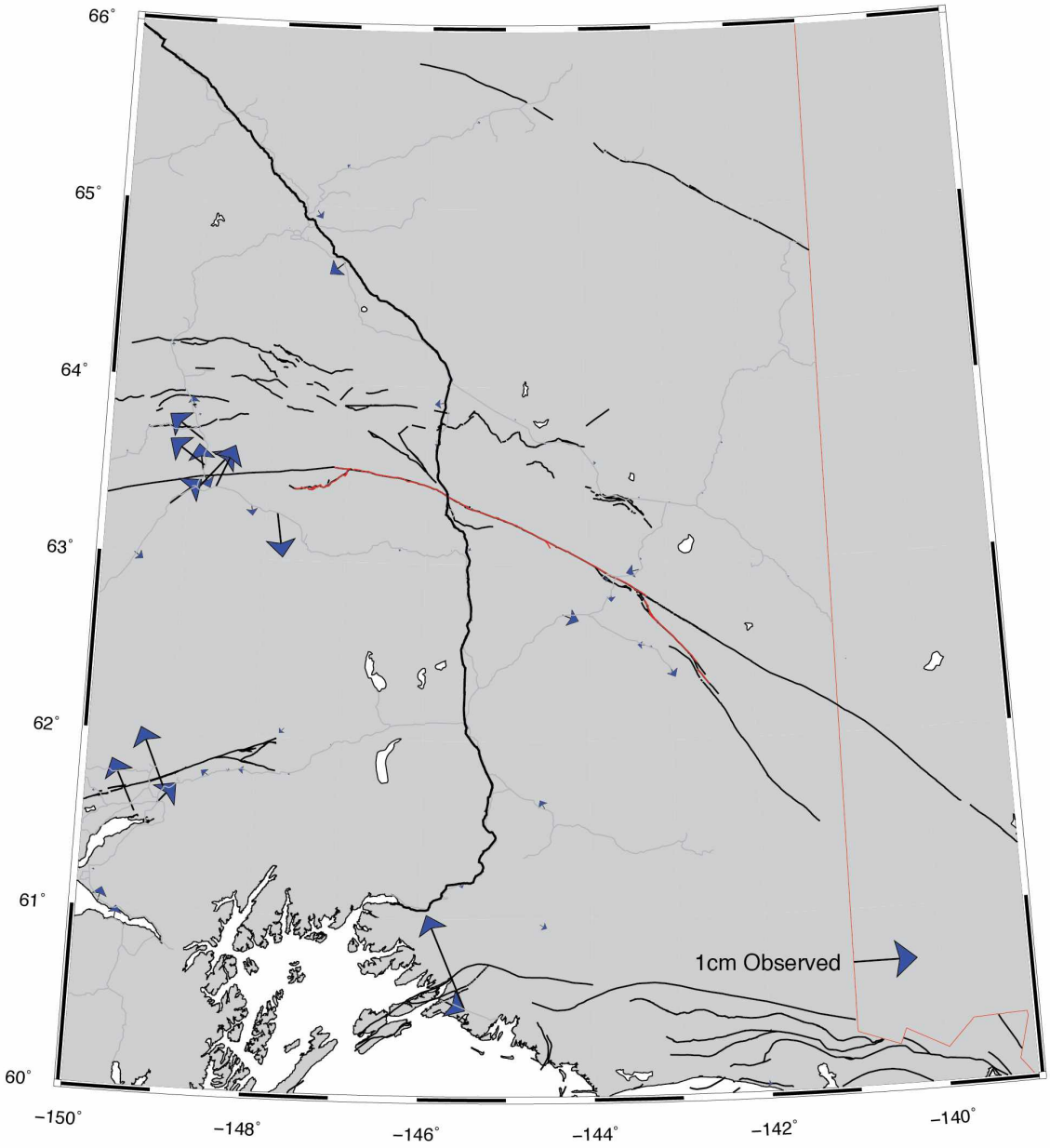

Figure 27 cont.

7.4 FEM Model Fit and Steps Forward Developing an Optimal Postseismic Model

Beginning the postseismic modeling process, the first approximation of viscous structure is based on the most recent postseismic study (Figure 28). The disparity in mantle viscosity north and south of the fault was implemented in that study to improve the overall model fit, but other factors were not considered first. This model yields unsatisfactory results—namely a systematic bias in the orientation of the displacement vectors in the early time series (2003-2006, 2006-2009) (Figure 29). To begin improving the model fit, the effect of the subducting Pacific plate to the south is considered first. A test model with a dipping elastic slab shows changes in displacements (slab – no slab) that are similar to at least some of the model residual patterns (and may change the overall pattern of residuals from fault normal to fault parallel, which is easier to explain with afterslip) (Figure 30). Regardless, the effects are shown to be non-negligible, so a slab should be included.

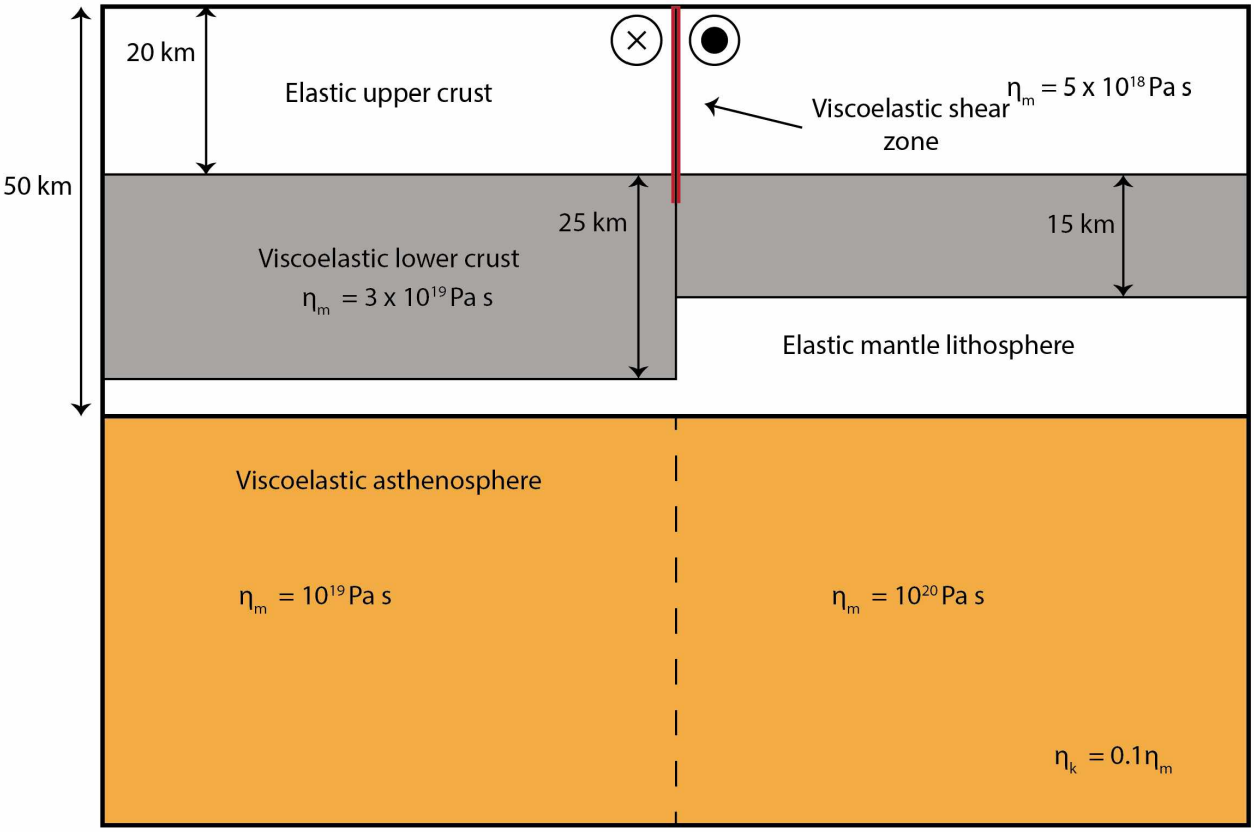

Figure 28. The viscous structure of the first postseismic model and the starting viscosity values. All viscoelastic bodies are Burgers materials, and the transient velocity component is an order of magnitude lower than the long-term component. The viscosity disparity in the upper-mantle is based on previous work by collaborator Yan Hu. Mantle viscosity in *Suito and Freymueller* [2009] was modeled with a viscosity of 3.2e19 Pa s, more consistent with the lower crustal viscosity here.

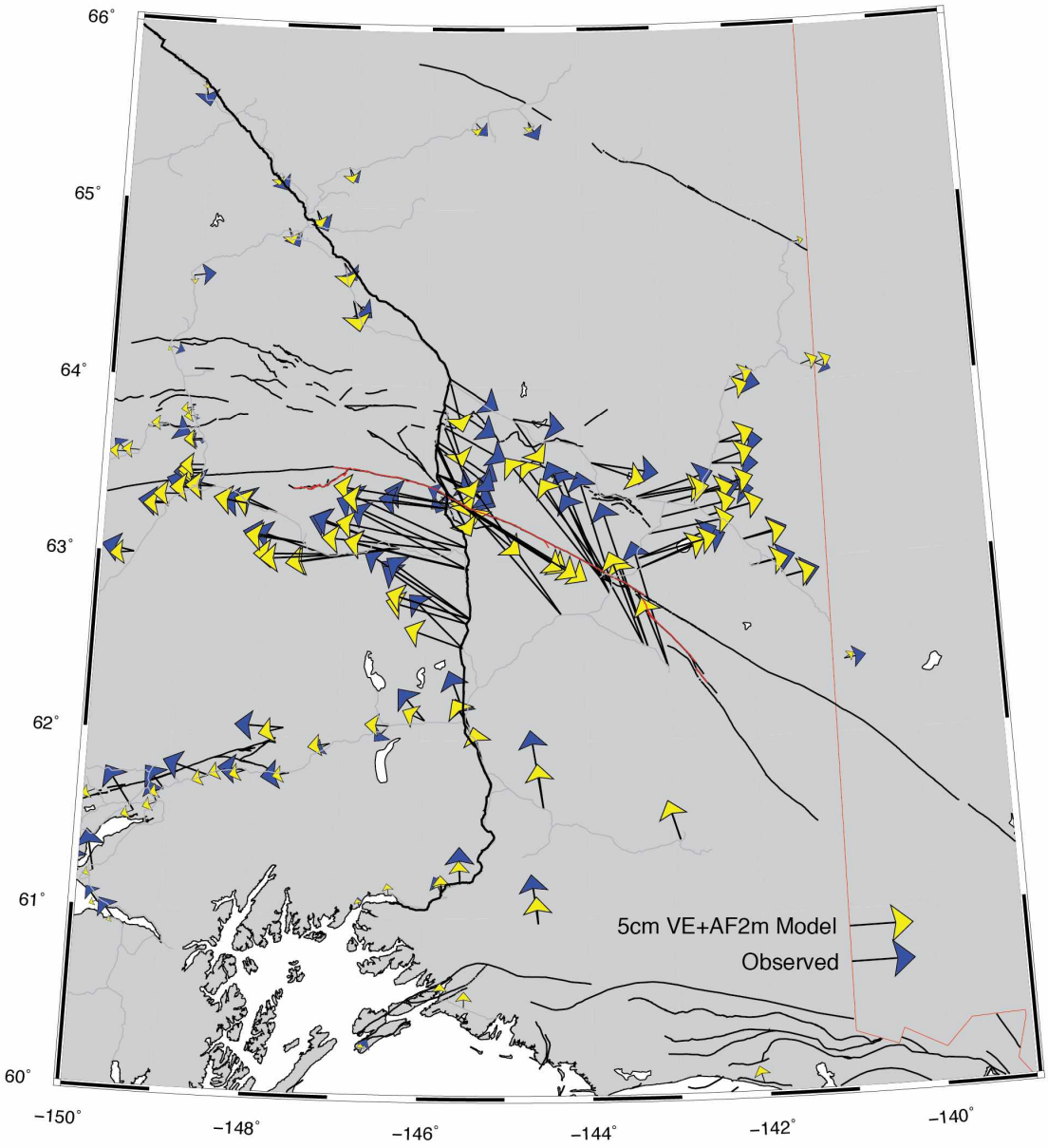

Figure 29. (Top) Observed and computed displacements for the 2003-2006 interval. (Bottom) Model residuals for the 2003-2006 interval. There is a dominant fault-normal component both north and south of the fault, and a large fault-parallel component very near the fault.

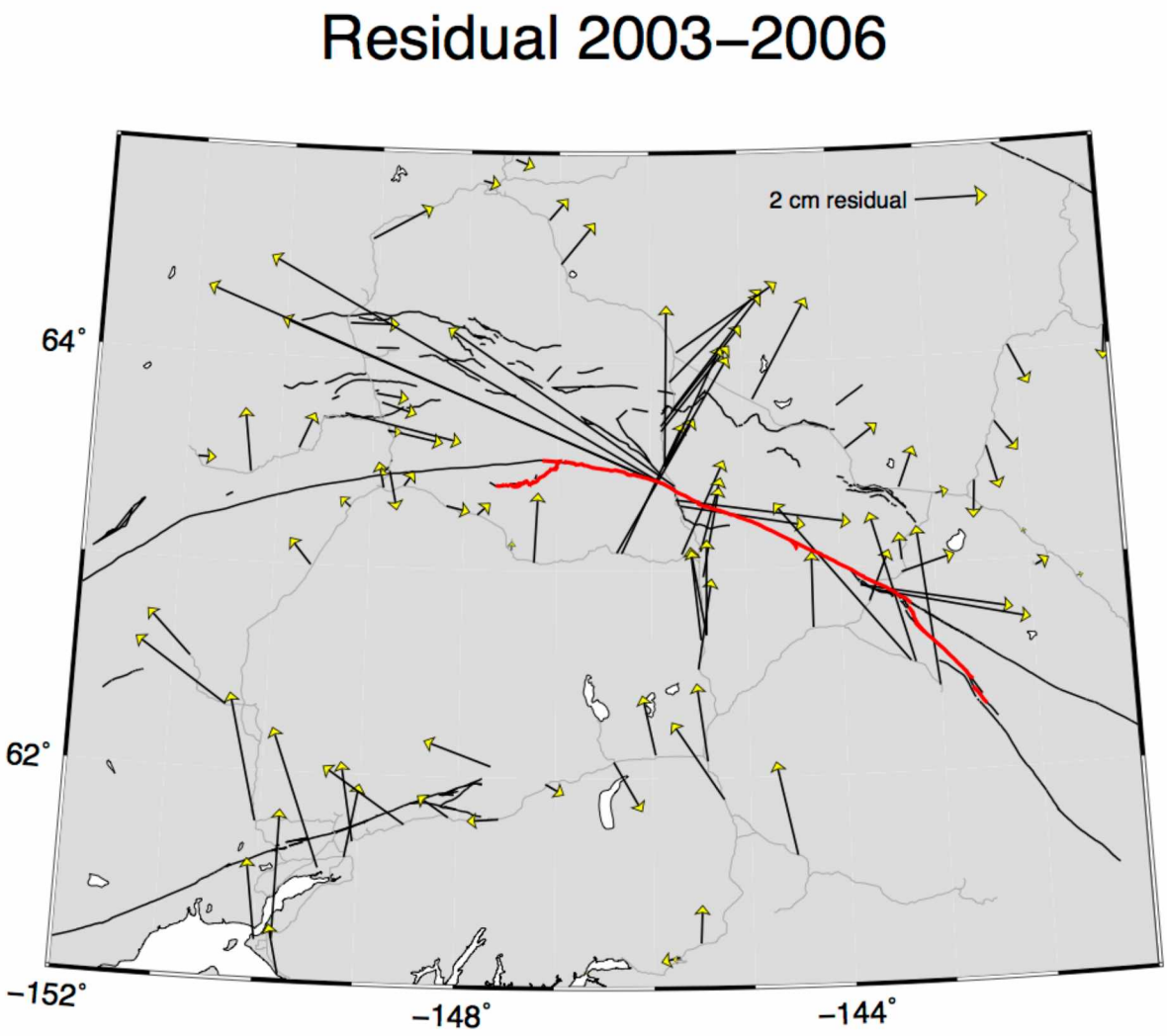

Figure 29 cont.

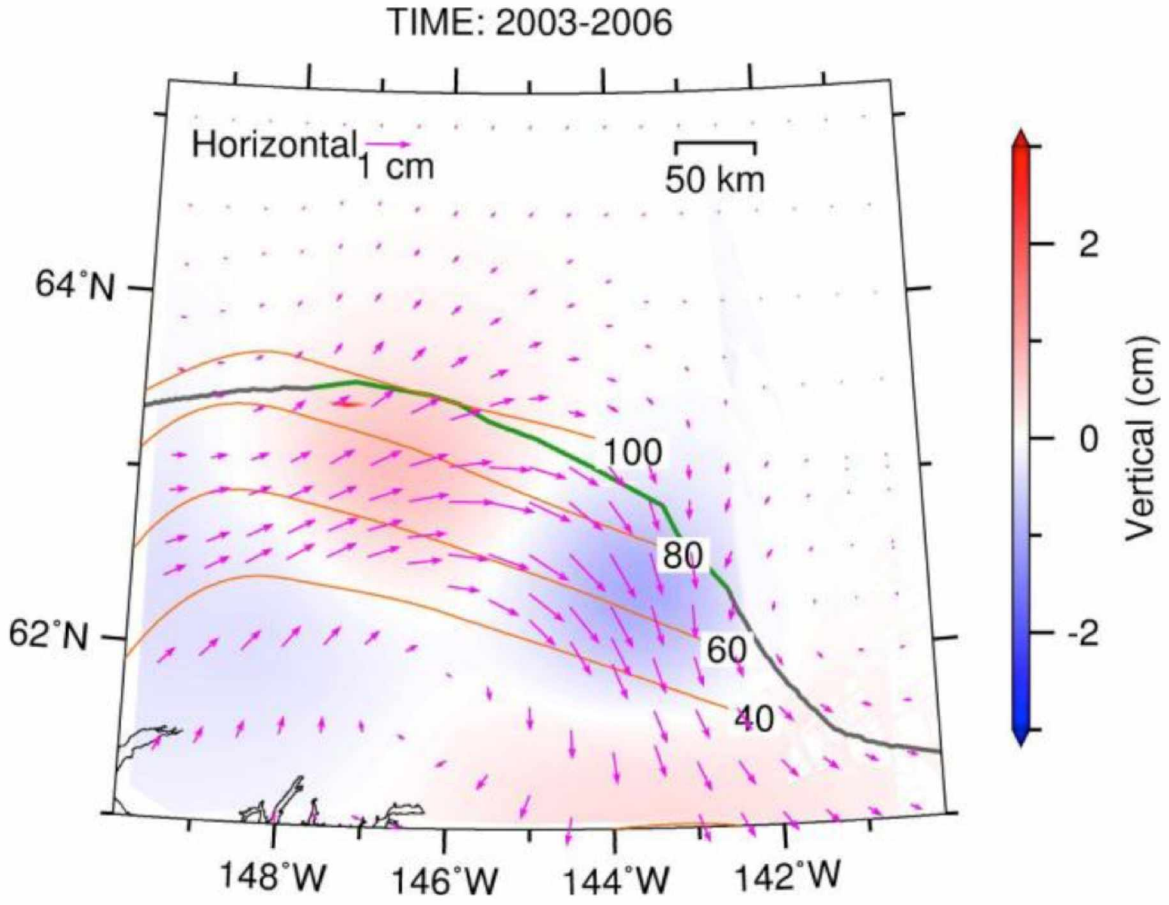

Figure 30. Differences in postseismic displacement due to the addition of an elastic subducting slab south of the Denali fault. (Figure courtesy of Yan Hu)

One must also consider the approach to afterslip modeling, which differs across many postseismic studies. A good reason for suspecting trouble in the afterslip modeling is that the major systematic bias occurs within the first six years—after this, the effects of afterslip should be negligible. The approach used in the existing FEM is to approximate afterslip as a viscoelastic process along a narrow shear zone surrounding the ruptured fault, and slip is allowed only on elements that did not exceed a certain threshold of coseismic slip. Afterslip is known to follow a rate-strengthening friction law, inconsistent with the modeling in this study [*Marone et al.*, 1991], so the viscoelastic shear zone approach should match the spatial pattern of afterslip but not the precise time decay.

A more pressing issue in modeling afterslip, however, is defining where afterslip is and is not allowed on the interface. Being dependent on coseismic stress changes, it is reasonable to exclude afterslip on major slip patches, but changes in rheology along the fault will also

determine afterslip locations. Additionally, the current model allows deep afterslip to only 30 km depth, and it's unclear how deep afterslip might occur in the first place. All of these issues contribute to difficulties in forward modeling afterslip.

I suggest an alternative to this approach where the initial postseismic model is viscoelastic relaxation only. Deformation is then estimated over a short interval, and the residual is kinematically inverted for afterslip on the fault interface. That afterslip over the short interval then adds to the stress changes, forcing additional viscoelastic relaxation. This process is iterated until changes to the afterslip are negligible. While this approach does not take the frictional and rheological laws of afterslip into account, it does eliminate the need to somewhat arbitrarily define where afterslip can and cannot occur. However, inverting the residual makes the assumption that the viscoelastic relaxation components are perfectly parameterized, introducing another degree of non-uniqueness. Realistic kinematic afterslip models will have to be constrained by physical plausibility such as in *Freed et al.* [2006].

Lastly, it may be that the viscous structure considered in the most recent study needs revision. The model uses the "jelly-sandwich" model of the lithosphere, but studies suggest good reason for abandoning this model, especially in back-arc subduction settings (which interior Alaska roughly fits) [*Freed et al.*, 2006]. Elimination of the purely elastic lithospheric mantle, then, might show improvements. The mantle viscosity disparity across the fault interface may also not be appropriate when these other factors are considered.

Chapter 8 Conclusions

The coseismic model presented here improves on previous studies by unifying the model coseismic and postseismic elastic structures, which is crucial for consistently reproducing coseismic displacements. The preferred 1D coseismic model (total WRSS = 4.86e3 m^2) fits the GPS data nearly as well as an Okada model (4.56e3 m^2). The success of this model eliminates the need to artificially apply deep slip to drive stress changes in postseismic models and can be used in similar earthquake cycle studies. In addition to the new elastic model, the coseismic displacement estimation program written in MATLAB provides a straightforward method of homogeneously processing GPS data sets and will be an invaluable tool in future (and current) studies.

Parameterization of time series is a great tool to constrain transient displacement, but in the tests carried out in this study, the future predictive power remains limited. It is unclear whether more data could resolve this problem, as best-fitting decay constants continue to change (full time series: τ_L = 0.125 years, τ_E = 20 years; 2012-windowed time series: τ_L = 0.075 years, τ_E = 15 years). However, it is clear that a decade of data is vastly better than 4 years in terms of predicting future deformation, with a prediction period WRSS decrease from an order of magnitude greater than the full time series to only a factor of two greater than the full time series. Other studies suggest adding even a third decay function in the parameterization to assess prediction power, which inevitably fits the data better, but strays from the purpose of resampling poorly-constrained campaign data. Observations in the following years will be essential to validating a new postseismic model.

Following the successful implementation of the elastic structure and the subducting oceanic slab in the south, a new postseismic model can quickly be developed. Since current model misfit is greatest in the first 6 years following the earthquake, it is likely viscosity values are reasonable, although the viscous structure may need slight modification. The approach to modeling afterslip needs to be improved. The alternative iterative kinematic approach to afterslip will be tested.

A working postseismic model will not only give good insight into Alaskan lithospheric rheology and general earthquake cycle processes, but will be a key component in developing a

complete tectonic block model of Alaska. Removal of transient signals such as glacial isostatic adjustment (GIA), postseismic relaxation from the 1964 Mw 9.2 earthquake, and recurring slow slip events is already accomplished with satisfactory models for each of these processes. A model for the transient deformation following the 2002 Denali Mw 7.9 earthquake is one of the final pieces in a complete tectonic model.

References

Argus, D. F., R. G. Gordon, M. B. Heflin, C. Ma, R. J. Eanes, P. Willis, W. R. Peltier, and S. E. Owen (2010), The angular velocities of the plates and the velocity of Earth's centre from space geodesy, Geophysical Journal International, 180, 913-960, doi: 10.1111/j.1365-246X.2009.04463.x.

Bender, A. M., and P. J. Haeussler (2017), Eastern Denali Fault surface trace map, eastern Alaska and Yukon, Canada, U.S. Geological Survey.

Boehm, J., A. Niell, P. Tregoning, and H. Schuh (2006), Global Mapping Function (GMF): A new empirical mapping function based on numerical weather model data, Geophysical Research Letters, 33, doi: 10.1029/2005GL025546.

Bürgmann, R., and G. Dresen (2008), Rheology of the lower crust and upper mantle: evidence from rock mechanics, geodesy, and field observations, Annual Review of Earth and Planetary Sciences, 36, 531-567, doi: 36.031207.124326.

Chinnery, M. A. (1961), The Deformation of the Ground Around Surface Faults, Bulletin of the Seismological Society of America, 51(3), 355-372.

Crone, A. J., S. F. Personius, P. A. Craw, P. J. Haeussler, and L. A. Staft (2004), The Susitna Glacier Thrust Fault: Characteristics of Surface Ruptures on the Fault that Initiated the 2002 Denali Fault Earthquake, Bulletin of the Seismological Society of America, 94, S5-S22.

Eberthart-Phillips, D., et al. (2003), The 2002 Denali Fault Earthquake, Alaska: A Large Magnitude, Slip-Partitioned Event, Science, 300, 1113-1118.

Elliott, J. L., J. T. Freymueller, and B. Rabus (2007), Coseismic deformation of the 2002 Denali fault earthquake: Contributions from synthetic aperture radar range offsets, Journal of Geophysical Research, 112, doi: 10.1029/2006JB004428.

Fletcher, H. J. (2002), Crustal deformation in alaska measured using the Global Positioning System, Ph.D. Dissertation, University of Alaska Fairbanks, Fairbanks, Alaska.

Freed, A. M., R. Bürgmann, E. Calais, J. Freymueller, and S. Hreinsdóttir (2006), Implications of deformation following the 2002 Denali, Alaska, earthquake for postseismic relaxation processes and lithospheric rheology, Journal of Geophysical Research, 111, doi: 10.1029/2005JB003894.

Fu, Y., and J. T. Freymueller (2012), Seasonal and long-term vertical deformation in the Nepal Himalaya constrained by GPS and GRACE measurements, Journal of Geophysical Research, 117, doi: 10.1029/2011JB008925.

Haeussler, P. J., et al. (2004), Surface Rupture and Slip Distribution of the Denali and Totschunda Faults in the 3 November 2002 M 7.9 Earthquake, Alaska, Bulletin of the Seismological Society of America, 94(6B), S23-S52.

Hearn, E. H., and R. Bürgmann (2005), The Effect of Elastic Layering on Inversions of GPS Data for Coseismic Slip and Resulting Stress Changes: Strike-Slip Earthquakes, Bulletin of the Seismological Society of America, 95.

Hearn, E. H., R. Bürgmann, and R. E. Reilinger (2002), Dynamics of Izmit Earthquake Postseismic Deformation and Loading of the Düzce Earthquake Hypocenter, Bulletin of the Seismological Society of America, 92(1), 172-193.

Hreinsdóttir, S., J. T. Freymueller, R. Bürgmann, and J. Mitchell (2006), Coseismic deformation of the 2002 Denali Fault earthquake: Insights from GPS measurements, Journal of Geophysical Research, 111, doi: 10.1029/2005JB003676.

Hu, Y. (2011), Deformation processes in great subduction zone earthquake cycles, Ph.D. Dissertation, University of Victoria, Victoria, BC.

Johnson, K. M., R. Bürgmann, and J. T. Freymueller (2009), Coupled afterslip and viscoelastic flow following the 2002 Denali Fault, Alaska earthquake, Geophysical Journal International, 176, 670-682, doi: 10.1111/j.1365-246X.2008.04029.x.

Kennett, B. L. N., E. R. Engdahl, and R. Buland (1995), Constraints on seismic velocities in the earth from travel times, Geophysical Journal International, 122.

Marone, C. J., C. H. Scholz, and R. Bilham (1991), On the mechanics of earthquake afterslip, Journal of Geophysical Research, 96, 8441-8452.

Matmon, A., D. P. Schwartz, P. J. Haeussler, R. Finkel, J. J. Lienkaemper, H. D. Stenner, and T. Dawson (2006), Denali fault slip rates and Holocene-late Pleistocene kinematics of central Alaska, Geology, 34, 645-648, doi: 10.1130/G22361.1.

Melosh, H. J., and A. Raefsky (1981), A Simple and Efficient Method for Introducing Faults into Finite Element Computations, Bulletin of the Seismological Society of America, 71(5), 1391-1400.

Nur, A., and J. R. Booker (1972), Aftershocks cause by pore fluid flow?, Science, 175.

Nur, A., and G. Mavko (1974), Postseismic viscoelastic rebound, Science, 183, 204-206.

Okada, Y. (1985), Surface deformation due to shear and tensile faults in a half-space, Bulletin of the Seismological Society of America, 75(4), 1135-1154.

Orowan, E. (1967), Seismic damping and creep in the mantle, Geophysical Journal International, 14.

Perfettini, H., and J.-P. Avouac (2004), Postseismic relaxation driven by brittle creep: A possible mechanism to reconcile geodetic measurements and the decay rate of aftershocks, application to the Chi-Chi earthquake, Taiwan, Journal of Geophysical Research, 109, doi: 10.1029/2003JB002488.

Plafker, G., T. Hudson, and D. H. Richter (1977), Preliminary observations on late Cenozoic displacements along the Totschunda and Denali fault systems, U.S. Geol. Surv. Circ.

Reid, H. F. (1910), The Mechanics of the Earthquake, The Carnegie institution of Washington.

Savage, J. C., and R. O. Burford (1973), Geodetic Determination of Relative Plate Motion in Central California, Journal of Geophysical Research, 78(5), 832-845.

Savage, J. C., and W. H. Prescott (1978), Asthenosphere readjustment and the earthquake cycle, Journal of Geophysical Research: Solid Earth, 83.

Scholz, C. H. (2002), The mechanics of earthquakes and faulting, Cambridge University Press.

Seitz, G. J., P. J. Haeussler, A. J. Crone, P. Lipovsky, and D. P. Schwartz (2008), Eastern Denali fault slip rate and paleoseismic history, Kluane Lake Area, Yukon Territory, Canada, in *American Geophysical Union, Fall Meeting 2008*, San Francisco, CA.

Stark, P. B., and R. L. Parker (1995), Bounded-variable least-squares: an algorithm and applications, Computational Statistics, 10, 129-129.

Stein, R. S. (1999), The role of stress transfer in earthquake occurrence, Nature, 402, 605-609.

Suito, H., and J. T. Freymueller (2009), A viscoelastic and postseismic deformation model for the 1964 Alaska earthquake, Journal of Geophysical Research, 114, doi: 10.1029/2008JB005954.

Tobita, M. (2016), Combined logarithmic and exponential function model for fitting postseismic GNSS time series after 2011 Tohoku-Oki earthquake, Earth, Planets and Space, 68, doi: 10.1186/s40623-016-0422-4.

Veenstra, E., D. H. Christensen, G. A. Abers, and A. Ferris (2006), Crustal thickness variation in south-central Alaska, Geology, 34(9), doi: 10.1130/G22615.1.